



Michigan Technological University
Create the Future Digital Commons @ Michigan Tech

Dissertations, Master's Theses and Master's
Reports - Open

Dissertations, Master's Theses and Master's
Reports

2010

Spin-strain coupling in a 3-D transition metal oxides

Ghous Bakhsh Narejo
Michigan Technological University

Follow this and additional works at: <https://digitalcommons.mtu.edu/etds>



Part of the [Electrical and Computer Engineering Commons](#)

Copyright 2010 Ghous Bakhsh Narejo

Recommended Citation

Narejo, Ghous Bakhsh, "Spin-strain coupling in a 3-D transition metal oxides", Dissertation, Michigan Technological University, 2010.

<https://doi.org/10.37099/mtu.dc.etds/77>

Follow this and additional works at: <https://digitalcommons.mtu.edu/etds>



Part of the [Electrical and Computer Engineering Commons](#)

SPIN-STRAIN COUPLING IN 3-*D* TRANSITION METAL OXIDES

By

GHOUS BAKHSH NAREJO

A DISSERTATION

Submitted in partial fulfillment of the requirements

for the degree of

DOCTOR OF PHILOSOPHY

(Electrical Engineering)

MICHIGAN TECHNOLOGICAL UNIVERSITY

2010

© 2010 Ghaus Bakhsh Narejo

This dissertation, "Spin-Strain Coupling in 3-*d* Transition Metal Oxides", is hereby approved in partial fulfillment of the requirements for the degree of DOCTOR OF PHILOSOPHY in the field of Electrical Engineering.

DEPARTMENT:
Electrical and Computer Engineering

Signatures:

Dissertation Advisor _____

Dr. Paul L. Bergstrom

Co-Advisor _____

Dr. Warren F. Perger

Department Chair _____

Dr. Daniel R. Fuhrmann

Date _____

Contents

List of Figures	xi
List of Tables	xv
Acknowledgments	xix
Abstract	xxi
1 Introduction	1
1.1 Introduction to Transition Metal Oxide (TMO) physics	6
1.1.1 Electronic Structure of TMOs	6

1.1.2	Electronic configuration of transition metals (TMs), <i>Ba</i> and <i>O</i> atoms	7
1.1.3	Crystal Field in TMOs	12
1.1.4	Chemical Bonding in TMOs	18
1.1.5	<i>d</i> Orbitals in TMOs	19
1.1.6	Spin Exchange in TMOs	23
1.2	Introduction to CRYSTAL09 Program	28
1.2.1	Computational Parameters	28
1.2.2	ELASTCON Algorithm	29
1.2.3	EOS Algorithm	31
1.2.4	BILLY Program	32
1.3	Thesis statement	33
1.4	Research outline	34

2	Crystalline Geometry and Elastic Properties of Tetragonal $BaTiO_3$	43
2.1	Introduction	43
2.1.1	ELASTCON Algorithm	46
2.1.2	EOS Algorithm	48
2.2	Choice of basis sets	49
2.3	Selection of Hartree Fock, DFT and hybrid potentials	51
2.4	Discussion of computational results	52
2.5	Conclusions	57
3	Electronic Structure and Properties of Rutile TiO_2	71
3.1	Introduction	71
3.2	Computational procedure	73
3.3	Potentials and basis sets	75
3.4	Experiments	77

3.5	Computational parameters	79
3.6	Discussion of results	80
3.7	Conclusions	82
4	Optimized Lattice Parameters and Elastic Properties of $BaFeO_3$	93
4.1	Introduction	93
4.2	Procedures	96
4.2.1	Potentials and basis sets	96
4.2.2	Billy script	97
4.2.3	Computational tolerances	98
4.3	Computational results	98
4.4	Analysis	99
4.5	Concluding Remarks	101

5	Spin-Strain Coupling in 3-<i>d</i> Transition Metal Oxides	111
5.1	Introduction	111
5.2	Computations	113
5.2.1	Quantum mechanical model	114
5.3	Results	116
5.4	Analysis of results	119
5.5	Concluding Remarks	121
6	Conclusions	137
6.1	Research accomplishments	140
6.2	Future directions	142
A	JOURNAL PUBLISHING AGREEMENT Elsevier B.V.2	145
A.0.1	ASSIGNMENT OF PUBLISHING RIGHTS	145
A.0.2	RETENTION OF RIGHTS FOR SCHOLARLY PURPOSES	146

List of Figures

1.1	Unit cells of cubic $BaFeO_3$ and $BaTiO_3$	8
1.2	Unit cell of rutile TiO_2	9
1.3	Electronic configuration of Ba and O atoms	10
1.4	Electronic configuration of Ti and Fe atoms	11
1.5	Diagrams showing strained octahedral cages.	15
1.6	The crystal field split-off	16
1.7	Top: Figure shows the crystal field and spin alignment before strain. Bottom: Figure shows new spin alignment after strain.	17
1.8	Plots showing $1s$ and $2p_x$, $2p_y$ and $2p_z$ orbitals	20

1.9	Plots showing d_{z^2} , $d_{x^2-y^2}$, d_{xy} , d_{yz} and d_{xz} orbitals	21
1.10	Electronic configuration of Ba and O atoms with electron spin polarization	24
1.11	Electronic configuration of Sc and Ti atoms showing spin polarization	25
1.12	Electronic configuration of V and Cr atoms showing spin states . . .	26
1.13	Electronic configuration of Mn and Fe atoms showing spin states . .	27
2.1	Comparison between the computational and experimental values of bulk moduli is shown for basis set 1.	63
2.2	Comparison between the computational and experimental values of bulk moduli is shown for basis set 2.	64
2.3	Comparison between the computational and experimental values of elastic constants and bulk moduli is shown for basis set 1.	65
2.4	Comparison between the computational and experimental values of elastic constants and bulk moduli is shown for basis set 2.	66

3.1	Computational and experimental values of second-order elastic constants and bulk moduli	87
3.2	Computational and experimental values of bulk moduli	88
4.1	Computational values of bulk moduli for cubic $BaFeO_3$	106
5.1	Two unit cells of $BaFeO_3$ employed during computations.	128
5.2	Two unit cells of $BaTiO_3$ employed during computations.	129
5.3	Exchange energy vs. lattice strain for cubic $BaScO_3$	129
5.4	Exchange energy vs. lattice strain for cubic $BaTiO_3$	130
5.5	Exchange energy vs. lattice strain for cubic $BaVO_3$	130
5.6	Exchange energy vs. lattice strain for cubic $BaCrO_3$	131
5.7	Exchange energy vs. lattice strain for cubic $BaMnO_3$	131
5.8	Exchange energy vs. lattice strain for cubic $BaFeO_3$	132

List of Tables

2.1	Values of relaxed lattice constants (in $\overset{\circ}{A}$), ambient volume (in $\overset{\circ}{A}^3$) and total energy E (in a.u.), for tetragonal $BaTiO_3$ with basis set 1. . . .	59
2.2	Values of relaxed lattice constants (in $\overset{\circ}{A}$), ambient volume (in $\overset{\circ}{A}^3$) and total energy E (in a.u.), for tetragonal $BaTiO_3$ with basis set 2. . . .	60
2.3	Computational results of elastic constants and bulk moduli employing basis set 1.	60
2.4	Computational results of elastic constants and bulk moduli employing basis set 2.	61
2.5	Equation of state results for tetragonal $BaTiO_3$ employing basis set 1.	61
2.6	Equation of state results for tetragonal $BaTiO_3$ employing basis set 2.	62

3.1	The values of relaxed lattice constants (in $\overset{\circ}{\text{\AA}}$) and ambient volume (in $\overset{\circ}{\text{\AA}}^3$) and total energy, E (in a.u.), for rutile TiO_2 using basis set 1. . .	84
3.2	The values of relaxed lattice constants (in $\overset{\circ}{\text{\AA}}$) and ambient volume (in $\overset{\circ}{\text{\AA}}^3$) and total energy, E (in a.u.), for rutile TiO_2 using basis set 2. . .	84
3.3	The elastic constants and bulk modulus computational results using basis set 1.	85
3.4	The elastic constants and bulk modulus computational results using basis set 2.	85
3.5	Equation of state results for tetragonal TiO_2 using basis set 1.	86
3.6	Equation of state results for rutile TiO_2 using basis set 2.	86
4.1	The values of relaxed lattice constants (in $\overset{\circ}{\text{\AA}}$), ambient volume (in $\overset{\circ}{\text{\AA}}^3$), density (in gm/cm^3), and energy (in a.u.) for cubic $BaFeO_3$ for basis set 1.	102
4.2	Computational values of elastic constants and bulk moduli with basis set 1.	102
4.3	Equation of state results for cubic $BaFeO_3$ employing basis set 1. . .	103

4.4	The values of relaxed lattice constants (in $\overset{o}{\text{\AA}}$), ambient volume (in $\overset{o}{\text{\AA}^3}$), density (in gm/cm^3), and energy (in a.u.) for cubic $BaFeO_3$ employing basis set 2.	103
4.5	Computational values of elastic constants and bulk moduli with basis set 1.	104
4.6	Equation of state results for cubic $BaFeO_3$ employing basis set 2. . .	104
4.7	The values of relaxed lattice constants (in $\overset{o}{\text{\AA}}$), ambient volume (in $\overset{o}{\text{\AA}^3}$), density (in gm/cm^3), and energy (in a.u.) for tetragonal $BaFeO_3$ employing basis set 1.	104
4.8	Equation of state results for tetragonal $BaFeO_3$ employing basis set 1	105
4.9	The values of relaxed lattice constants (in $\overset{o}{\text{\AA}}$), ambient volume (in $\overset{o}{\text{\AA}^3}$), density (in gm/cm^3), and energy (in a.u.) for tetragonal $BaFeO_3$ employing basis set 2.	105
4.10	Equation of state results for tetragonal $BaFeO_3$ employing basis set 2.	105
5.1	Computational values of $E_{fm.}$, $E_{exch.}^{fm.}$, $E_{afm.}$ and $E_{exch.}^{afm.}$ are determined for cubic $BaScO_3$	122

5.2	Computational values of $E_{fm.}$, $E_{exch.}^{fm.}$, $E_{afm.}$ and $E_{exch.}^{afm.}$ are determined for cubic $BaTiO_3$	123
5.3	Computational values of $E_{fm.}$, $E_{exch.}^{fm.}$, $E_{afm.}$ and $E_{exch.}^{afm.}$ are determined for cubic $BaVO_3$	124
5.4	Computational values of $E_{fm.}$, $E_{exch.}^{fm.}$, $E_{afm.}$ and $E_{exch.}^{afm.}$ are determined for cubic $BaCrO_3$	125
5.5	Computational values of $E_{fm.}$, $E_{exch.}^{fm.}$, $E_{afm.}$ and $E_{exch.}^{afm.}$ are determined for cubic $BaMnO_3$	126
5.6	Computational values of $E_{fm.}$, $E_{exch.}^{fm.}$, $E_{afm.}$ and $E_{exch.}^{afm.}$ are determined for cubic $BaFeO_3$	127

Acknowledgments

I owe my deepest gratitude to Dr. Paul L. Bergstrom and Dr. Warren F. Perger, who have always provided encouragement, guidance and support. They have enabled me to develop a thorough understanding of the science and engineering of 3-*d* transition metal oxides. It is an honor for me that Dr Anand Kulkarni and Dr Miguel Levy have given their valuable advices for the research project.

Lastly, I offer my sincere regards to my colleagues in Dr Bergstrom group, the ECE and Physics faculty who have encouraged me during my research effort at Michigan Technological University.

Ghous B. Narejo

Abstract

ab-initio Hartree Fock (HF), density functional theory (DFT) and hybrid potentials were employed to compute the optimized lattice parameters and elastic properties of perovskite 3-*d* transition metal oxides. The optimized lattice parameters and elastic properties are interdependent in these materials. An interaction is observed between the electronic charge, spin and lattice degrees of freedom in 3-*d* transition metal oxides. The coupling between the electronic charge, spin and lattice structures originates due to localization of *d*-atomic orbitals. The coupling between the electronic charge, spin and crystalline lattice also contributes in the ferroelectric and ferromagnetic properties in perovskites. The cubic and tetragonal crystalline structures of perovskite transition metal oxides of ABO_3 are studied.

The electronic structure and the physics of 3-*d* perovskite materials is complex and less well considered. Moreover, the novelty of the electronic structure and properties of these perovskites transition metal oxides exceeds the challenge offered by their complex crystalline structures. To achieve the objective of understanding the structure and property relationship of these materials the first-principle computational method is employed.

CRYSTAL09 code is employed for computing crystalline structure, elastic, ferromagnetic and other electronic properties.

Second-order elastic constants (SOEC) and bulk moduli (B) are computed in an automated process by employing ELASTCON (elastic constants) and EOS (equation of state) programs in CRYSTAL09 code. ELASTCON, EOS and other computational algorithms are utilized to determine the elastic properties of tetragonal $BaTiO_3$, rutile TiO_2 , cubic and tetragonal $BaFeO_3$ and the ferromagnetic properties of 3-*d* transition metal oxides. Multiple methods are employed to crosscheck the consistency of our computational results.

Computational results have motivated us to explore the ferromagnetic properties of 3-*d* transition metal oxides. *Billyscript* and CRYSTAL09 code are employed to compute the optimized geometry of the cubic and tetragonal crystalline structure of transition metal oxides of *Sc* to *Cu*. Cubic crystalline structure is initially chosen to determine the effect of lattice strains on ferromagnetism due to the spin angular momentum of an electron.

The 3-*d* transition metals and their oxides are challenging as the basis functions and potentials are not fully developed to address the complex physics of the transition metals. Moreover, perovskite crystalline structures are extremely challenging with respect to the quality of computations as the latter requires the well established methods.

Ferroelectric and ferromagnetic properties of bulk, surfaces and interfaces are explored by employing CRYSTAL09 code. In our computations done on cubic TMOs of *Sc–Fe*

it is observed that there is a coupling between the crystalline structure and FM/AFM spin polarization. Strained crystalline structures of 3-*d* transition metal oxides are subjected to changes in the electromagnetic and electronic properties. The electronic structure and properties of bulk, composites, surfaces of 3-*d* transition metal oxides are computed successfully.

Chapter 1

Introduction

Silicon (Si) microfabrication techniques have been highly successful in reducing the size of MOSFET. This trend has resulted in ultra small gate lengths for MOSFETs. According to Moore's law [1], the number of transistors on a chip is expected to double every year. It has been predicted that Si MOSFET will continue to scale down to device dimensions of 10 nm.

Due to miniaturization, the size of a Si MOSFET is approaching the atomistic range. It is a challenge to design the MOSFET of sub-100 nm size as it has touched the atomic physics limit. Moreover, the trend of miniaturization in Si microfabrication industry is now severely constrained [2]. High electric fields [3, 4], electron tunneling and leakage currents have significant impacts on the future of Si as a material of

choice. Appearance of tunneling currents through ultra thin gate oxide introduces a physical limitation on the design of *Si* MOSFETs [3, 4]. The emergence of secondary effects in a MOSFET strengthens the case of computational physics simulations [5] as a viable method [6].

The secondary effects in Si MOSFET validate the research on alternative technologies. It is expected that the shrinking [2] of Si MOSFET will continue for several years till the advent of alternative technologies.

Spintronics is one of the very exciting alternative technologies. The spin of electron is a quantum mechanical property. Coupling between electron charge and spin in transition metals results in giant magnetoresistance (GMR) [7].

Electron spins are spontaneously polarized in these transition metals resulting in a high magnetic moment. Transition metals such as *Cr* and *Fe* are employed in GMR devices [8] based upon the thin film composite nanostructures. Magnetoresistance effect appears due to interfacial properties of nanostructured composites of transition metals [7]. Degeneracy is partially lifted perpendicular to the interfaces in thin film composites utilized for GMR devices. The energy discretization is utilized for spin-dependent tunneling. Transition metals possess spin-dependent density of states for spins being up or down.

The spintronics technology based upon the magnetoresistance logic is relatively free from the challenges of scaling and power consumption [9]. Magnetoresistance effect consumes less power as it utilizes the spin angular momentum of an electron. Existing spintronic devices provided a solution to challenge of high-density data storage for the modern microprocessor applications [8, 7]. TMR and other spintronic device mechanisms were also developed upon the spin-dependent tunneling mechanism. The spintronic device approaches based upon GMR effect has not materialized into three-terminal spintronic devices.

In early spintronic designs, the Schottky junctions [10] formed between transition metals and other materials have not been able to inject spin with maximum efficiency. The spin scattering and spin relaxation at interfaces are major challenges in current spintronic designs [11]. Therefore, it has remained a challenge to implement an three-terminal spintronic device based upon the composites of ordinary metals as well as transition metals.

Oxides of transition metals possess a variety of electronic structure and properties. Research into ferroic properties of these materials has been performed by refs. [12, 13, 14, 15, 16]. The mechanism of elastic coupling [17, 18, 19] in transition metal oxides has been widely researched. Our research on transition metal oxides is motivated by the prospect of low power dissipation in spintronic devices of transition metal oxides. In these materials, there is an interplay between the electronic charge, spin

and orbitals (see section 1.1 on the physics of TMOs). These materials exhibit a significantly higher electronic exchange and correlation due to localized d -orbitals.

The degeneracy is partially lifted in these materials due to electrostatic field. Electron spins and charge dipoles are spontaneously formed in oxides of transition metals. The spontaneous polarization and magnetization result in ferroelectric and ferromagnetic properties respectively.

A variation in ferroelectric, ferromagnetic and ferroelastic properties is possible in these materials due to compression as well as expansion of the crystalline lattice. The elastic properties of 3- d transition metal oxides must be explored due to coupling between electron spin angular momentum and crystalline symmetry of perovskites.

The injection, control and detection of the quantum mechanical electron spin [20] through lattice coupling can lead to a new paradigm shift in nanoelectronics. Oxides of transition metals, however, can also be utilized to inject an electron spin in a controlled manner [21]. These spin states can be injected, transported and detected in transition metals at room temperature. Devices based upon the electron spin in 3- d transition metals can couple electron spin exchange with periodic crystalline structure.

Variations in the competition between the crystal field and electron spin exchange due to an external pressure may also result in spin transitions. Oxides of transition

metals are magnetic semiconductors and do not suffer from these spin relaxation issues typically associated with ordinary metals.

Pressure-induced spin transitions can be implemented as logic states. Therefore, a novel device based upon the spin angular momentum of an electron provides an alternative to the charge-based logic. The significance of the electron spin angular momentum increases at nanoscale [22]. Novel logic designs can be implemented to utilize the electron spin [23].

The major focus of this research project is to develop the methods and materials by exploring the elastic properties of ferroic materials. The first principle computational methods are viable techniques to study the atomistic and molecular level logic designs which are physically realizable now [6]. We have employed first principle computational techniques to compute the elastic properties of 3-*d* transition metal oxides. The coupling between the spin and lattice structure in transition metal oxides is explored in *BaScO₃*, *BaTiO₃*, *BaVO₃*, *BaCrO₃*, *BaMnO₃* and *BaFeO₃*. We have studied spin-strain coupling in cubic and tetragonal structures of *BaTiO₃*, *BaFeO₃* and *Ba_xFe_{1-x}TiO₃*.

The devices based upon the spin polarization in the oxides of these transition metals can be utilized for sensing, actuation, high density data storage and spintronic applications. A whole new range of processors can be developed based upon the spin logic.

1.1 Introduction to Transition Metal Oxide (TMO) physics

Transition Metal Oxides (TMOs) can occur in a $A(Ba)B(Sc - Cu)O_3$ perovskite crystalline structure form. Our research has been focused on the perovskite structures containing Ba atom positioned at the edge, transition metals $Sc - Cu$ at the centre and O atom at each face of the unit cell (see Figures: 1.1 and 1.2).

In cubic perovskites of TMOs, an octahedral cage is formed having O atoms at the corners and transition metal positioned at the centre of the cage.

The interaction between the electronic spin and lattice structure is weak in an ordinary metal or gas due to valence electrons located in s and p orbitals.

Sections below will discuss the electronic configuration, d -orbitals, chemical bonding and crystal field in TMOs. The Figure 1.6 shows the crystal structure, crystal field, energy doublets and triplets for a cubic ABO_3 perovskite.

1.1.1 Electronic Structure of TMOs

Oxides of transition metals form a rich variety of crystalline structures. The wide variety of crystalline structures is caused by partially filled d - orbitals of transition

metal ions. The position of transition metals and their ionic radii results in a diversity of crystalline structures such as hexagonal, orthorhombic, tetragonal and cubic. Crystalline structure is coupled with the electron charge, spin and atomic orbitals in each unit cell.

Crystalline structures of $BaTiO_3$, $BaFeO_3$ and rutile TiO_2 are shown Figures 1.1 and 1.2. We computed the optimized lattice structures of these crystalline material systems.

1.1.2 Electronic configuration of transition metals (TMs), Ba and O atoms

The electronic properties of transition metals are different than ordinary metals. The electronic configuration in transition metals result in partially filled d -orbitals. The electron wavefunctions and probability density function of a d -orbital is significantly different than the s and p orbitals. For ordinary metals the valence electrons occupy $s - p$ orbitals. Figures 1.3 and 1.4, 1.8 and 1.9 show the electronic configurations of Ba , O , Ti and Fe atoms and shapes of s , p and d orbitals.

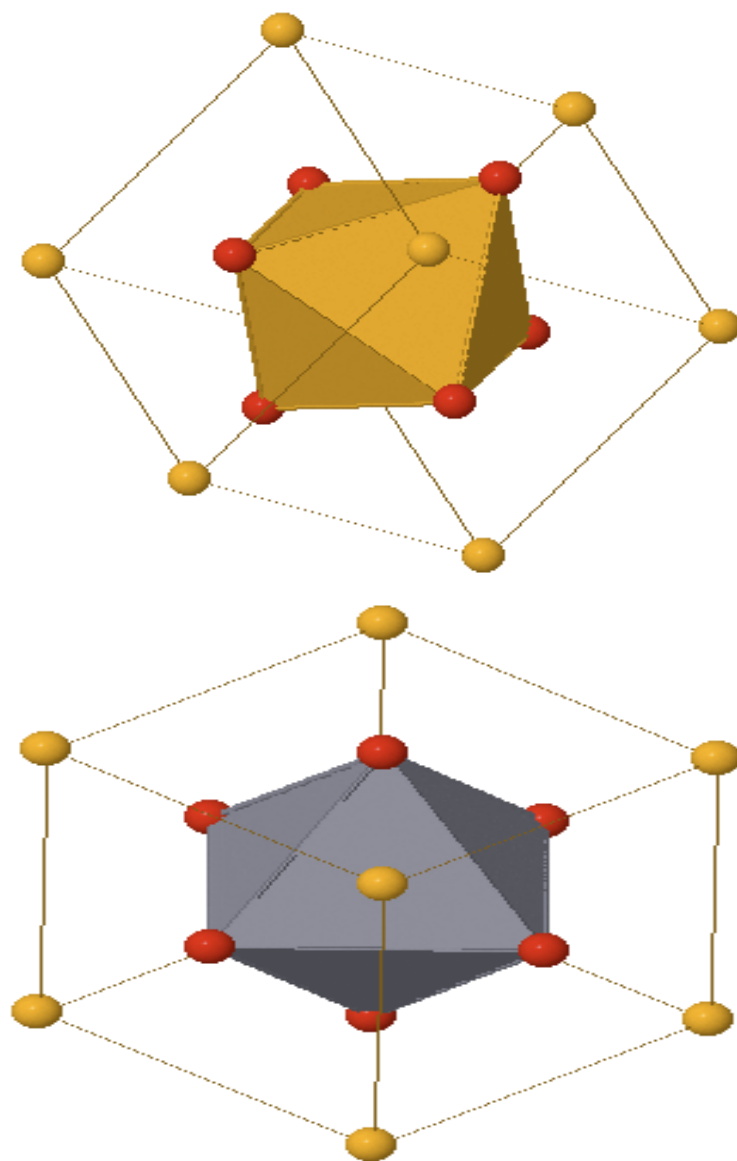


Figure 1.1: Unit cells of cubic $BaFeO_3$ and $BaTiO_3$ respectively. Yellow and red spheres represent Ba and O . Fe and Ti atoms are positioned in the middle of the octahedral cage.

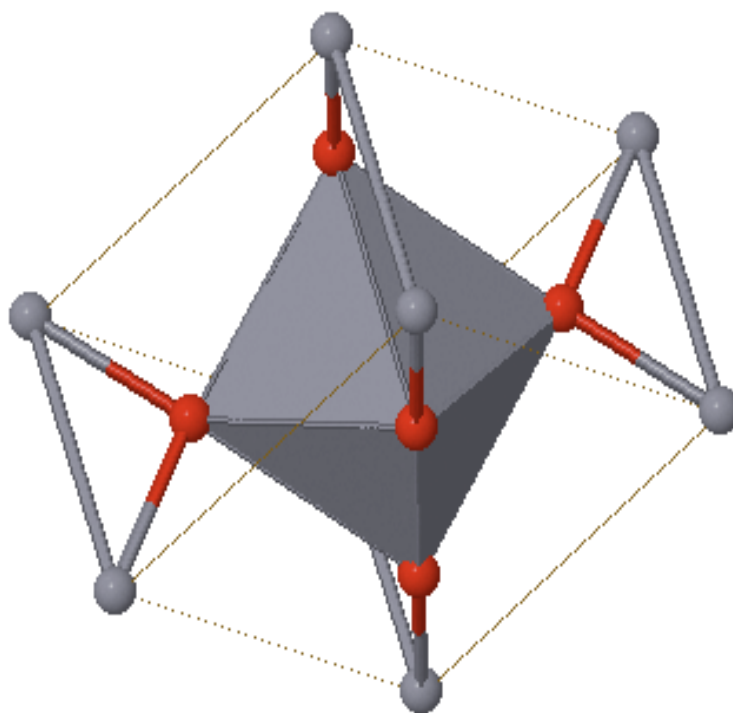


Figure 1.2: Unit cell of rutile TiO_2 . Red colored sphere represents O atoms. Ti atom is positioned in the center of the octahedral cage.

56

Barium



1s●●
 2s●● 2p●●●●●●
 3s●● 3p●●●●●● 3d●●●●●●●●●●
 4s●● 4p●●●●●● 4d●●●●●●●●●●
 5s●● 5p●●●●●●
 6s●●

Configuration: [Xe]6s²
 Valence: **2**
 Block: **s**
 Group: **2**
 Period: **6**

8

Oxygen



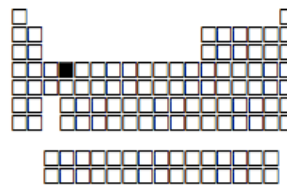
1s●●
 2s●● 2p●●●●○○

Configuration: [He]2s²2p⁴
 Valence: **2**
 Block: **p**
 Group: **16**
 Period: **2**

Figure 1.3: Electronic configurations of *Ba* and *O* atoms.

22

Titanium

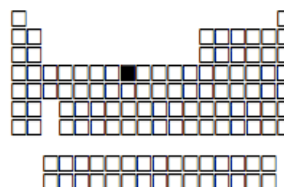


1s●●
 2s●● 2p●●●●●●●●
 3s●● 3p●●●●●●●● 3d●●○○○○○○○○
 4s●●

Configuration: $[\text{Ar}]4s^23d^2$
 Valence: **4**
 Block: **d**
 Group: **4**
 Period: **4**

26

Iron



1s●●
 2s●● 2p●●●●●●●●
 3s●● 3p●●●●●●●● 3d●●●●●●●●○○○○
 4s●●

Configuration: $[\text{Ar}]4s^23d^6$
 Valence: **3**
 Block: **d**
 Group: **8**
 Period: **4**

Figure 1.4: Electronic configurations of *Ti* and *Fe* atoms.

In oxides of transition metals, the interaction between electron spin and charge is significantly higher due to position of valence electrons. The quantum mechanical wavefunction of an electron in d -orbital of the transition metal adjusts itself to various shapes due to coulomb force between electrons and parent ion.

Electronic configurations of d - electrons in TMs are delocalized or localized due to varying amount of screening from electrons in adjacent ions.

1.1.3 Crystal Field in TMOs

Crystal field and ligand field are two most prominent models which are based on the electrostatic and molecular orbital approaches. These models explain the inorganic chemistry of transition metal oxides. The crystal field emphasizes the energy split-up due to $p - d$ hybridization between transition metal ions and O atoms as shown in Figure 1.6.

Bethe gave the concept of crystalline field in 1929. The highly localized d - orbitals and their interactions with the spin, orbital and lattice degrees of freedom can be modelled by the crystal field theory.

A single line energy diagram may be drawn to show the energy splittings with reference to the the central free ion. Degeneracy of a transition metal ion is lifted by

the octahedral arrangement between the central TM and six surrounding O ions in an octahedral field. Electric, magnetic fields and pressure on the octahedral complex perturbs these energy levels due to a change in the crystal field.

Splitting of energy levels is represented as Δ . The value of Δ depends upon the position and radii of cations and surrounding anions in a crystal. The spherically symmetric crystalline field provides the central energy. The splitting energies are raised by the perturbations initiated by crystal field of TM cation and O anions.

The value of Crystal Field Split- Off Energy (CFSE), also known as Δ , varies for octahedral, tetrahedral or other interactions in TMOs. The insulator-metallic behavior in ABO_3 perovskites is due to localization vs. delocalization resulting from crystal field. The electrons in the e_g are at higher electron levels than the electrons at t_{2g} due to the position of O atoms in crystals.

The partial lifting of double degeneracy of e_g orbital energy states can also lead to distortions resembling Jahn-Teller effect if there are enough electrons to fill these levels. The displacement of TM cations vs. O anions stabilizes the crystalline system with $dz^2 - r^2$ electrons going to a lower energy state as they undergo less repulsion in comparison with $dx^2 - y^2$ electrons.

In case of cubic $BaTiO_3$, the energy splits into Δ_{oct} . The upper two orbitals are placed at $3/5\Delta_{oct}$ above the quantum center of gravity and the lower three are placed

at $2/5\Delta_{oct}$. These orbitals are assumed to be in a spherically symmetric field with the reference energy higher than the free ion energy.

However, the crystal field approach has its limitations as the CFSE fails to provide any contribution due to the electronic correlations in d^n orbitals in TMs. Values of crystal field in third row transition metal oxides are in the range of 2-3 eV.

An energy Hamiltonian can be based upon the CFT having energy components due to d_{xy} , d_{xz} and d_{yz} sub-orbitals known as t_{2g} and $d_{x^2-y^2}$, d_{z^2} sub-orbitals known as e_g :

$$H_{eff} = H_{hund} + H_{t_{2g}} + H_{e_g} \quad (1.1)$$

In Eq. 1.2, the subscripts i and j stand for the nearest atomic neighbors, $a_{i\gamma\sigma}^\dagger$ and $a_{j\gamma'\sigma}$ are the creation and annihilation operators representing small changes in energy of electrons occupying the atomic orbitals

$$H_{e_g} = \Delta \sum_i L_{iz} + \sum_{\langle ij \rangle \sigma \gamma \gamma'} t_{\gamma \gamma'}^{ij} (a_{i\gamma\sigma}^\dagger a_{j\gamma'\sigma}) + \sum_{\beta} H_{U_{\beta}} \quad (1.2)$$

$$\sum_{\beta} H_{U_{\beta}} = H_U + H_{U_{t_{2g}}} + H_{U_{e_g}} \quad (1.3)$$

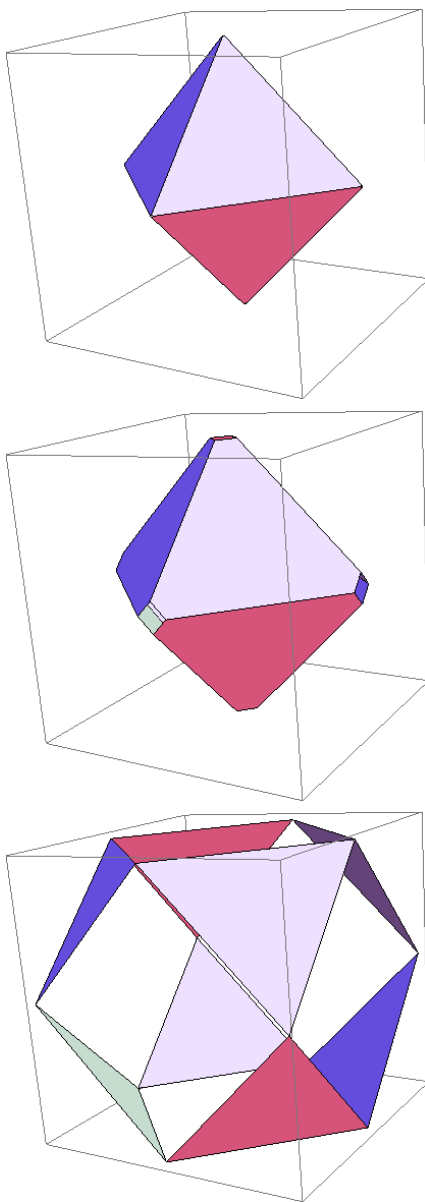


Figure 1.5: Octahedral cages formed between TM and O atoms. Top: Octahedral cage with cubic symmetry. Middle: octahedral cage with small strain. Bottom: octahedral cage with a large strain.

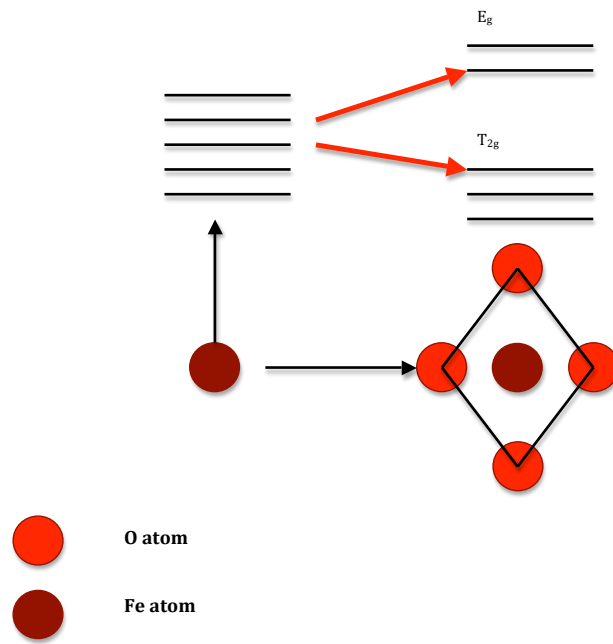


Figure 1.6: The crystal field split-off and lifting of the energy degeneracy in a cubic TMO.

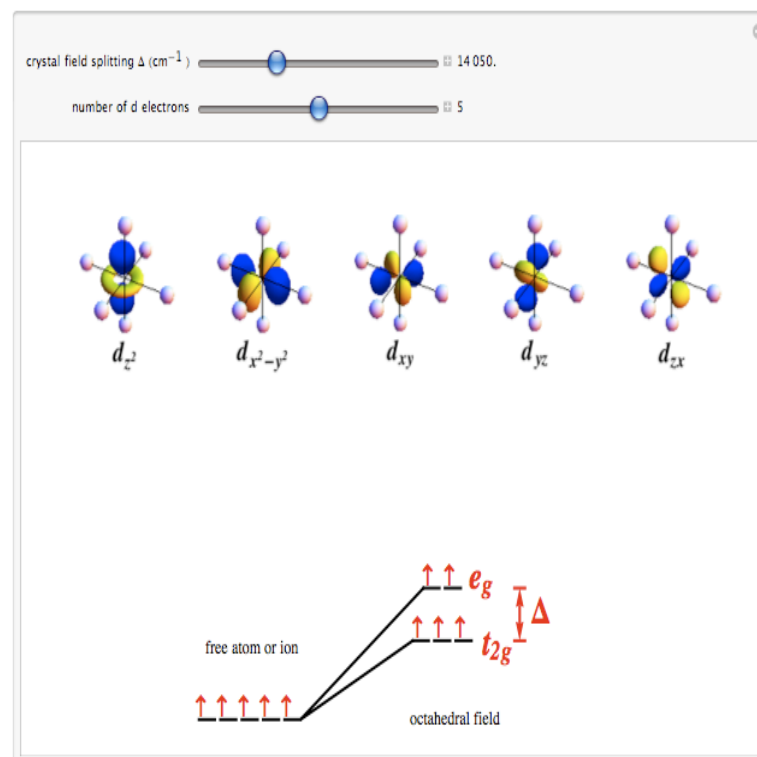
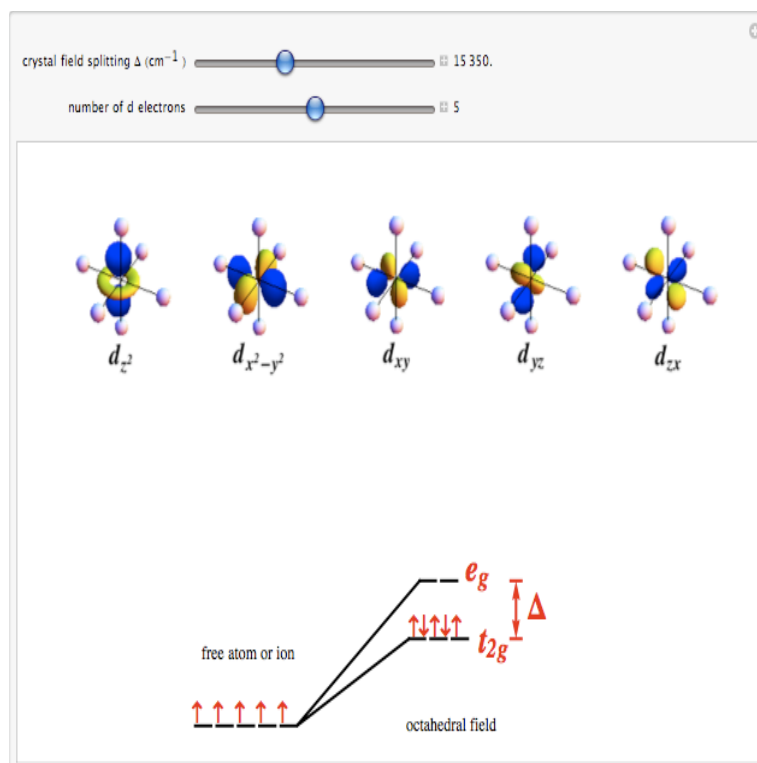


Figure 1.7: Top: Figure shows the crystal field and spin alignment before strain. Bottom: Figure shows new spin alignment after strain.

1.1.4 Chemical Bonding in TMOs

In electrostatic theory, the cations and anions are chemically bonded and approximated as point charges or point dipoles. In a vacuum state and free of any field or external strain, the d -orbitals of a transition metal ion are energetically degenerate. Energies of these atomic orbitals are raised with the approach of the O ions or negative field affected by the nature of the chemical bonding.

In a ground state, the force of attraction between the positively charged TM ion and negatively charged O ion is altered by the combination of ionic and covalent components of chemical bonding.

Chemical bonding in oxides of transition metals is a combination of ionic and covalent bonding. Covalent bonding in transition metal oxide like $BaTiO_3$ and rutile TiO_2 results in d^0 orbitals. The Mott insulators result due to highly localized nature of TM orbitals. Transition from metallic to a non-metallic state in TMOs occurs due to large contribution of ionic bonding. The higher percentage of ionic bonding in $BaFeO_3$ results in small band gap.

In TMs, electron localization induces strong electron correlations affecting the chemical bonding in TMOs. Pressure-induced transitions in TMOs provide an increase in the electron wavefunction overlaps between the neighbors to induce a change from

the localized to an itinerant behavior. The itinerant behavior results in spin polarized states.

The chemical bonding between the *TM d* and *O p* orbitals can result in significant overlap due to covalent bonding and no overlap due to ionic bonding for *Ti-Fe* TM series. Electrons in ABO_3 may be localized, delocalized or remain partially localized due to a delicate balance between the covalent and ionic bonding affecting the Hund energy and crystal field stabilizing energy.

Cubic $BaTiO_3$ is an insulator with AFM state due to covalent bonding. Whereas cubic $BaFeO_3$ is a charge-transfer type insulator with a FM state due to *Fe*.

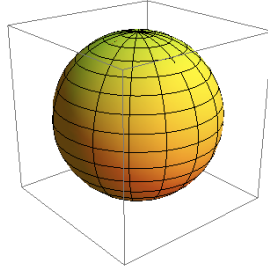
A Mott insulator with antiferromagnetic, charge-transfer type insulator with paramagnetic and conductor with ferromagnetic spin polarization is due to a varying electron exchange and correlation influenced by the chemical bonding.

1.1.5 *d* Orbitals in TMOs

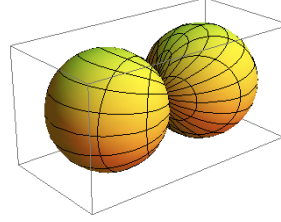
Atomic orbital function also expresses the probability of finding an electron in a particular region around the atomic nucleus.

The angular part of electron wave function can be expressed by spherical harmonics.

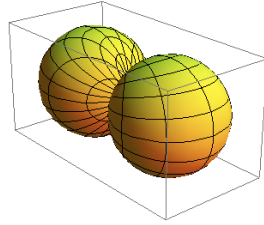
Type of atomic orbital: $1s$



Type of atomic orbital: $2p_x$



Type of atomic orbital: $2p_y$



Type of atomic orbital: $2p_z$

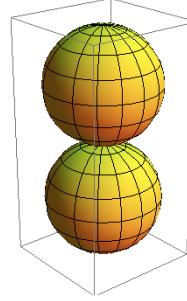


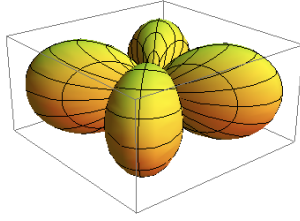
Figure 1.8: The $1s$ and $2p_x$, $2p_y$ and $2p_z$ orbitals.

There is a 5-fold degeneracy due to the spherical potential on an isolated transition metal in a vacuum.

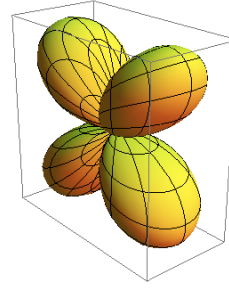
In the case of unstrained and perfect octahedral symmetry the d orbital is split into a pair of sub-orbitals. The dz^2 and $d_{x^2-y^2}$ and d_{xy} , d_{xz} , and d_{yz} sub-orbitals are split as two separate groups. Two higher energy orbitals and three lower energy orbitals are named differently in van Vleck, Mulliken and Bethe's notations [24].

The electron wave functions of e_g sub-orbitals pointing towards O^{2-} ions are located at higher energy than the t_{2g} which are pointing away from the O^{2-} ions. These partially degenerate sub-orbitals provide an additional degree of freedom [25].

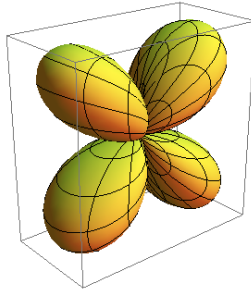
Type of atomic orbital: $3d_{xy}$



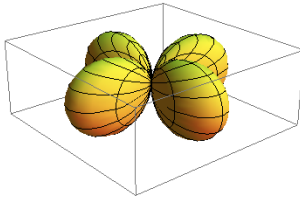
Type of atomic orbital: $3d_{yz}$



Type of atomic orbital: $3d_{zx}$



Type of atomic orbital: $3d_{x^2-y^2}$



Type of atomic orbital: $3d_z$

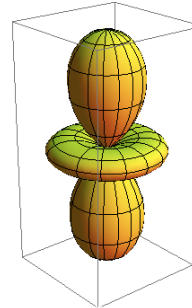


Figure 1.9: Five d orbitals are shown: d_{z^2} , $d_{x^2-y^2}$, d_{xy} , d_{yz} and d_{xz} .

Inside a d -orbital, the first of three electrons will fill the t_{2g} sub-orbital as per the Hund's rule to have their spins up. The fourth electron will fill the t_{2g} energy level with spin-down or will fill the e_g energy level with spin-up.

Highly localized d orbitals in a transition metal oxide, may result in high exchange

or correlation. Electrons in d orbitals experience the competitive forces [26] of the coulomb repulsion resulting in localization of the electrons at atomic lattice sites whereas the $p - d$ hybridization delocalizes these electrons. The delicate balance [27] between these two forces in transition metal oxides results in metal-insulator transitions accompanied with changes in their electronic properties. The TMOs of V , Mn and Cr possess the mix of covalent and ionic characteristics.

Figures 1.9 show the 3-dimensional plots of probability density of electrons having a varying shape due to spherical harmonics resulting from $l = 2$.

The perovskite type TMO such as $R(R = Ba, Ca)TiO_3$ is one of a prototype of the transition metal oxides having Ti transition metal in center of a cage formed by O atoms. In these transition metal oxides, Ti ion has t_{2g} configuration which are three-fold degenerate.

The distortions appear as changes in energies of the distorted octahedral. Distortions also produce additional splittings in the energy of e_g and t_{2g} sub-orbitals.

For TiO_2 , the e_g and t_{2g} energies are located near the bottom of conduction band. The e_g is located approximately 2 eV higher in energy as compared with t_{2g} . The partial density of state curve for t_{2g} is steeper and the one for e_g has higher width and low amplitude. The nature of the curve suggests that density of states pertaining to t_{2g} is highly localized [27].

1.1.6 Spin Exchange in TMOs

Exchange interaction effects were discovered independently by physicists Werner Heisenberg and P. A. M. Dirac in 1926. Electrons are fermions and electron spins polarized in opposite direction have more mutual repulsion than electrons with spins polarized in same direction.

The term J_H is the Hund's energy which shows that t_{2g} electrons are localized very well in the singlet or triplet form depending upon the number of electrons available in cubic ABO_3

$$H_{hund} = J_H \sum_i S_i S_i^{t_{2g}} \quad (1.4)$$

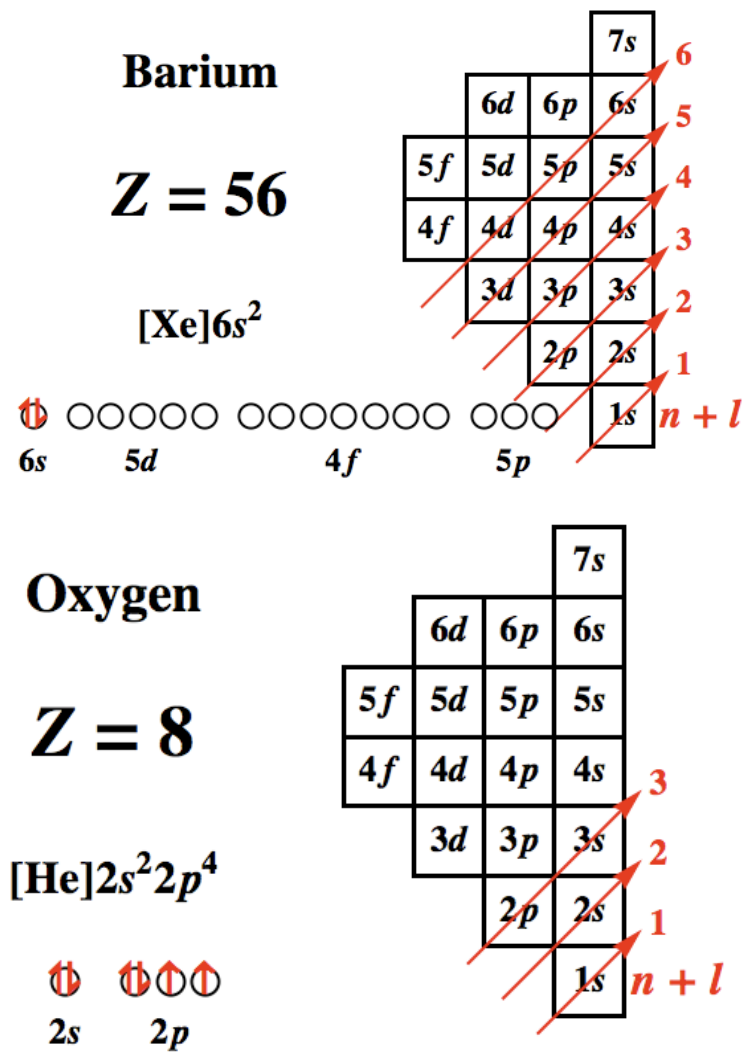
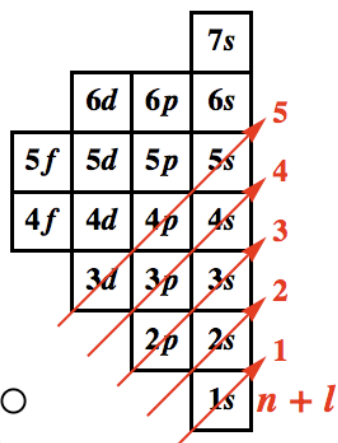
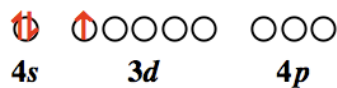


Figure 1.10: Electronic configuration of Ba and O atoms.

Scandium

$Z = 21$

$[\text{Ar}]4s^23d^1$



Titanium

$Z = 22$

$[\text{Ar}]4s^23d^2$

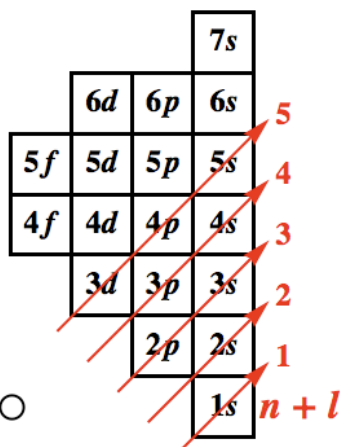
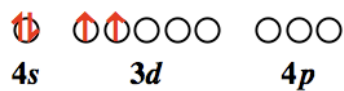
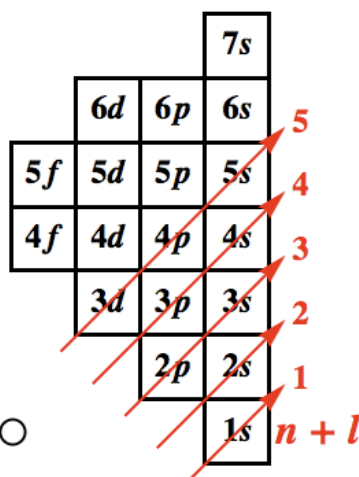
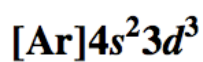


Figure 1.11: Electronic configuration of *Sc* and *Ti* atoms.

Vanadium

$$Z = 23$$



Chromium

$$Z = 24$$

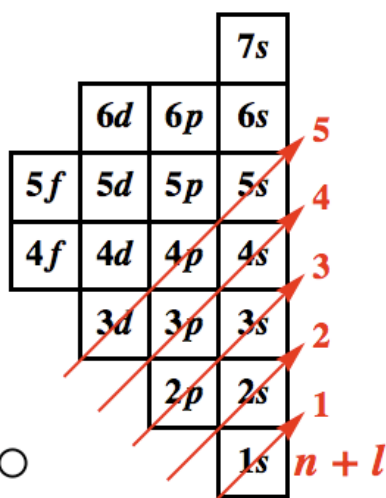
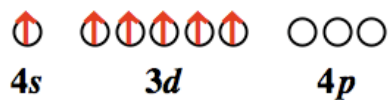
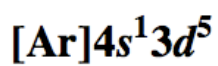
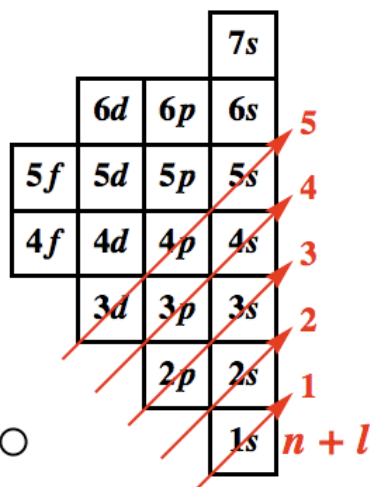
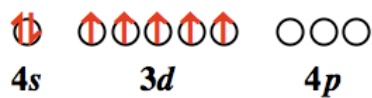
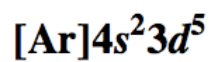


Figure 1.12: Electronic configuration of V and Cr atoms.

Manganese

$$Z = 25$$



Iron

$$Z = 26$$

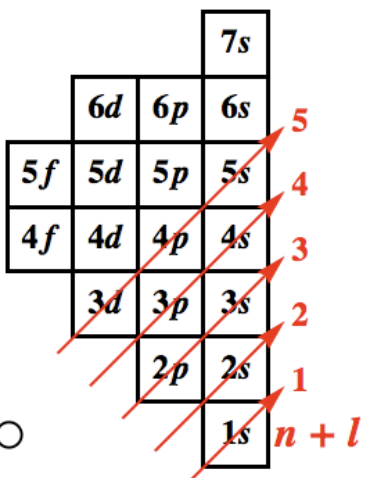
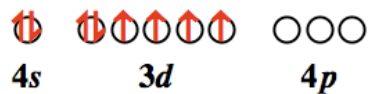
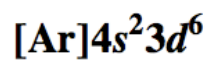


Figure 1.13: Electronic configuration of *Mn* and *Fe* atoms.

1.2 Introduction to CRYSTAL09 Program

The CRYSTAL09 employs *ab-initio* computational techniques for computing the electronic structure and properties of crystalline materials. It is based upon the linear combination of atomic orbitals (LCAO). The CRYSTAL09 code possesses basis sets, potentials, geometry optimization techniques to compute the single point energy and properties of a variety of crystalline structures.

1.2.1 Computational Parameters

The high-pressure cubic and tetragonal phases of $BaFeO_3$ were computed by employing BILLY program in combination with CRYSTAL code.

Later, CRYSTAL09 code was employed to compute the elastic constants and bulk moduli of cubic and tetragonal $BaFeO_3$ phases. The computational parameters were kept consistent throughout these computations. Shrinking factor was adjusted to 16 32, tolerances on SCF were kept as 9 9 9 9 18 and the tolerances on energy gradient were also set to 9.

The bulk moduli are computed by employing the ELASTCON (second-order elastic constants) and EOS (equation of state).

1.2.2 ELASTCON Algorithm

The computation of elastic constants and the bulk modulus is an automated process in the ELASTCON program. It begins with determining the crystalline symmetry of tetragonal $BaTiO_3$ and deformations are applied to exploit the available symmetries. The analytic first derivative and the numerical second derivative of total energy are computed for each deformation. Levenberg Marquardt (LM) curve fitting [29] is applied to compute the elastic constants. The computation of the elastic constants for tetragonal $BaTiO_3$ is complicated due to its crystalline geometry and the position of the atoms in the perovskite crystalline structure. With the lowering of crystalline symmetry, the number of independent elastic constants increases and geometry optimization steps are also increased.

The linear deformation of solids is expressed by Hooke's law as:

$$\sigma_{ij} = \sum_{kl} C_{ijkl} \epsilon_{kl} \quad (1.5)$$

where $i, j, k, l = 1, 2, 3$, $\sigma_{i,j,k,l}$, $\epsilon_{k,l}$ and $C_{i,j,k,l}$ are stress, strain and second-order elastic constant tensors.

The second-order elastic constants may be computed with different techniques. Molecular dynamics [30] and *ab-initio* computational techniques are two prominent methods to compute the elastic constants and bulk modulus. The *ab-initio* computational

techniques compute the second-order elastic constant (SOEC) from the total energy. The elastic constants can be computed from the Taylor series expansion of the total energy with respect to the applied strains, as shown in Eq. (1.6). The Taylor series terms up to the second-order may be utilized for the estimation of the elastic constants if the strains are very small and the higher order terms have negligible effects on the computational results.

$$E(V, \epsilon) = E(V_0) + \sum_{\alpha} \sigma_{\alpha} \epsilon_{\alpha} + \frac{V}{2} \sum_{\alpha\beta} C_{\alpha\beta} \epsilon_{\alpha} \epsilon_{\beta} + \dots \quad (1.6)$$

The terms $\alpha, \beta = 1, \dots, 6$ express the elastic constants in Voigt notation and V_0 is the equilibrium volume. The second term in Eq. (1.6) may be ignored if the crystalline geometry of the system is fully optimized. The third term in Eq. (1.6) can be rewritten to express the elastic constant as the second derivative of the total energy with respect to the applied strain in a crystalline direction

$$C_{\alpha\beta} = \frac{1}{V} \left. \frac{\partial^2 E}{\partial \epsilon_{\alpha} \partial \epsilon_{\beta}} \right|_0. \quad (1.7)$$

In Eq. (1.7), the terms $C_{\alpha\beta}$, E , and V express the elastic constant tensor, energy and volume of the crystalline structure, respectively.

The *ab-initio* computations are achieved by calculating the analytic first derivative and numerical second derivative of the total energy with respect to the applied strain.

The appropriate number of strains are applied in a systematic manner, the elastic constants are calculated, and the compliance coefficients are computed from Eq. (1.8). The compliance coefficients are then utilized for the computation of the bulk modulus as shown in Eq. (1.9).

$$[S] = [C]^{-1} \quad (1.8)$$

$$B = 1/(S_{11} + S_{22} + S_{33} + 2(S_{12} + S_{13} + S_{23})). \quad (1.9)$$

The terms S_{ij} and B in Eq. (1.9) express the compliance tensor elements and bulk modulus, respectively.

1.2.3 EOS Algorithm

The EOS algorithm utilizes systematic changes [31] in the volume around the optimized equilibrium state of a crystalline structure. The EOS calculations are carried out by selecting a range of volumes around a minimum total energy at an equilibrium state of the tetragonal $BaTiO_3$ crystalline structure. The EOS algorithm permits selection of a range of volumes and a number of volumes within that range. At each of the volumes in the range, the constant volume optimization is carried out. The energy vs. volume results are curve-fitted to an EOS such as Murnaghan EOS [32] given in Eq. (1.10).

The Crystal09 code [33] can accomplish an optimization of the internal co-ordinates

and lattice parameters while keeping the volume constant (see ref. [33] for the detailed description of CVOLOPT option of geometry optimization). The EOS algorithm in CRYSTAL09 computes the energy for a range of volumes around the optimized equilibrium volume, and is equipped with a wide variety of equations of state such as Birch Murnaghan, 3rd order Birch Murnaghan, logarithmic, Vinet and polynomial. In this paper, the 3rd order Birch Murnaghan equation of state algorithm was utilized for computing the bulk modulus from the energy vs. volume computations as expressed in Eq. (1.10):

$$E(V) = B_o V_o \left[\frac{1}{B'(B' - 1)} \left(\frac{V_o}{V} \right)^{B'-1} + \frac{V}{B'V_o} - \frac{1}{B' - 1} \right] + E_o. \quad (1.10)$$

In Eq. (1.10), V_o represents the volume at the minimum energy, B_o is the bulk modulus at pressure $P = 0$, B' is the derivative of the bulk modulus B at $P = 0$ and E_o is the minimum energy. The optimization of crystalline geometry at each step is done during energy-volume (E-V) calculations. The bulk modulus results are obtained with Levenberg-Marquardt curve fitting of the E vs. V computations.

1.2.4 BILLY Program

Billy script [5] is employed within CRYSTAL09 code to compute the optimized crystalline structure of $BaFeO_3$. There are various options available within BILLY pro-

gram. The optimized crystalline structure is determined in BILLY program by employing the small variation in the lattice parameter value for a range from .0001 to 5 percent of a lattice parameter value. The values of the energy within a given range of the lattice parameter are curve-fitted by a polynomial of third degree. The optimized lattice parameter is then computed at the lowest energy by the nonlinear least square curve-fitting of the energy values obtained.

Accuracy of BILLY program was crosschecked by employing the non-linear least square curve fitting using MATHEMATICA. The values of optimized lattice parameters computed with BILLY script and MATHEMATICA showed a significant agreement in the optimized values of lattice parameters.

1.3 Thesis statement

The electronic structure, elastic and ferroic properties of 3-*d* transition metal oxide perovskites are computed. A coupling between the crystalline structure, electronic charge and spin has been explored. The computational results of electronic structure, elastic and ferroic properties are compared with experimental values where possible.

The pursuit of electronic spin based electronics may be addressed by the exploration and development of materials which enable spin states to be manipulated through

elastic strain. The electronic structure, elastic and ferroic properties of 3-d transition metal oxide perovskites are of particular interest. *ab-initio* computational modeling is a valuable instrument to explore these materials. Model results will be compared with experimental values where possible.

1.4 Research outline

We performed *ab-initio* computations to explore the electronic structure and properties of 3-*d* transition metal oxides. Hartree Fock (HF), density functional theory (DFT) and hybrid potentials were employed to determine the electronic structure of cubic and tetragonal perovskites of *Ti* and *Fe* transition metals. The electronic structure and elastic properties of rutile TiO_2 were also computed. Moreover, oxides of 3-*d* transition metals of *Sc*, *Ti*, *V*, *Cr*, *Mn* and *Fe* were chosen to compute the ferromagnetic and antiferromagnetic properties resulting from spin exchange.

Chapter 2 consists of the *ab-initio* computations of lattice parameters, elastic constants and bulk moduli of tetragonal $BaTiO_3$. A variety of potentials, basis sets and algorithms were employed to expand the scope of our computational effort. Following are the main points of our computational research on tetragonal $BaTiO_3$.

† *ab-initio* computations are carried out for determining the electronic structure and elastic properties of tetragonal $BaTiO_3$.

† Optimized lattice parameters, elastic constants and bulk moduli of tetragonal are computed with two basis sets, a variety of potentials. The ELASTCON and EOS programs are employed for computing second-order elastic constants and bulk moduli.

† The computational values of the lattice parameters, elastic constants and bulk moduli are compared with experimental values where possible.

Chapter 3 contains the computations of the optimized electronic structure and properties of rutile TiO_2 . These computations were carried out to confirm the merit of the computational methods employed on tetragonal $BaTiO_3$ and rutile TiO_2 . Following are the main points of our computational research on rutile TiO_2 .

† Computations are performed on rutile TiO_2 to understand the causes of disagreement between the experimental and computational values of lattice parameters, elastic constants and bulk moduli.

† *ab-initio* computations are carried out to determine the electronic structure and elastic properties of tetragonal rutile TiO_2 .

† The computations are attempted with new hybrid potentials that introduce the

effective exchange and correlation effects required for rutile TiO_2 computations [34].

† A comparison between the experimental and computational values of lattice parameters, elastic constants and bulk moduli is performed.

† The merit of the computational methods is crosschecked by comparing the experimental and computational results.

In chapter 4, the optimized crystalline structure and elastic properties of cubic and tetragonal $BaFeO_3$ crystalline structures are explored. The theoretical values of lattice parameters, elastic constants and bulk moduli from other sources are presented for comparison where possible.

† *ab-initio* computations are carried out for determining the electronic structure and elastic properties of novel cubic and tetragonal $BaFeO_3$. A wide variety of basis sets and potentials are employed.

† The optimized lattice parameters, elastic constants and bulk moduli are computed for the cubic and tetragonal $BaFeO_3$.

† Computational values of bulk moduli computed from second-order elastic constants and equation of state are compared.

Chapter 5 contains the computations about the coupling between the crystalline structure and FM/AFM properties. These computations are performed on cubic $BaScO_3$, $BaTiO_3$, $BaVO_3$, $BaMnO_3$, $BaCrO_3$ and $BaFeO_3$. We employed the CRYSTAL09 code to detect the interdependence between the FM/AFM spin and external pressure on cubic $BaScO_3$, $BaTiO_3$, $BaVO_3$, $BaMnO_3$, $BaCrO_3$ and $BaFeO_3$. Spin transitions may be coupled due to a significant overlap in atomic orbitals. We try to hydrostatically compress and expand the crystalline structures of $BaVO_3$, $BaMnO_3$ and $BaCrO_3$ as well as $BaScO_3$, $BaTiO_3$ and $BaFeO_3$.

† The computations of the FM/AFM energy are done for the optimized cubic crystalline structure of each oxide.

† The computations are repeated for a variety of material systems to explore the interaction between the crystalline lattice structure and FM/AFM spin configuration.

† *ab-initio* computations of the FM/AFM energy are carried out for HF, DFT and hybrid potentials to check the consistency.

† The coupling is explored between electron spin transitions, atomic orbitals and hydrostatic pressure on the cubic crystalline structure of $BaScO_3$, $BaTiO_3$, $BaVO_3$, $BaMnO_3$, $BaCrO_3$ and $BaFeO_3$.

Chapter 6 contains a detailed summary, conclusions and future research on the tran-

sition metal oxides. The challenges in the optimized crystalline structure, elastic properties are discussed. The causes of the disagreement between the computational and experimental values are highlighted. The significance of an agreement between the computational values obtained second order elastic constants and bulk moduli is also discussed for crystalline systems having no experimental values.

References

- [1] Gordon E. Moore. *Electronics*, 38:4, 1965.
- [2] Lihui Wang. Quantum mechanical effects on MOSFET scaling limit. *PhD thesis, Georgia Institute of Technology*, page 191, 2006.
- [3] Amit Chaudhry and J. N. Roy. *Journal Of Semiconductor Technology And Science*, 10:20–27, 2009.
- [4] Qiang Chen and James D. Meindl. *Nanotechnology*, 15:S549–55, 2004.
- [5] R. Dovesi, V. R. Saunders, C. Roetti, R. Orlando, C. M. Zicovich-Wilson, F. Pascale, B. Civalleri, K. Doll, N. M. Harrison, I. J. Bush, Ph. D’Arco, and M. Llunell. *CRYSTAL2006 User’s Manual*. University of Torino, University of Torino, Torino, Italy, 2006.
- [6] Mahboubeh Hortamani, Leonid Sandratskii, Peter Kratzer, and Ingrid Mertig. *New Journal of Physics*, 11:1–23, 2009.

- [7] Baibich M. N., Broto J. M., Fert A., and Chazelas J. *Phys. Rev. Lett.*, 61:2472–2475, 1988.
- [8] Jagadeesh S. Moodera, GuoXing Miao, and Tiffany S. Santos. *Physics Today*, 63:46–51, 2010.
- [9] Alexander M. Grishin Fumiaki Mitsugi, Yukihiro Yamagata. *Jpn. J. Appl. Phys.*, pages 5418–5420, 2000.
- [10] Min Shen, Saikin S., and MingCheng Cheng. *Nanotechnology, IEEE Transactions on*, 4:40–44, 2005.
- [11] Ferreira R. and Bastard G. *Phys. Rev. B*, 43:9687–9691, 1991.
- [12] Jeroen Van Den Brink and Daniel I. Khomskii. *J. Phys. Condens. Matter*, 20:1–12, 2008.
- [13] Nicola A. Hill. *AIP Conference Proceedings*, 535:372–382, 2000.
- [14] CeWen Nan, M. I. Bichurin, Shuxiang Dong, D. Viehland, and G. Srinivasan. *J. App. Phy.*, 103:031101(1–25), 2008.
- [15] Sinha K. P. and Upadhyaya U. N. *Phys. Rev.*, 127:432–439, 1962.
- [16] Qing Hua Qin. *Green’s Function and Boundary Elements of Multifield Materials*. Elsevier, University of New South Wales, 2007.
- [17] Chun Gang Duan, Julian P. Velez, R. F. Sabirianov, W. N. Mei, S. S. Jaswal, and E. Y. Tsymbal. *Applied Physics Letters*, 92:1–3, 2008.

- [18] Evgeny Y Tsymbal, Oleg N Mryasov, and Patrick R LeClair. *J. Phys. Condens. Matter*, 15:R109–R142, 2003.
- [19] J. P. Velev, P. A. Dowben, E. Y. Tsymbal, S. J. Jenkin, and A.N. Caruso. *Surface Science Reports*, 63:400–425, 2008.
- [20] G.P. Berman, F. Borgonovi, V.N. Gorshkov, and V.I. Tsifrinovich. *Nanotechnology, IEEE Transactions on*, 4:14–20, 2005.
- [21] M. Catti, G. Sandrone, G. Valerio, and R. Dovesi. *Journal of Physics and Chemistry of Solids*, 57:1735–1741, 1996.
- [22] Garlid E. S., Hu Q. O., Chan M. K., Palmstrom C. J., and Crowell P. A. *Phys. Rev. Lett.*, 105:156–602, 2010.
- [23] Masaaki Tanaka. *Journal of Crystal Growth*, 278:25–37, 2005.
- [24] J. J. Zuckerman. *J Chem Ed*, 42:315, 1965.
- [25] Goodenough J. Electron-Lattice Interactions in Manganese-Oxide. *Perovskites, Fundamental Materials Research*, pages 127–133, 2002.
- [26] C. N. R. Rao. *Annual Review of Physical Chemistry*, pages 291–326, 1989.
- [27] Y. Tokura and N. Nagaosa. *Science*, 288:462–468, 2000.
- [28] Wolfram. *MATHEMATICA*, V. 07.
- [29] W. Marquardt. *SIAM J. Appl. Math.*, 11:431–44, 1963.

- [30] A. Khalal, D. Khatib, and B. Jannot. *Physica B*, pages 343–47, 1999.
- [31] Warren F. Perger. *Int. J. Quant. Chem.*, pages 1916–1922, 2010.
- [32] F. D. Murnaghan. *Proc. Natl. Acad. Sci. (USA)*, 30(9):244–7, 1944.
- [33] R. Dovesi, V. R. Saunders, C. Roetti, R. Orlando, C. M. Zicovich-Wilson, F. Pascale, B. Civalleri, K. Doll, N. M. Harrison, I. J. Bush, Ph. D’Arco, and M. Llunell. *CRYSTAL2006 User’s Manual*. University of Torino, University of Torino, Torino, Italy, 2006.
- [34] B. H. O’Connor and S. Pratapa. *Advances in X-ray Analysis*, 45:158–165, 2002.

Chapter 2

Crystalline Geometry and Elastic Properties of Tetragonal $BaTiO_3$

2.1 Introduction

The perovskites are an important class of materials with applications in the fields of memory, logic design and switching. However, the theoretical exploration of these materials is not on par with their technological importance. Crystalline $BaTiO_3$ possesses a perovskite geometry which may occur in cubic, tetragonal, rhombohedral or orthorhombic crystalline phases. There is a general lack of data on the mechanical properties of all phases of $BaTiO_3$. However, there have been attempts [1, 2, 3, 4,

5, 6, 7] to understand the electronic and mechanical properties of this material. For example, the computation of elastic constants and the bulk modulus was reported by Piskunov *et al* [8] for cubic $BaTiO_3$ using *ab-initio* computational methods.

At room temperature, $BaTiO_3$ has tetragonal crystalline geometry. In the past, the elastic constants and bulk modulus of tetragonal $BaTiO_3$ could not be computed due to the complexity of the system. Due to recent advancements in basis sets, geometry optimization, and computational power, *ab-initio* computational techniques can now be employed. In this paper, the computations of elastic constants and the bulk modulus of tetragonal $BaTiO_3$ are obtained with *ab-initio* Hartree Fock (HF), density functional theory (DFT) and hybrid potentials using two different basis sets.

An important factor that affects the efficiency and accuracy of computation is the determination of the optimized geometry of the crystalline structure. The geometry optimization is an essential step for calculating elastic constants and bulk moduli because it is assumed that all displacements are made relative to a system in equilibrium. The total geometry optimization finds both the atomic positions and lattice parameters of the unit cell which minimize the total energy. In addition, the geometry optimization in the CRYSTAL09 code [9] used here has features which make it an efficient program for calculating mechanical properties. For example, there is an option which permits optimization of the system at constant volume, which facilitates

the determination of a total energy vs. volume curve which is necessary for equation of state (EOS) calculations.

As a cross-check, the bulk modulus is found independently with the program ELASTCON [10] and a separate EOS program. The ELASTCON algorithm determines the number of crystalline deformations based upon the crystalline geometry of tetragonal $BaTiO_3$. Geometry optimization of the crystalline structure is carried out after each deformation. The analytic first derivative, numerical second derivative and Levenberg Marquardt (LM) curve fitting is performed in sequence to compute elastic constants for the tetragonal $BaTiO_3$. A detailed discussion of the ELASTCON program can be found in refs. [10, 11].

The task of crystalline geometry optimization of the perovskite $BaTiO_3$ has remained a challenge because the crystalline system undergoes a sudden decrease in energy when it is deformed. This sudden decrease in the strain vs. energy computations has been reported earlier [1, 12, 13] and was observed with the ELASTCON algorithm. Detailed energy vs. strain computations were carried out to explore this sudden decrease in energy.

2.1.1 ELASTCON Algorithm

The computation of elastic constants and the bulk modulus is an automated process in the ELASTCON program. It begins with determining the crystalline symmetry of tetragonal $BaTiO_3$ and deformations are applied to exploit the available symmetries. The analytic first derivative and the numerical second derivative of total energy are computed for each deformation. Levenberg Marquardt (LM) curve fitting [14] is applied to compute the elastic constants. The computation of the elastic constants for tetragonal $BaTiO_3$ is complicated due to its crystalline geometry and the position of the atoms in the perovskite crystalline structure. With the lowering of crystalline symmetry, the number of independent elastic constants increases and geometry optimization steps are also increased.

The linear deformation of solids is expressed by Hooke's law as:

$$\sigma_{ij} = \sum_{kl} C_{ijkl} \epsilon_{kl} \quad (2.1)$$

where $i, j, k, l = 1, 2, 3$, $\sigma_{i,j,k,l}$, $\epsilon_{k,l}$ and $C_{i,j,k,l}$ are stress, strain and second-order elastic constant tensors.

The second-order elastic constants may be computed with different techniques. Molecular dynamics [15] and *ab-initio* computational techniques are two prominent methods to compute the elastic constants and bulk modulus. The *ab-initio* computational

techniques compute the second-order elastic constant (SOEC) from the total energy. The elastic constants can be computed from the Taylor series expansion of the total energy with respect to the applied strains, as shown in Eq. (2.2). The Taylor series terms up to the second-order may be utilized for the estimation of the elastic constants if the strains are very small and the higher order terms have negligible effects on the computational results.

$$E(V, \epsilon) = E(V_0) + \sum_{\alpha} \sigma_{\alpha} \epsilon_{\alpha} + \frac{V}{2} \sum_{\alpha\beta} C_{\alpha\beta} \epsilon_{\alpha} \epsilon_{\beta} + \dots \quad (2.2)$$

The terms $\alpha, \beta = 1, \dots, 6$ express the elastic constants in Voigt notation and V_0 is the equilibrium volume. The second term in Eq. (2.2) may be ignored if the crystalline geometry of the system is fully optimized. The third term in Eq. (2.2) can be rewritten to express the elastic constant as the second derivative of the total energy with respect to the applied strain in a crystalline direction

$$C_{\alpha\beta} = \frac{1}{V} \left. \frac{\partial^2 E}{\partial \epsilon_{\alpha} \partial \epsilon_{\beta}} \right|_0. \quad (2.3)$$

In Eq. (2.3), the terms $C_{\alpha\beta}$, E , and V express the elastic constant tensor, energy and volume of the crystalline structure, respectively.

The *ab-initio* computations are achieved by calculating the analytic first derivative and numerical second derivative of the total energy with respect to the applied strain.

The appropriate number of strains are applied in a systematic manner, the elastic constants are calculated, and the compliance coefficients are computed from Eq. (2.4). The compliance coefficients are then utilized for the computation of the bulk modulus as shown in Eq. (2.5).

$$[S] = [C]^{-1} \quad (2.4)$$

$$B = 1/(S_{11} + S_{22} + S_{33} + 2(S_{12} + S_{13} + S_{23})). \quad (2.5)$$

The terms S_{ij} and B in Eq. (2.5) express the compliance tensor elements and bulk modulus, respectively.

2.1.2 EOS Algorithm

The EOS algorithm utilizes systematic changes [11] in the volume around the optimized equilibrium state of a crystalline structure. The EOS calculations are carried out by selecting a range of volumes around a minimum total energy at an equilibrium state of the tetragonal $BaTiO_3$ crystalline structure. The EOS algorithm permits selection of a range of volumes and a number of volumes within that range. At each of the volumes in the range, the constant volume optimization is carried out. The energy vs. volume results are curve-fitted to an EOS such as Murnaghan EOS [16] given in Eq. (2.6).

The Crystal09 code [9] can accomplish an optimization of the internal co-ordinates

and lattice parameters while keeping the volume constant (see ref. [9] for the detailed description of CVOLOPT option of geometry optimization). The EOS algorithm in CRYSTAL09 computes the energy for a range of volumes around the optimized equilibrium volume, and is equipped with a wide variety of equations of state such as Birch Murnaghan, 3rd order Birch Murnaghan, logarithmic, Vinet and polynomial. In this paper, the 3rd order Birch Murnaghan equation of state algorithm was utilized for computing the bulk modulus from the energy vs. volume computations as expressed in Eq. (2.6):

$$E(V) = B_o V_o \left[\frac{1}{B'(B' - 1)} \left(\frac{V_o}{V} \right)^{B'-1} + \frac{V}{B'V_o} - \frac{1}{B' - 1} \right] + E_o. \quad (2.6)$$

In Eq. (2.6), V_o represents the volume at the minimum energy, B_o is the bulk modulus at pressure $P = 0$, B' is the derivative of the bulk modulus B at $P = 0$ and E_o is the minimum energy. The optimization of crystalline geometry at each step is done during energy-volume (E-V) calculations. The bulk modulus results are obtained with Levenberg-Marquardt curve fitting of the E vs. V computations.

2.2 Choice of basis sets

The selection of basis sets affects the calculation of the elastic constants and bulk modulus as reported in refs. [17, 18, 19, 20], particularly for a material such as *BaTiO₃*.

The first basis set chosen uses the 8-411d1 basis set for oxygen and HAYWSC ECP basis set for Ba and Ti atoms from the Crystal06 basis set library [9] because of its prior use in $BaTiO_3$ [8, 19]. For comparison, a second basis set, used previously for urea [17], was selected using a 6-31d1 set for oxygen and the HAYWSC ECP for Ba and Ti. We have named the combination of basis sets 8-411d1 and HAYWSC ECP as basis set 1 and 6-31d1 and HAYWSC ECP as basis set 2.

As will be shown, the variation in the values of elastic constants and bulk modulus confirms the fact that the choice of basis sets can severely affect the results. The choice of basis sets indicates a trade-off between the reliability of the results and the required computational time. Our approach is to check the credibility of the results by employing the basis sets in two different algorithms for the bulk modulus and comparing the results attained using these basis sets with each other and experiment. In contrast with 6-31d1, the 8-411d1 basis set is optimized to suit the nature of chemical bonding and atomic position of oxygen in the transition metal oxide $ScMnO_3$ [20]. The positions of the oxygen atoms in $ScMnO_3$ is similar to a $BaTiO_3$ unit cell which has a slightly off-centered Ti atom caged in the middle of an octahderal formed by six oxygen atoms. Because of this, basis set 1 (with the 8-411d1 set for oxygen) is expected to provide better results for $BaTiO_3$.

2.3 Selection of Hartree Fock, DFT and hybrid potentials

The computations of elastic constants and the bulk modulus were performed with the potentials HF, DFT and hybrid mixing of the former with the latter. The DFT and hybrid exchange correlation potentials are employed due to the lack of correlation of HF as reported in [8].

In a hybrid potential, there is a significant balance between the electron exchange and correlation for a crystal field formed between the transition metal Ti and O nearest neighbors. Due to the effect of the crystal field, the transition metal oxides are insulators with a significantly higher band gap. This is unlike the situation in oxygen with s and p electrons resulting in an itinerant and delocalized electron gas. These d electrons are highly localized resulting in wide band gaps and a significant change in the probability density of inter-atomic and intra-atomic orbitals. The electron localization affects the choice of a basis set for oxygen atoms. It is very important that the basis set is optimized for the valence electrons of oxygen which are covalently bonded with a transition metal.

Corà [19] utilized HF, DFT and hybrid exchange correlation potentials and a 8-411d1 basis set for the oxygen atom of cubic $BaTiO_3$ to calculate the lattice constants, bulk

modulus, and band gap. In that work, hybrid exchange and correlation potentials were used with an optimum percentage of HF exchange to account for the exchange and correlation parts of a highly correlated transition metal oxide. Hybrid exchange correlation potentials were found to be efficient, reliable and accurate in comparison with HF and DFT potentials. Based on that prior work, hybrid exchange potentials are used here for the tetragonal phase of $BaTiO_3$.

2.4 Discussion of computational results

The comparison of lattice constants a , c and the ratio c/a with experimental values is shown in Tables 2.1 and 2.2 for basis sets 1 and 2, respectively. The values of optimized lattice constants have shown a better agreement with the experimental values for basis set 1 than basis set 2. The computational values of a and c are slightly higher than the experimental values for DFT-PWGGA, DFT-BLYP, DFT-B3LYP and DFT-B3PW exchange correlation potentials employed with basis set 1. The optimized lattice constants a and c computed with HF and DFT-LDA exchange correlation are included for reference but are not expected to produce good agreement with experiment because the HF potential has no correlation and the DFT-LDA assumes a homogeneous electron gas. Interestingly, the optimized values of lattice constants a and c computed with basis set 2 show relatively large deviations from the experimental values of 3.99 and 4.03. The values of the optimized lattice constants a and c are equal for Hartree

Fock, exchange correlation and hybrid potentials employing basis set 2 as shown in Table 2.2. The fact that the tetragonal character has been missed for all potentials chosen suggests that basis set 2 is inadequate for this system. It is generally observed that local DFT (LDFT) exchange correlation potentials underestimate and nonlocal DFT (NLDT) exchange correlation potentials overestimate the lattice constants.

The computational values of elastic constants and bulk moduli show a trend of better agreement with the experimental values for basis set 1 than for basis set 2 as shown in Tables 2.3 and 2.4. Likewise, the comparison of computational values of bulk moduli computed with the EOS method indicates a better agreement with experimental values as shown in Tables 2.5 and 2.6 for basis set 1 relative to basis set 2, respectively. Also given in those tables are the values of the bulk modulus determined from the ELASTCON calculation and the agreement in B using two, independent, methods demonstrates the quality of the numerical methods employed. The computational values of bulk moduli in Table 2.5 calculated with basis set 1, for DFT-BLYP, PWGGA, B3LYP and B3PW potentials, fall within the range of experimental values of bulk modulus reported by [21]. The trend of consistency between the computational and experimental values of elastic constants and bulk moduli for basis set 1 vs. basis set 2 can also be seen by comparing results of elastic constants and bulk moduli shown in Figures 2.1-2.4. Comparing Figures 2.1 and 2.2, it is evident that basis set 2 produces results for the bulk modulus consistently larger than experiment, whereas the basis set 1 results effectively bracket experiment. Those figures also show the good

agreement between the two methods used to compute B . Figure 2.3 using basis set 1 shows better agreement with experiment for the elastic constants than basis set 2 used in Figure 2.4, particularly for the hybrid potentials. Figures 2.3 and 2.4 also indicate the spread in experimental values.

The discrepancy in results for lattice constants, elastic constants, and bulk modulus from basis set 2 and experiment [22, 23] is the consequence of the coefficients and exponents of the outermost Gaussian functions in a 6-31d1 basis set for the oxygen atom [17]. The 6-31d1 basis set was initially optimized for the oxygen atom in a unit cell of urea [17]. Therefore, the values of coefficients and exponents of these sp Gaussians are significantly larger to optimize the basis set for the requirements of hydrogen bonding and the peculiar position of the oxygen atom in a unit cell of urea [17, 18]. As a result, the values of elastic constants, particularly C_{11} , C_{33} and consequently bulk moduli (B), are largely affected by the values of these coefficients and exponents of sp type Gaussian functions. This is apparent from Table 2.4 where the values of C_{11} and C_{33} are consistently much larger than experiment and the results using basis set 1, Table 2.3. The basis sets are merely approximations of wavefunctions for valence electrons taking part in the chemical bonding. Therefore, the difference in the nature of chemical bonding in a urea vs. $BaTiO_3$ unit cell increases this inconsistency in the computational values for basis set 2 in comparison with basis set 1 and experimental values. The nature of chemical bonding is complex in $BaTiO_3$ and is different from the hydrogen bonding of urea. Moreover, the basis set 8-411d1 has

already been optimized for *ab-initio* computations of magnetic properties of $ScMnO_3$ [20]. The transition metal oxide like $BaTiO_3$ is a highly correlated material system due to the contracted nature of its d orbitals. The localized nature of transition metal oxides demands an oxygen basis set which is specially optimized to suit these transition metal oxides as in refs. [19, 20, 8].

Regarding basis set 1, the DFT-LDA have shown higher bulk modulus values due to the underestimation of the optimized lattice constant values, whereas the computations done with DFT-PWGGA and DFT-BLYP have shown lower values of bulk modulus due to the overestimation of optimized lattice constants. The computations done with hybrid potentials have shown the optimum values of bulk modulus as a consequence of the fact that the optimized lattice constants are comparatively close to the experimental values. In contrast with these results, the computational values of bulk modulus are higher with the basis set 2 as reported in Tables 2.5 and 2.6. The large increase in computational values of bulk modulus for the basis set 2 is attributed to the deviation in optimized lattice constants from the experimental values.

The computational results obtained with the PWGGA and hybrid potentials and basis set 1 are expected to be relatively accurate based on prior work for cubic $BaTiO_3$ [8] and rutile TiO_2 [10] crystalline systems. Moreover, the values of bulk modulus computed with ELASTCON and EOS algorithms are sufficiently close to each other for the same potential and basis set. These facts point to the importance of selecting a

variety of basis sets, potentials and algorithms and comparing the results. Therefore, the computational values of elastic constants computed with hybrid potentials are reliable if we ignore the variations in computations originating due to the order-disorder nature of the tetragonal $BaTiO_3$.

While comparing the results of elastic constants and bulk moduli obtained with basis set 1 vs. experimental values and basis set 2 vs. experimental values, the former shows a relatively better agreement in comparison with the latter [24, 25, 26, 27, 21]. This agreement is specifically significant in the case of a hybrid exchange and correlation potential used with basis set 1. The computational accuracy of hybrid exchange and correlation potentials has been reported by Corà [19]. The computational values of bulk moduli of cubic $BaTiO_3$ are highly accurate for the optimum percentage of Hartree Fock and DFT exchange and DFT correlation potential. The accuracy of a hybrid exchange correlation potential is ingrained in the exchange and correlation parts of hybrid potential which improves the lattice parameters, bulk modulus and band gap of cubic $BaTiO_3$ as reported in ref. [19].

Regarding any comparisons made of computational to experimental values, it should be noted that for this system there is a considerable variation between the experimental values of elastic constants and bulk moduli [24, 25, 27, 21]. These variations in computational and experimental values of elastic constants and bulk moduli [24, 26, 28, 6, 21] have been constantly observed in a variety of experimental results.

The causes of variation in experimental and computational values of elastic constants and bulk modulus may not be completely known. For the case of computational values, there are significant contributions due to an inefficient basis set, as in case of basis set 2, which makes the choice basis set so vital for the accuracy of results. On the other hand, the variation in computational and experimental values may not be an isolated effect due to the effect of the crystalline geometry on the computational and experimental values. (see A.0.1 and A.0.2 from Chemical Physics Letters)

2.5 Conclusions

The second order elastic constants and equations of state parameters were obtained for tetragonal $BaTiO_3$. We have observed close agreement between the values of the bulk modulus independently computed with ELASTCON and EOS methods. There have been attempts [29, 30, 31] to compute the different properties of tetragonal $BaTiO_3$. However, the computational values of elastic constants and bulk modulus of tetragonal $BaTiO_3$ are not available in the literature. We have further verified the computational accuracy of the results by implementing different algorithms, potentials and basis sets for rutile TiO_2 [10] and cubic $BaTiO_3$ [8]. The computational results obtained with these crystalline systems have provided additional evidence for the accuracy of the computational results presented here for tetragonal $BaTiO_3$. It has been observed that the crystalline structure and position of atoms in tetragonal

phase [32, 33] has increased the complexity of our computations. The agreement in computational values of bulk modulus provided an opportunity to verify the computational accuracy of elastic constants of tetragonal $BaTiO_3$.

The computational results of the optimized lattice constants obtained with basis set 1 and exchange correlation potential PWGGA and hybrid exchange correlation potentials B3LYP and B3PW have shown good agreement with respect to experiment. Therefore the employment of HF, DFT and hybrid exchange correlation potentials have essentially reinforced the computational merit of hybrid potentials as was found by Corà [19] for cubic phase $BaTiO_3$. The variations in computational values of elastic constants and bulk moduli are mainly attributed to the quality of basis sets and choice of potential. Basis set 1 is better designed to represent the interatomic and intra-atomic chemical nature of O , Ti and Ba for $BaTiO_3$ and, as expected, provided better agreement with experiment than basis set 2. It is important to note that differences in the sp orbital basis set for oxygen resulted in large differences in the C_{11} and C_{33} elastic constants. The inconsistency in computational results of elastic constants and bulk modulus for the two chosen basis sets compared with experimental values points at the importance of choosing an appropriate basis set for reliable and accurate *ab-initio* computations.

The order-disorder nature [33] of perovskite $BaTiO_3$ is another important factor that makes the computation of optimum values of the bulk modulus problematic, requiring

accurate basis sets and potentials. It has been observed that the computation of the bulk modulus for tetragonal $BaTiO_3$ is coupled intimately with the geometry optimization of its complex crystalline structure. Slight deviations in the values of optimized lattice constants a and c have shown large effects on the computational values of bulk moduli.

Based upon our computational results and the experimental data on tetragonal $BaTiO_3$, we conclude that there is a degree of consistency in the elastic properties. Further work on basis sets and exchange correlation potentials is necessary for improved comparison with experiment. Additionally, improvements in the experiments are important for continued progress on this important crystalline system.

Table 2.1: The values of relaxed lattice constants (in \AA), ambient volume (in \AA^3), and total energy, E (in a.u.), for tetragonal $BaTiO_3$. The computations were done by using Hartree-Fock, DFT LDA, PWGGA, BLYP, B3LYP and B3PW potentials using basis set 1. (see section 2.2).

	a	c	c/a	Vol.	E
HF	3.96	4.26	1.07	67.17	-307.5388
LDA	3.93	3.93	1.00	61.12	-307.8828
PWGGA	4.00	4.03	1.00	64.75	-309.5928
BLYP	4.05	4.14	1.02	68.12	-309.4749
B3LYP	4.01	4.10	1.02	66.15	-309.4084
B3PW	3.98	4.02	1.01	63.75	-309.5360
Exp. [22, 23]	3.99	4.03	1.01	64.16	-

Table 2.2: The values of relaxed lattice constants (in $\overset{\circ}{\text{\AA}}$), ambient volume (in $\overset{\circ}{\text{\AA}}^3$), and total energy, E (in a.u.), for tetragonal $BaTiO_3$. The lattice constants are computed with Hartree-Fock, DFT LDA, PWGGA, BLYP, B3LYP and B3PW potentials with basis set 2 (see section 2.2). O-631d1 basis set for O atom was not optimized for transition metal oxides resulting in the lattice parameters that differ significantly from experimental values.

	a	c	c/a	Vol.	E
HF	3.98	3.98	1.00	63.23	-307.4627
LDA	3.90	3.90	1.00	59.50	-307.7595
PWGGA	3.95	3.95	1.00	61.94	-309.4862
BLYP	4.00	4.00	1.00	64.06	-309.3636
B3LYP	3.97	3.97	1.00	62.66	-309.3082
B3PW	3.94	3.94	1.00	61.27	-309.4393
Exp. [22, 23]	3.99	4.03	1.01	64.16	-

Table 2.3: The elastic constants and bulk modulus computational results using the Hartree Fock and DFT LDA, PWGGA, BLYP, B3LYP and B3PW potentials with basis set 1 (see section 2.2). All values are in GPa.

	C_{11}	C_{12}	C_{13}	C_{33}	C_{44}	C_{66}	B
HF	308.	128.	88.	66.	121.	163.	62.
LDA	444.	93.	93.	444.	224.	224.	210.
PWGGA	354.	76.	56.	227.	175.	194.	139.
BLYP	285.	82.	58.	146.	73.	160.	110.
B3LYP	315.	95.	64.	166.	76.	177.	123.
B3PW	371.	89.	61.	228.	148.	204.	145.
Exp.[24]	211±6	107±5	114±8	160 ±11	56.2±1.7	127±4	125-141[21]
[25]	242.7	128.3	122.6	147.9	54.9	120.1	-
[27]	275.1	178.9	151.55	164.8	54.3	113.1	-
[26]	222.9	-	147.0	240.0	61.7	133.7	-

Table 2.4: The elastic constants and bulk modulus computations using the Hartree Fock, DFT LDA, PWGGA, BLYP, B3LYP and B3PW potentials with basis set 2 (see section 2.2). All values are in GPa.

	C_{11}	C_{12}	C_{13}	C_{33}	C_{44}	C_{66}	B
HF	408.	154.	154.	408.	185.	185.	239.
LDA	480.	129.	129.	480.	163.	163.	246.
PWGGA	445.	107.	107.	445.	214.	214.	220.
BLYP	382.	111.	111.	382.	185.	185.	201.
B3LYP	414.	123.	123.	414.	200.	200.	220.
B3PW	463.	119.	119.	463.	223.	223.	234.
Exp.[24]	211±6	107±5	114±8	160 ±11	56.2±1.7	127±4	125-141[21]
[25]	242.7	128.3	122.6	147.9	54.9	120.1	-
[27]	275.1	178.9	151.55	164.8	54.3	113.1	-
[26]	222.9	-	147.0	240.0	61.7	133.7	-

Table 2.5: Equation of state results for tetragonal $BaTiO_3$ with the Birch Murnaghan 3rd order equation. The energy-volume curve was fitted with eleven points and the range of volume around equilibrium was chosen as $\pm 10\%$ using basis set 1 (see section 2.2). The value of the bulk modulus, B_{EL} , as calculated from Eq. (2.5) is given in the last column for comparison.

	$B_{EOS}(\text{GPa})$	$V_o(\text{\AA}^3)$	$E_0(a.u.)$	$B_{EL}(\text{GPa})$
HF	62.	67.41	-307.5386	62.
LDA	198.	61.16	-307.8827	210.
PWGGA	144.	64.75	-309.5928	139.
BLYP	96.	68.09	-309.4749	110.
B3LYP	104.	66.07	-309.4083	123.
B3PW	149.	63.82	-309.5360	145.
Exp.[21]	125-141	-	-	-

Table 2.6: Equation of state data for $BaTiO_3$ using the 3rd-order Birch Murnaghan equation. Eleven points in the energy-volume curve were used and the range of volumes used around equilibrium was $\pm 10\%$ using basis set 2 (see section 2.2). The value of the bulk modulus, B_{EL} , as calculated from Eq. (2.5) is given in the last column for comparison.

	$B_{EOS}(\text{GPa})$	$V_o(\text{\AA}^3)$	$E_0(a.u.)$	$B_{EL}(\text{GPa})$
HF	202.	64.23	-307.4678	239.
LDA	238.	59.07	-307.7672	246.
PWGGA	221.	61.93	-309.4862	220.
BLYP	203.	64.09	-309.3636	201.
B3LYP	229.	62.77	-309.3082	220.
B3PW	230.	61.41	-309.4395	234.
Exp. [21]	125-141	-	-	

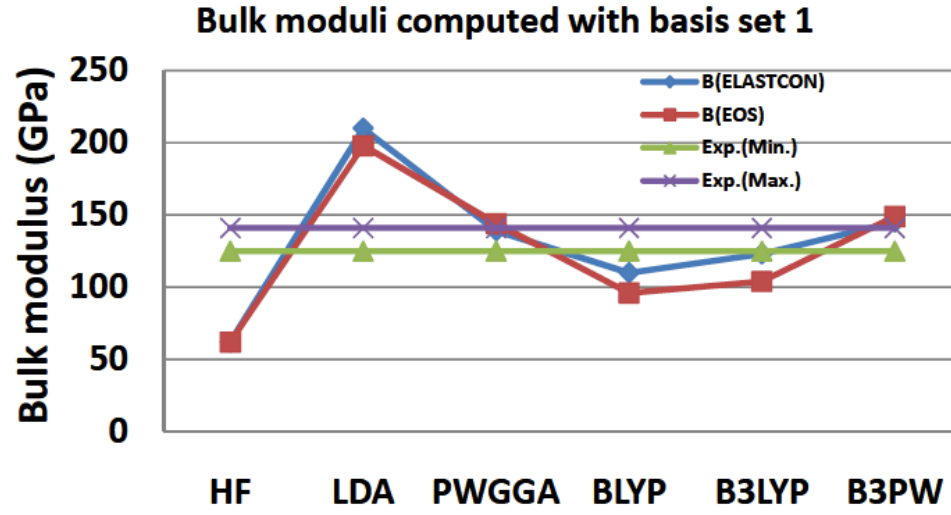


Figure 2.1: The computational values of bulk moduli are shown for basis set 1 computed with HF, DFT and hybrid functionals. The minimum and maximum experimental values of bulk moduli, titled as Exp.(Min.) and Exp.(Max.), are taken from ref. [21]. All values are in GPa.

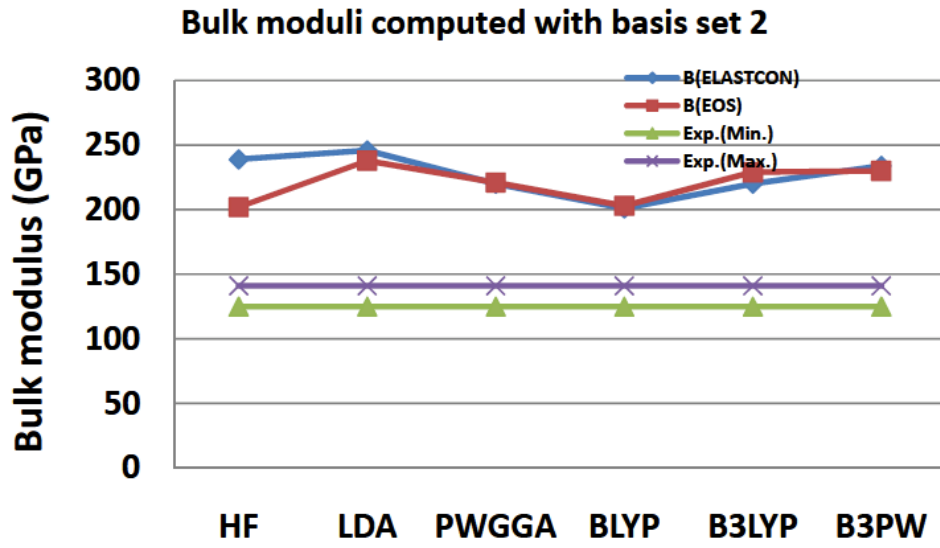


Figure 2.2: The computational values of bulk moduli are shown for basis set 2 computed with HF, DFT and hybrid functionals. The minimum and maximum experimental values of bulk moduli, titled as Exp.(Min.) and Exp.(Max.), are taken from ref. [21]. All values are in GPa.

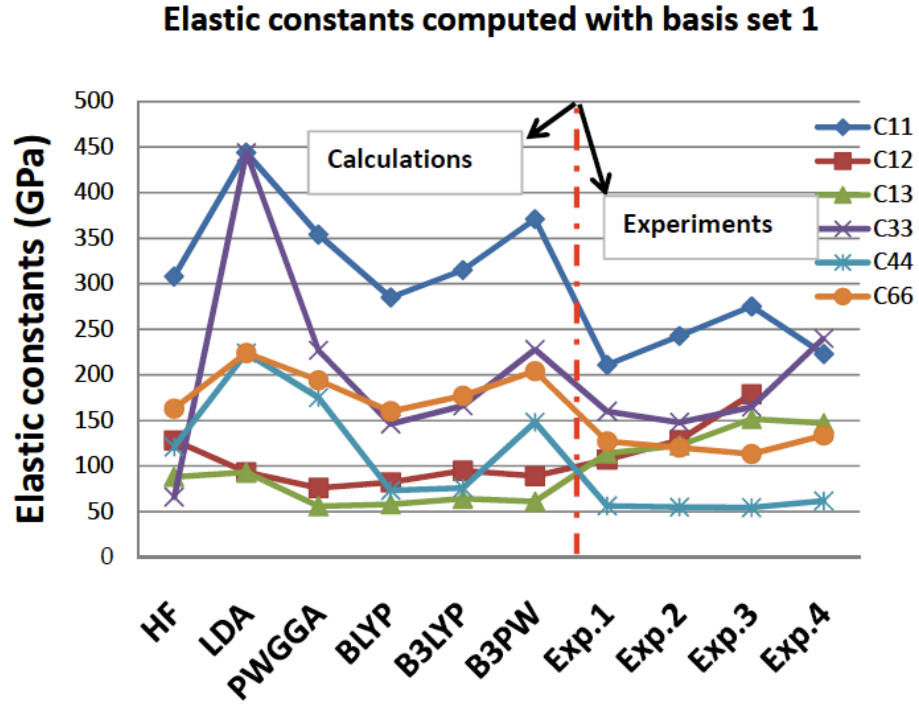


Figure 2.3: The computational and experimental values of elastic constants and bulk moduli are shown for basis set 1 computed with HF, DFT and hybrid exchange correlation potentials. The experimental values titled as Exp.1, Exp.2, Exp.3 and Exp.4 are taken from refs.[24, 25, 27, 26, 21]. All values are in GPa.

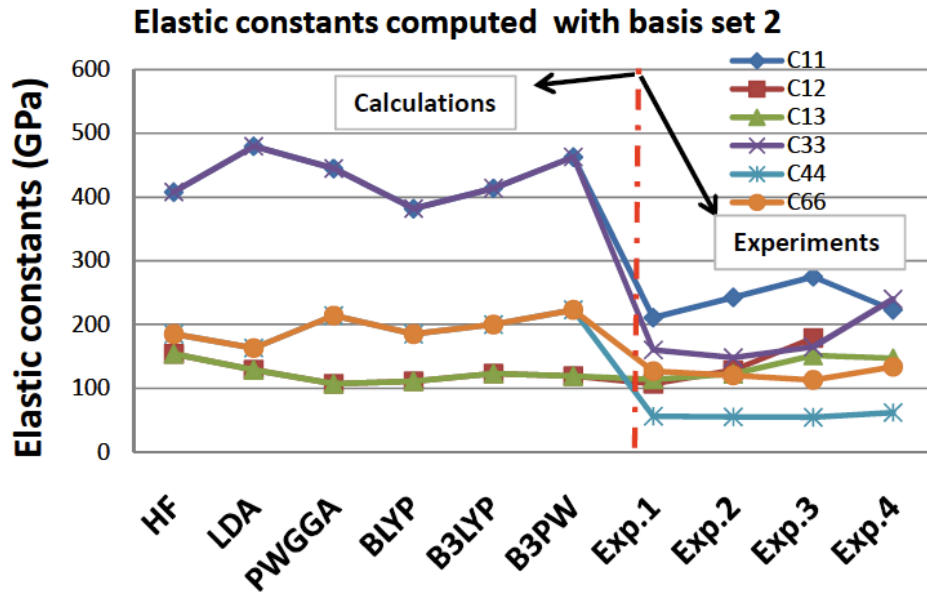


Figure 2.4: The computational and experimental values of elastic constants and bulk moduli are shown for basis set 2 computed with HF, DFT and hybrid exchange correlation potentials. The experimental values titled as Exp.1, Exp.2, Exp.3 and Exp.4 are taken from refs.[24, 25, 27, 26, 21]. All values are in GPa.

References

- [1] Philippe Ghosez. *First-principles study of the dielectric and dynamic properties of Barium Titanate*. Universite catholique De Louvain, Faculte des Sciences Appliques, 1997.
- [2] A. Bouhemadou and K. Haddadi. *Solid State Sciences*, pages 630–36, 2010.
- [3] J. D. Freire and R. S. Katiyar. *Phy. Rev. B*, pages 2074–85, 1988.
- [4] J. Kung, R. A. Angel, and N. L. Ross. *Phys. Chem. Minerals*, pages 35–43, 2001.
- [5] Nina Orlovskaya, Kjersti Kleveland, Tor Grande, and Mari Ann Einarsrud. *Jrnl. European Cera. Soc.*, pages 50–56, 1991.
- [6] T. Ishidate, S. Abe, H. Takahashi, and N. Mori. *Phy. Rev. Lett.*, pages 2397–2400, 1997.
- [7] E. V. Mejia-Uriarte, R. Y. Sato-Berru, M. Navarrete, M. Villagran-Muniz, C., Medina-Guerrez, C. Frausto-Reyes, and H. Murrieta. *Meas. Sci. Technol.*, pages 1319–23, 2006.

- [8] S. Piskunov, E. Heifets, R. I. Eglitis, and G. Borstel. Bulk properties and electronic structure of $SrTiO_3$, $BaTiO_3$, $PbTiO_3$ perovskites: An *ab initio* HF/DFT study. *Comput. Mater. Sci.*, pages 165–178, 2004.
- [9] R. Dovesi, V. R. Saunders, C. Roetti, R. Orlando, C. M. Zicovich-Wilson, F. Pascale, B. Civalleri, K. Doll, N. M. Harrison, I. J. Bush, Ph. D’Arco, and M. Llunell. *CRYSTAL2006 User’s Manual*. University of Torino, University of Torino, Torino, Italy, 2006.
- [10] Warren F. Perger, J. Criswell, B. Civalleri, and R. Dovesi. *ab-initio* calculation of elastic constants of crystalline systems with the CRYSTAL code. *Comput. Phy. Comm.*, pages 1753–1759, 2009.
- [11] Warren F. Perger. *Int. J. Quant. Chem.*, pages 1916–1922, 2010.
- [12] Mustafa Uludogan, Tahir Cagin, and William A. Goddard. MRS web archive.
- [13] H. Salehi, S. M. Hosseini, and N. Shahtahmasebi. *Chin. J. Phys.*, 42:619–27, 2004.
- [14] W. Marquardt. *SIAM J. Appl. Math.*, 11:431–44, 1963.
- [15] A. Khalal, D. Khatib, and B. Jannot. *Physica B*, pages 343–47, 1999.
- [16] F. D. Murnaghan. *Proc. Natl. Acad. Sci. (USA)*, 30(9):244–7, 1944.
- [17] C. Gatti, V. R. Saunders, and C. Roetttti. *J. Chem. Phys.*, pages 10686–96, 1994.

- [18] Abhay Shukla, E. D. Isaacs, D. R. Hamann, and P. M. Platzman. *Phy. Rev. B*, pages (052101)–1–4, 2001.
- [19] Furio Corà. *Molecular Physics*, pages 2483–2496, 2005.
- [20] Thomas Bredow, Karl Jug, and Robert A. Evarestov. *Phys. Stat. Sol.*, pages R10–R12, 2006.
- [21] Li Feng-Ying, Jin Chang-Qing, You Shu-Jie, Xiao Chang-Jiang, Yu Ri Cheng, Wang Xiao-Hui, Liu Jing, Li Xiao-Dong, Li Yan-Chun, and Chen Liang-Chen. *Chin. Phy. Lett.*, pages 1249–52, 2006.
- [22] Jerry Donohue, Stanley J. Miller, and Robert F. Cline. *Acta. Cryst.*, 11:693–695, 1958.
- [23] Upendra A. Joshi, Songhak Yoon, Sunggi Baik, and Jae Sung Lee. *J. Phys. Chem. B*, 110:12249–56, 2006.
- [24] Z. Li, S. K. Chan, M. H. Grimsditch, and E. S. Zouboulis. *J. Appl. Phys.*, pages 7327–32, 1991.
- [25] A. Schaefer, H. Schmitt, and A. Dorr. *Ferroelectrics*, pages 253–66, 1986.
- [26] T. Ishidate and S. Sasaki. *J. Phys. Soc. Jpn.*, pages 4214–17, 1987.
- [27] D. Berlincourt and H. Jaffe. *Phys. Rev.*, pages 353–266, 1958.
- [28] T. Ishidate and S. Sasaki. *Phys. Rev. Lett.*, pages 67–70, 1989.

- [29] A. C. Dent, C. R. Bowen, R. Stevens, M. G. Cain, and M. Stewart. *Eur. Ceram. Soc. J.*, 27:3739–43, 2007.
- [30] Wang Chun Mei, Duan Yi Feng, and Chen Chang Qing. *Chin. Phys. L.*, 26:(017203)–1–4, 2009.
- [31] Ravi S. Kumar, Andrew L. Cornelius, and Malcolm F. Nicol. *Phys. Stat. Sol.*, 244:290–294, 2006.
- [32] G. H. Kwei, A. C. Lawson, S. J. L. Billinge, and S. W. Cbeong. *J. Phys. Chem.*, 97:2368–77, 1993.
- [33] Robert Blinc. *Springer Berlin/Heidelberg*, 124:51–67, 2007.

Chapter 3

Electronic Structure and Properties of Rutile TiO_2

3.1 Introduction

Titanium dioxide (TiO_2) is an important transition metal oxide, which exists in anatase, rutile and brookite phases [1]. There is a considerable interest in the fabrication [2] of this material. It is employed extensively in optical devices, photovoltaic cells, gas sensors, and electrochemical storage devices [3]. The thin films of rutile TiO_2 have been widely tested due to their potential as materials suitable for solar cells, self-cleaning coatings and photocatalysis applications. Due to its technolog-

ical importance, the crystalline structure and properties of rutile TiO_2 phases has remained a major focus of researchers [1, 4, 5].

Ab-initio Hartree Fock (HF) and density functional theory (DFT) techniques are employed by various research groups to compute the optimized electronic structure, band gap and charge density of rutile TiO_2 [6, 7, 1, 8].

The *ab-initio* computation of the elastic constants and bulk moduli of rutile TiO_2 is presented in this work using the CRYSTAL09 code [9]. The availability of precise and accurate values of experimental lattice parameters, elastic properties [10] and chemical bonding [11] has provided a considerable challenge to *ab-initio* computational codes. Computational codes based upon the linear combination of atomic orbitals (LCAO) and plane waves (PW) were employed to compute the optimized crystalline structure of rutile TiO_2 [6, 7, 1, 8, 5]. However, the inadequacy of the existing potentials [1, 7, 6] to accurately predict the physics of TiO_2 has motivated a detailed analysis of a wide range of existing and new potentials [12, 6]. Research on the structural and electronic properties has confirmed the relative accuracy of the hybrid potentials [12, 6, 7, 1, 6].

There has been no systematic effort to explore the elastic properties of rutile TiO_2 using the LCAO code CRYSTAL09 [9]. CRYSTAL09 possesses a combination of geometry optimization techniques, basis sets, potentials and algorithms such as ELAST-CON [9] (for second-order elastic constants) and EOS (equation of state) [9]. The experimental values of lattice parameters, elastic constants and bulk moduli [10] of

the TiO_2 rutile phase provided an opportunity to confirm the relative merit of the self consistent field (SCF) process, the ELASTCON and EOS programs [13, 14].

3.2 Computational procedure

We employed two different basis sets and a variety of potentials to compute the optimized lattice constants and elastic properties (see section 3.3 for the discussion of potentials and basis sets). The ELASTCON [9] and EOS [9] algorithms are employed to compute the elastic constants and bulk moduli of rutile TiO_2 in an automated manner.

The two basis sets employed are named as basis set 1 and 2 (see section 3.3 for basis set definitions). Optimized lattice parameters are computed with HF, DFT and hybrid potentials using the two unique basis sets. The computations of elastic constants and bulk moduli are performed by employing the ELASTCON algorithm [9]. The computations of the equation of state and bulk moduli are carried out by the EOS algorithm. Finally, the bulk moduli obtained with ELASTCON and EOS algorithms are compared.

Optimized lattice parameters, elastic constants and bulk moduli, obtained with basis set 1 and 2, are also compared with the experimental values where possible.

A possible contribution of this research work is to assist a general reader in understanding the complex dependence of the elastic properties on the quality of basis sets, potentials, SCF process, ELASTCON and EOS parameters. Experimental values of lattice parameters, elastic constants and bulk moduli of rutile TiO_2 provide additional assistance for implementation of ELASTCON and EOS programs.

A significant number of computations and experiments are conducted on rutile TiO_2 . It is also noticed that a high precision has been achieved in the experimental lattice parameters of rutile TiO_2 [15]. The availability of the experimental values of lattice constants, elastic constants and bulk moduli of rutile TiO_2 , provides a highly valuable resource to conduct new research. In contrast, computations of elastic constants and bulk moduli have been done in an isolated and non-systematic manner.

A vast majority of *ab-initio* computations have already tried DFT exchange and correlation potentials [7, 16, 1]. The need for hybrid potentials arose because HF underestimated and DFT potentials overestimated the lattice parameters of rutile TiO_2 . It has been found that the higher exchange and correlation associated with the transition metals requires new hybrid potentials with variable exchange and correlation [7, 16, 1]. The HF, DFT as well as hybrid potentials are employed in this work [9] to fill the gap with regard to the efficient, accurate and systematic computation of elastic properties of rutile TiO_2 .

3.3 Potentials and basis sets

The HF, local and non-local DFT potentials have consistently resulted in inadequate results of the lattice parameters. First principles computations using PW codes [17, 18, 19, 20, 21, 22] can not employ the hybrid mixing of HF exchange and DFT correlations.

Therefore, we employed hybrid potentials in our computations of elastic properties as suggested in refs. [6, 1, 7, 16]. The hybridization between the *Ti* *d*-orbitals and *O* *p*-orbitals requires that an adequate percentage of exchange and correlation is introduced in the potential while computing the electronic structure of a material [23]. The DFT-PWGGA and DFT-PBE potentials lack the exchange part and HF lacks the correlation part barring them from being as accurate as hybrid potentials.

In addition to using hybrid potentials, the proper choice of basis sets, SCF tolerances, ELASTCON and EOS parameters can achieve the optimum efficiency as well as accuracy (see sections 3.4 and 3.6). Moreover, it is necessary to employ adequate SCF tolerances consistently.

We selected the O-8411d1[24] and O-6311d1 basis sets for *O* atoms and defined these basis sets as basis set 1 and 2, respectively. Both basis sets used a pseudopotential basis set for the *Ti* atom [9]. The aim of employing these combinations was to separate

the basis set dependency from other factors such as potentials, SCF parameters, ELASTCON and EOS tolerances.

The purpose of selecting basis set 1 and 2 is to understand the role of a basis set in combination with each individual potential. For basis set 1 and 2, the computations of lattice parameters, elastic constants and bulk moduli are performed with a specific purpose to assist a general reader.

The sensitivity of the elastic properties with respect to deviations in the lattice parameters [1] suggests that a detailed set of potentials must be employed to compute the lattice parameters and understand their influences on the elastic constant values. The impact of a particular potential and basis set on the computational values of lattice parameters, elastic constants and bulk moduli values can be understood by careful comparisons of results achieved for a variety of these basis sets and potentials.

Further, we have also performed comparisons of our computational results for each potential and basis set combination with the refs. [1, 16, 7] to confirm their research findings.

3.4 Experiments

Due to its technological importance, a significant number of experiments have been conducted on rutile TiO_2 [25, 22, 10]. The experimental results of the electronic structure, band gap, optic and elastic properties are available for rutile TiO_2 . The lattice parameters of the rutile TiO_2 have been determined [15] precisely up to the fifth significant figure. In addition, the pressure and temperature dependence of elastic constants and bulk moduli have also been explored through experimental means.

The experimental and computational values of elastic constants and bulk moduli [10] of rutile TiO_2 have special significance as they serve the purpose of linking these vital branches of research. The importance of achieving a consistency in the lattice parameters of rutile TiO_2 among diverse experimental techniques and computational codes is a remarkable achievement which has been repeatedly observed [6, 7, 1, 16].

However, there are deviations in the experimental values of elastic constants and bulk moduli due to their dependence on the experimental details, pressure and temperature conditions [26]. Therefore, the sources that cause the variations in the experimental values [27, 26, 10, 28] must also be considered. However, the dependence of the experimental results on the nature of the experimental set up and ambient conditions can be explored and understood by robust and reliable *ab-initio* computational methods.

Fortunately, a detailed research is carried out by ref. [29] on variations in experimental and computational values of elastic constants and bulk moduli of rutile TiO_2 . The elastic properties vary with changes in temperature and pressure conditions.

An increase in pressure has shown an increase in the elastic constants and bulk moduli values [29] for rutile TiO_2 . Moreover, the values of $C_{11}, C_{33}, C_{66}, C_{12}$ and C_{13} increase with increasing pressure whereas the pressure dependence of C_{44} is not clear. Moreover, the elastic constants are nonlinearly dependent on the temperature. Our *ab-initio* computational values of elastic constants and bulk moduli are relatively independent of pressure variations to provide a reliable and independent set of values.

Another important area where the experiments are performed is the volume charge density and chemical bonding of rutile TiO_2 [11]. The quantitative convergent beam electron diffraction (QCBED) technique was employed to determine the experimental volume charge density and chemical bonding. The experimental data was utilized to confirm the contribution of ionic and covalent bonding in rutile TiO_2 . The experimental charge density maps predicted the the $p - d$ hybridization between Ti 3- d electrons and O ligands.

The charge density influenced by highly localized d -orbitals of Ti atoms influences the selection of proper basis sets and potentials in *ab-initio* computations (see section on the potential, basis sets 3.3 and discussion of results 3.6).

Unlike the precision in the experimental lattice parameters, the computational values of lattice parameters vary in the second significant figures. The variation in the lattice parameter values is partially due to the complex nature of the chemical bonding of rutile TiO_2 . Moreover, the sensitivity of the computational values of lattice parameters is attributed to the choice of potentials and basis sets. However, the hybrid potentials can map the chemical bonding and charge density of rutile TiO_2 with a considerable accuracy.

In general, the *ab-initio* computations are lacking the level of accuracy of the experiments. However, the extensive computational effort by refs. [7, 16, 1, 6, 30] has provided guidance for the present study.

3.5 Computational parameters

For the computation of lattice parameters and elastic properties, the SCF tolerances and other computational parameters were carefully chosen. The ELASTCON, EOS and SCF tolerances were adjusted due to the highly localized nature of transition metal Ti d -orbitals. The ELASTCON and other parameters were adjusted as $STEPSIZE=0.01$, $NUMDERIV=7$, $LGRID=(75, 434)$ and $SHRINK=9 \times 9$. The SCF tolerances were fixed as $TOLINTEG=9\ 9\ 9\ 18$ and $TOLDEE=9$ [22].

3.6 Discussion of results

Tables 3.1 and 3.2 show the optimized lattice parameters computed with basis sets 1 and 2, respectively. Considerable agreement between the computational and experimental values of lattice parameters computed with DFT-PWGGA, DFT-PBE, DFT-B3LYP and DFT-B3PW potentials can be seen in Table 3.1. The experimental values from refs. [2, 10, 4] are provided at the bottom of Table 3.1. The optimized lattice parameters show less agreement with the experimental values in case of basis set 2 as shown in Table 3.2.

Elastic constants and bulk moduli computed with ELASTCON are presented in Tables 3.3, 3.4 and Figures 3.1, 3.2. For basis set 1, the agreement between the computational and experimental values of elastic constants is better with non-local DFT and hybrid potentials only. The disagreement between the computational and experimental values of elastic constants is significantly higher for basis 2 as shown in Table 3.4. The values of elastic constants and bulk moduli are higher than the experimental values as the O-6311d1 basis set fails to represent the chemical bonding required for rutile TiO_2 .

Tables 3.5 and 3.6 show the comparisons between the bulk moduli values computed with ELASTCON and EOS algorithms. Excellent agreement is observed between the computational values of bulk moduli achieved with ELASTCON and EOS programs

(see Figure 3.2). The agreement between the bulk moduli values points at the computational accuracy of the ELASTCON and EOS programs. Moreover, it is important that a good agreement in computational results should also be crosschecked with the experimental values of the bulk moduli given at the bottom of Tables 3.5 and 3.6. Table 3.5 shows a better agreement between the computational and experimental values [4, 22, 1, 5].

However, there is a considerable disagreement between the computational and experimental values of C_{11} , C_{12} , C_{13} , C_{33} , C_{44} , C_{66} and B for basis set 1 and 2 with HF and DFT-LDA potentials as shown in Tables 3.3 and 3.4. On the other hand, the computational values of C_{11} , C_{12} , C_{13} , C_{33} , C_{44} , C_{66} and B provide a significant agreement with the experimental values computed with DFT-PWGGA, DFT-PBE and hybrid potentials for basis set 1 as shown in Table 3.3 and Figure 3.1.

In addition, slightly better agreement between the computational and experimental values of lattice parameters, elastic constants and bulk moduli is observed for the hybrid potentials. The hybrid potentials have shown better agreement due to the adequate percentage of exchange and correlation contributions to total energy of the crystal specifically important for the highly correlated physics of the *Ti* transition metal. The localized nature of the *Ti* atom *d*-orbitals contributes to the higher exchange and correlation effects.

The HF, local DFT and non-local DFT potentials can not predict results as effectively

as hybrid potentials. Moreover, the computational values of lattice parameters, elastic constants and bulk moduli deviate from the corresponding experimental values for HF and DFT-LDA potentials [6]. It can be easily seen in Tables 3.1-3.6. In fact, the lack of correlation in HF and the localized nature of DFT-LDA potentials make these potentials less effective for transition metal oxides which possess the covalent as well as ionic nature of chemical bonding.

It must be mentioned that DFT-PWGGA and DFT-PBE exhibit better agreement with experimental results due to the non-localized nature of the rutile TiO_2 volume charge density. However, the agreement between the DFT-PWGGA, DFT-PBE and experimental results of elastic constants may not be adequate which can be confirmed by values in Tables 3.2, 3.4 and 3.6.

3.7 Conclusions

The technological applications of titanium dioxide (TiO_2) have generated a significant research activity in experimental and computational sciences. Computational research has resulted in testing the merit of basis sets, potentials and new programs. The elastic properties of rutile TiO_2 are computed and compared with experimental values. The dependance of experimental values on experimental set up, temperature and pressure conditions can not be ignored. The computations of elastic constants

and bulk moduli by a wide variety of *ab-initio* techniques provide results to generate new experiments on this material.

We have separated the factors that determine the quality of computational results of the lattice parameters and elastic properties. The non-local DFT and hybrid potentials present better agreement with the experimental values of lattice parameters, elastic constants and bulk moduli. However, the disagreement between the computational and experimental values of the elastic constants and bulk moduli for HF and DFT-LDA potentials [17, 18, 20] is significant.

The computations presented for rutile TiO_2 with different potentials are motivated by a variety of challenges related with the existing potentials. For a crystalline system such as rutile TiO_2 , which has considerable visibility in the experimental research arena, an integrated set of computational results have significant utility. These computations can guide researchers to appreciate the subtle influences of the charge density on lattice parameters and elastic properties of rutile TiO_2 .

Table 3.1: The values of relaxed lattice constants (in $\overset{\circ}{\text{\AA}}$) and ambient volume (in $\overset{\circ}{\text{\AA}}^3$) and total energy, E (in a.u.), for rutile TiO_2 . The computations were done by using Hartree-Fock, DFT LDA, PWGGA, BLYP, PBE0, B3LYP and B3PW potentials using basis set 1. (see sections 3.2, 3.3, 3.4 and 3.6 .)

	$a(\overset{\circ}{\text{\AA}})$	$c(\overset{\circ}{\text{\AA}})$	$Vol(\overset{\circ}{\text{\AA}}^3)$	$Density(g/cm^3)$	$E(a.u.)$
HF	4.568	2.980	62.11	4.264	-415.125024
LDA	4.559	2.932	60.98	4.351	-415.4375020
PWGGA	4.640	2.976	64.08	4.140	-417.745101
PBE	4.647	2.978	64.32	4.125	-417.450436
BLYP	4.66	3.01	65.67	4.040	-417.646742
B3LYP	4.629	2.976	63.78	4.160	-417.525784
B3PW	4.599	2.961	62.63	4.236	-417.647585
PBE0	4.627	2.973	63.69	4.627	-417.800715
Exp.[2, 10, 4]	4.59	2.96	62.36	-	-

Table 3.2: The values of relaxed lattice constants (in $\overset{\circ}{\text{\AA}}$) and ambient volume (in $(\overset{\circ}{\text{\AA}})^3$) and total energy, E (in a.u.), for rutile TiO_2 . The computations were done by using Hartree-Fock, DFT LDA, PWGGA, BLYP, PBE0, B3LYP and B3PW potentials using basis set 2. (see sections 3.2, 3.3, 3.4 and 3.6 .)

	$a(\overset{\circ}{\text{\AA}})$	$c(\overset{\circ}{\text{\AA}})$	$Vol(\overset{\circ}{\text{\AA}}^3)$	$Density(g/cm^3)$	$E(a.u.)$
HF	4.561	2.991	62.24	4.262	-415.030280
LDA	4.539	2.904	59.84	4.433	-415.303870
PWGGA	4.619	2.946	62.82	4.220	-417.622557
PBE	4.625	2.949	63.05	4.204	-417.329627
BLYP	4.657	2.971	64.41	4.117	-417.520930
PBE0	4.571	2.940	61.46	4.317	-417.245299
B3LYP	4.607	2.957	62.75	4.225	-417.408695
B3PW	4.583	2.942	61.81	4.292	-417.533064
Exp.[31]	4.593	2.958	62.40	-	-
Exp. [2, 10]	4.59	2.96	62.36	-	-

Table 3.3: The elastic constants and bulk modulus computational results using the Hartree Fock and DFT LDA, PWGGA, BLYP, PBE0, B3LYP and B3PW potentials with basis set 1. All values are in GPa. (see sections 3.2, 3.3, 3.4 and 3.6.)

	C_{11}	C_{12}	C_{13}	C_{33}	C_{44}	C_{66}	B
HF	363.88	216.43	184.34	625.97	164.08	276.93	269.71
LDA	311.10	210.59	175.15	504.48	159.31	252.60	243.15
PWGGA	266.41	177.25	148.88	462.40	138.23	223.33	208.06
PBE	261.66	176.04	146.29	457.73	135.14	221.06	205.14
BLYP	255.76	133.27	142.78	477.90	153.90	206.05	187.60
PBE0	277.37	184.91	155.40	494.27	139.18	234.10	217.12
B3LYP	281.36	186.22	156.70	505.70	140.29	236.43	219.85
B3PW	293.89	193.64	164.11	517.48	146.55	245.56	229.13
Exp.[10]	268.00	175.00	147.00	484.00	124.00	190.00	212.00,230.00

Table 3.4: The elastic constants and bulk modulus computational results using the Hartree Fock and DFT LDA, PWGGA, BLYP, PBE0, B3LYP and B3PW potentials with basis set 2. All values are in GPa. (see sections 3.2, 3.3, 3.4 and 3.6.)

	C_{11}	C_{12}	C_{13}	C_{33}	C_{44}	C_{66}	B
HF	393.38	237.08	209.69	662.10	170.85	302.60	295.27
LDA	170.95	384.96	204.67	577.12	130.39	278.53	265.91
PWGGA	222.60	273.01	182.34	522.34	123.35	246.21	237.24
PBE	220.46	269.67	180.65	517.01	122.22	243.67	234.72
BLYP	259.83	225.99	174.58	508.73	123.33	235.50	231.32
PBE0	267.06	281.97	203.06	578.72	138.82	273.17	262.62
B3LYP	295.27	239.63	192.98	562.44	137.12	261.30	254.96
B3PW	268.97	269.36	197.01	568.79	136.54	267.48	257.44
Exp.[10]	268.00	175.00	147.00	484.00	124.00	190.00	212.00,230.00

Table 3.5: Equation of state results for tetragonal TiO_2 with the Birch Murnaghan 3rd order equation. The energy-volume curve was fitted with eleven points and the range of volume around equilibrium was chosen as $\pm 10\%$ using basis set 1. (see sections 3.2, 3.3, 3.4 and 3.6.) The value of the bulk modulus, B_{EL} , calculated separately, is given in the last column for comparison.

	$B_{EOS}(\text{GPa})$	$V_o(\text{\AA}^3)$	$E_0(a.u.)$	$B_{EL}(\text{GPa})$
HF	266.65	62.29	-415.125014	269.71
LDA	241.02	60.98	-415.4374458	243.15
PWGGA	205.84	64.09	-417.745066	208.06
PBE	202.42	64.33	-417.450408	205.14
BLYP	190.81	65.93	-417.646784	187.60
PBE0	232.36	62.24	-417.3564061	217.12
B3LYP	216.58	63.81	-417.525805	219.85
B3PW	226.04	62.66	-417.647557	229.13
Exp.[10]	-	-	-	212.00,230.00

Table 3.6: Equation of state results for rutile TiO_2 with the Birch Murnaghan 3rd order equation. The energy-volume curve was fitted with eleven points and the range of volume around equilibrium was chosen as $\pm 10\%$ using basis set 2. (see sections 3.2, 3.3, 3.4 and 3.6.) The value of the bulk modulus, B_{EL} , calculated separately, is given in the last column for comparison.

	$B_{EOS}(\text{GPa})$	$V_o(\text{\AA}^3)$	$E_0(a.u.)$	$B_{EL}(\text{GPa})$
HF	292.73	62.31	-415.030267	295.27
LDA	278.99	59.84	-415.303858	282.68
PWGGA	238.71	62.87	-417.622543	237.24
PBE	235.96	63.10	-417.329611	234.72
BLYP	229.03	64.45	-417.520911	231.32
PBE0	262.66	61.49	-417.2452817	262.62
B3LYP	252.43	62.81	-417.408677	254.96
B3PW	256.16	61.83	-417.533045	257.44
Exp.[10]	-	-	-	212.00,230.00

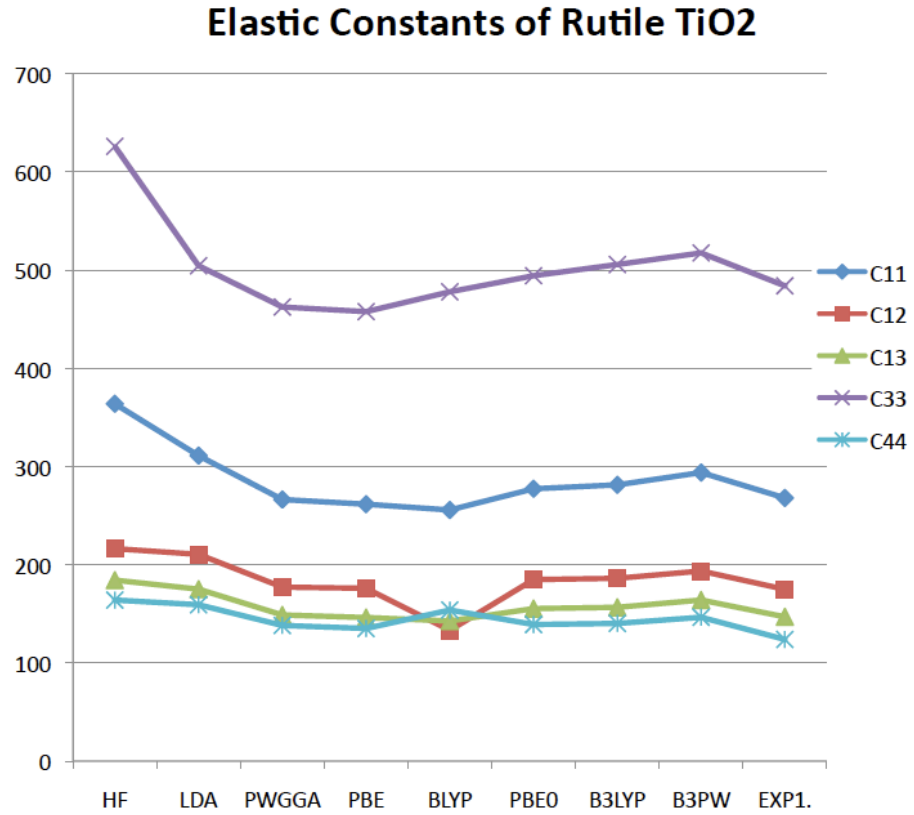


Figure 3.1: The computational and experimental values of elastic constants and bulk moduli are shown. All values are in GPa.

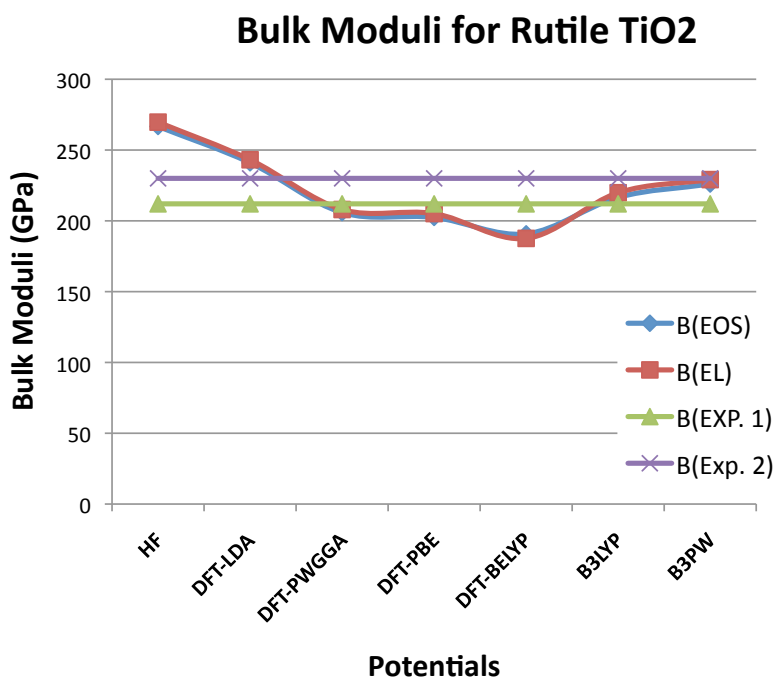


Figure 3.2: The computational and experimental values of bulk moduli are shown. All values are in GPa.

References

- [1] Frederic Labat, Philippe Baranek, Christophe Domain, Christian Minot, and Carlo Adamo. *The Journal of Chemical Physics*, 126:(154703)1–12, 2007.
- [2] Sakae Tanemuraa, Lei Miaoa, Wilfried Wunderlicha, Masaki Tanemuraa, Yukimasa Morib, Shoichi Tohc, and Kenji Kanekoc. *Science and Technology of Advanced Materials*, 6:11–17, 2005.
- [3] Mo Shang-Di and Ching W. Y. *Phys. Rev. B*, page 13023, 1995.
- [4] Hongzhi Yao, Lizhi Ouyang, and WaiYim Ching. *J. Am. Ceram. Soc.*, pages 3194–3204, 2007.
- [5] Bilc D. I., Orlando R., Shaltaf R., Rignanese G.-M., Jorge Íñiguez, and Ghosez Ph. *Phys. Rev. B*, 77:165107, 2008.
- [6] Furio Corà. *Molecular Physics*, pages 2483–2496, 2005.
- [7] Carlo Adamo and Vincenzo Barone. *J Chem Phys*, 110:6158–6170, 1999.
- [8] M. E. Stizzaumainis, T. Ejima, and W. J. James. *Acta Cryst.*, 8:493–97, 1961.

- [9] R. Dovesi, V. R. Saunders, C. Roetti, R. Orlando, C. M. Zicovich-Wilson, F. Pascale, B. Civalleri, K. Doll, N. M. Harrison, I. J. Bush, Ph. D’Arco, and M. Llunell. *CRYSTAL2006 User’s Manual*. University of Torino, University of Torino, Torino, Italy, 2006.
- [10] M. Iuga, G. Steinle-Neumann, and J. Meinhardt. *Eur. Phys. J. B*, 58:127–133, 2007.
- [11] Jiang B., Zuo J. M., Jiang N., O’Keeffe M., and Spence J. C. H. *Acta Cryst.*, page 341, 2003.
- [12] Corá Furio, Alfredsson Maria, Mallia Giuseppe, Middlemiss Derek S., Mackrodt William C., Dovesi Roberto, and Orlando Roberto. *Principles and Applications of Density Functional Theory in Inorganic Chemistry II*, page 171, 2004.
- [13] Warren F. Perger, J. Criswell, B. Civalleri, and R. Dovesi. *ab-initio* calculation of elastic constants of crystalline systems with the CRYSTAL code. *Comput. Phy. Comm.*, pages 1753–1759, 2009.
- [14] Warren F. Perger. *Int. J. Quant. Chem.*, pages 1916–1922, 2010.
- [15] B. H. O’Connor and S. Pratapa. *Advances in X-ray Analysis*, 45:158–165, 2002.
- [16] Frederic Labat, Philippe Baranek, and Carlo Adamo. *J. Chem. Theory Comput.*, 4:341–352, 2008.

- [17] Masayoshi Mikami, Shinichiro Nakamura, Osamu Kitao, Hironori Arakawa, and Xavier Gonze. *Jpn. J. Appl. Phys.*, 39:L847–L850, 2000.
- [18] X. Ma, P. Liang, L. Miao, S. Bie, C. Zhang, L. Xu, J. Jiang, H. Yao, L. Ouyang, and W. Ching. *Phys. Status Solidi B*, pages 2132–2139, 2009.
- [19] Yong Liu, Lihong Ni, Zhaohui Ren, Gang Xu, Chenlu Song, and Gaorong Han. *J. Phys. Condens. Matter*, 21:275901–6, 2009.
- [20] Nicholas M. Harrison Joseph Muscat Varghese Swamy. *Phys. Rev. B*, page 224112, 2010.
- [21] E. Shojaee and M. R. Mohammadizadeh. *J. Phys. Condens. Matter*, 22:1–8, 2010.
- [22] Zhao JianZhiwang GuangTao Liang Yong-Cheng. *Chin. Phys. Lett.*, 25:4356–59, 2008.
- [23] Gervais Francois and Kress Winfried. *Phys. Rev. B*, 31:4809–4814, 1985.
- [24] Thomas Bredow, Karl Jug, and Robert A. Evarestov. *Phys. Stat. Sol.*, pages R10–R12, 2006.
- [25] I. J. Fritz. *Journal of Physics and Chemistry of Solids*, 35:817–826, 1974.
- [26] Hearmon R. F. S. *Rev. Mod. Phys.*, 18:409–440, 1946.
- [27] L. Gerward and J. Staun Olsen. *J. Appl. Cryst.*, 30:259–264, 1997.

- [28] L. Kóci, D. Y. Kim, J. S. De Almeida, M. Mattesini E. Isaev, and R. Ahuja. *J. Phys. Condens. Matter*, page 345218, 2008.
- [29] Zhu Jun, Yu JingXin, Wang YanJu, Chen XiangRong, and Jing FuQian. *Chin. Phys. Soc.*, 17:2216–21, 2008.
- [30] Held K., Anisimov V., V. Eyert, Keller G., McMahan A., Nekrasov I., and Vollhardt D. Lda+dmft investigations of transition metal oxides and f-electron materials. In *Advances in Solid State Physics*, volume 43 of *Advances in Solid State Physics*, pages 267–286. Springer Berlin / Heidelberg, 2003.
- [31] J. K. Burdett, T. Hughbanks, G. J. Miller, J. W. Richardson, and J. V. Smith. *J. Am. Chem. Soc.*, 109, 1987.

Chapter 4

Optimized Lattice Parameters and Elastic Properties of $BaFeO_3$

4.1 Introduction

Transition metal oxides exhibit interesting properties such as high-temperature superconductivity, colossal magnetoresistance and ferroelectricity. The exceptional properties of these materials have enhanced research interests in newly found ferroic properties. The ABO_3 (where $A = Ba, Sr, Ca$, $B = Co, Fe, Mn$ and $O = Oxygen$) perovskites can be employed as spintronic sensors, solid oxide fuel cells (SOFC), oxygen separation membranes and catalysts [1]. These materials undergo pressure-induced

phase transitions. The knowledge about the elastic properties of perovskites is vital for their implementation as novel sensors and actuators. A detailed research on the crystalline structure and elastic properties of cubic and tetragonal $BaFeO_3$ have not been attempted.

Researchers [2] have widely employed *ab-initio* simulations, fabrication and characterization techniques to explore these materials. The hexagonal, triclinic and rhombohedral phases are successfully found by researchers [3, 4, 5, 6, 7, 8]. The X-ray diffraction techniques have been employed to determine the crystalline structure of thin films of $BaFeO_3$ [9]. The pseudocubic and tetragonal crystalline structures have been found in thin films of $BaFeO_3$. Ferroic properties are found in crystalline structures of $BiFeO_3$ and $BaFeO_3$ [10, 9] by experimental and computational methods.

Advancement in the computational speed has resulted in efficient DFT and hybrid potentials and basis sets. The crystalline geometry optimization techniques have contributed to the success in the exploration of the novel crystalline structure and properties of these materials. We employed *ab-initio* computational methods to determine the electronic structure, elastic constants and bulk moduli of $BaFeO_3$. However, a the detailed exploration of lattice parameters, elastic constants and bulk moduli of $BaFeO_3$ has not been done by first-principles computational techniques. CRYSTAL09 code possesses geometry optimization techniques which can be utilized to

compute the crystalline structure and elastic properties of high-pressure phases of complex crystals.

The *ab-initio* computational techniques are employed to compute the elastic properties of cubic and tetragonal perovskite $BaFeO_3$ for a wide variety of basis sets and potentials.

Moreover, the *ab-initio* computational techniques are employed to compute the lattice parameters of cubic and tetragonal $BaFeO_3$. The geometry optimization techniques available in CRYSTAL09 code are utilized for computing the cubic and tetragonal structures with HF, local, non-local DFT and hybrid potentials.

Advancement of computational speed and processing power has led to a thrust in the computational effort on perovskites [11, 12, 13, 14, 7, 6, 2]. The novel phases of the novel class of perovskites are being discovered and experimented. CRYSTAL09 employs the first principles computational techniques to determine the electronic structure and properties of a wide variety of materials.

CRYSTAL09 code has unique crystalline geometry optimization algorithms which can be utilized for the innovative research into the novel phase discoveries. We employed BILLY script in CRYSTAL09 code to determine the crystalline structure of cubic $BaFeO_3$. We employed all necessary checks to separate the numerical noise and physics.

We employed ELASTCON and EOS algorithms for the computation of elastic constants and bulk moduli of cubic and tetragonal $BaFeO_3$.

4.2 Procedures

The high-pressure cubic and tetragonal phases of $BaFeO_3$ were computed by employing BILLY program in combination with CRYSTAL code.

Later, CRYSTAL09 code was employed to compute the elastic constants and bulk moduli of cubic and tetragonal $BaFeO_3$ phases. The computational parameters were kept consistent throughout these computations. Shrinking factor was adjusted to 16 32, tolerances on SCF were kept as 9 9 9 9 18 and the tolerances on energy gradient were also set to 9.

The bulk moduli are computed by employing the ELASTCON (second-order elastic constants) and EOS (equation of state).

4.2.1 Potentials and basis sets

The basis sets and potentials were chosen from CRYSTAL09 basis set library [15]. The basis sets are defined as basis set 1 and 2. The basis set 1 consist of Fe-86-

411d41G-towler-1992a and O-8-411d1-bredow-2006 while basis set 2 consists of Fe-86-411d41G-towler-1992b and O-8-411d1-cora-2005. The basis set for *Ba* atom is kept as ECP. Moreover, the basis sets for *Ba* and *O* atoms are already employed on tetragonal *BaTiO₃* and rutile *TiO₂*.

4.2.2 Billy script

Billy script [15] is employed within CRYSTAL09 code to compute the optimized crystalline structure of *BaFeO₃*. There are various options available within BILLY program.

The optimized crystalline structure is determined in BILLY program by employing the small variation in the lattice parameter value for a range from .0001 to 5 percent of a lattice parameter value. The values of the energy within a given range of the lattice parameter values are curve-fitted by a polynomial of third degree. The optimized lattice parameter is then computed at the lowest energy by the nonlinear least square curve-fitting of the energy values obtained.

Accuracy of BILLY program was crosschecked by employing the non-linear least square curve fitting using MATHEMATICA. The values of optimized lattice parameters computed with BILLY script and MATHEMATICA showed a significant agreement in the optimized values of lattice parameters.

4.2.3 Computational tolerances

The accuracy of the computations can be enhanced by employing the tighter tolerances for the energy and its gradient. The SCF convergence was achieved by employing the BROYDEN SCF technique. The numerical values of various parameters in BROYDEN were adjusted adequately [15].

4.3 Computational results

Tables 4.1 - 4.3 show computational results of optimized lattice parameters, volume, density, total energy, elastic constants and bulk moduli of cubic $BaFeO_3$ with basis set 1 (see section 4.2.1 for basis set definitions). The HF, local, non-local DFT and hybrid potentials were employed. The values of lattice parameters from refs. [16, 17] are shown in Tables 4.1 and 4.4.

Tables 4.4 - 4.6 show computational results of optimized lattice parameters, volume, density, total energy, elastic constants and bulk moduli of cubic $BaFeO_3$ computed with basis set 2 (see section 4.2.1 for basis set definitions). The HF, local, non-local DFT and hybrid potentials were employed.

Tables 4.2 and 4.6 contain computational values of elastic constants. Computational

results obtained with DFT-LDA, DFT-PWGGA and DFT-PBE potentials for basis set 1 and 2 are shown in these Tables.

Tables 4.7- 4.10 present the computational results of the optimized lattice parameters, volume, density, total energy, elastic constants and bulk moduli of tetragonal $BaFeO_3$ computed with basis set 1 and 2 (see section 4.2.1 for basis set definitions). The HF, local, non-local DFT and hybrid potentials were employed. The optimized lattice parameters show a significant agreement with the experimental values reported by ref. [18].

However, we did not compare our results with the experimental lattice parameters of the thin film tetragonal structures of $BaFeO_3$ as done earlier by refs. [9, 19]. This is due to the fact that the lattice parameters of thin films structures are fairly large than the bulk crystalline structures.

4.4 Analysis

Computational values of lattice parameters , volume, density and total energy are computed with basis set 1 and 2 (see section 4.2.1 for basis set definitions). These computations were performed for cubic and tetragonal $BaFeO_3$. The HF, local DFT, non-local DFT and hybrid potentials were employed as shown in Tables 4.1 and 4.10.

A considerable agreement can be observed between our values of optimized lattice parameters and the theoretical values by refs. [16, 17]. The computational values of lattice parameters obtained with HF, DFT and hybrid potentials agree with each other as shown in Tables 4.1 and 4.4.

Values of elastic constants and bulk moduli, computed with ELASTCON and EOS algorithms, are presented in Tables 4.2, 4.3, 4.5 and 4.6. A significant agreement can be observed in values of bulk moduli computed from elastic constants and equation of state employing ELASTCON and EOS programs respectively (see Figure 4.1). The computational value of elastic constants and bulk moduli from ref. [20] are also presented in 4.2, 4.3, 4.5 and 4.6. They employed LSDA potentials using plane-wave (PW) code for computing elastic constants and bulk moduli.

Tables 4.7 and 4.8 show lattice parameters, volume, density and energy computed with basis set 1 and 2 (see section 4.2.1 for basis set definitions). The values of a , c and c/a depict a novel ferroelectric property accompanied with non- d^0 displacement in $BaFeO_3$ resulting in a large difference between a and c . Tetragonal $BaFeO_3$ is unlike the tetragonal $BaTiO_3$ showing a large difference between the lattice parameters a and c .

Higher percentage of ionic bonding between the Fe and O atoms may have resulted in significant exchange and correlation effects. High value of c/a point at the large anisotropy in tetragonal $BaFeO_3$ due to Fe atom.

Values of bulk moduli computed with EOS algorithm are shown in Tables 4.8 and 4.10. Elastic constants and bulk moduli values are significantly lower than their corresponding values of cubic $BaFeO_3$ as shown in Tables 4.2, 4.3, 4.5 and 4.6.

4.5 Concluding Remarks

Computations of lattice parameters, elastic constants and bulk moduli of cubic and tetragonal $BaFeO_3$ were carried out with HF, local DFT, non-local DFT and hybrid potentials. Two different basis sets were chosen. Computational values of lattice parameters of cubic phase were compared with the values from ref. [20]. A significant agreement in values of lattice parameters was observed. Moreover, the values of elastic constants and bulk moduli were compared with the computational values. A considerable disagreement was observed while comparing our values of elastic constants and bulk moduli with values from ref [20].

For tetragonal phase, the values of lattice parameters, elastic constants and bulk moduli were computed. Comparisons were made with the experimental values of lattice parameters [18] and a significant agreement was again observed.

Table 4.1: The values of relaxed lattice constants (in \AA), ambient volume (in $(\text{\AA}^0)^3$), density (in gm/cm^3), and energy (in a.u.) for cubic BaFeO_3 . The computations were done by using Hartree-Fock, DFT LDA, PWGGA, PBE and B3LYP potentials employing basis set 1. (see sections 4.2, 4.4 and 4.5.)

	$a(\text{\AA})$	$V_o((\text{\AA}^0)^3)$	$Density(\text{g/cm}^3)$	$E(\text{a.u.})$
HF	3.956	61.91	6.486	-1511.67809
LDA	3.819	55.73	7.204	-1510.95477
PWGGA	3.916	60.07	6.684	-1515.00777
PBE	3.921	60.29	6.660	-1514.483489
B3LYP	3.921	60.29	6.656	-1514.619036
Exp. ^a	3.994	-	-	-
Th. ^a	3.975	-	-	-
Th. ^a	4.116	-	-	-

a. Refs. [16, 17, 21]

Table 4.2: The elastic constants and bulk modulus computational results using the Hartree Fock and LDA, PWGGA and PBE potentials with basis set 1. (see sections 4.2, 4.4 and 4.5.) All values are in GPa.

	C_{11}	C_{12}	C_{44}	B
LDA	194.28	225.78	131.71	215.28
PWGGA	107.77	155.23	88.37	139.41
PBE	108.05	150.96	89.50	136.65
LSDA ^a	238.54	164.33	105.35	205.18

a. Ref. [20]

Table 4.3: Equation of state results for cubic $BaFeO_3$ with the Birch Murnaghan 3rd order equation. The energy-volume curve was fitted with eleven points and the range of volume around equilibrium was chosen as $\pm 10\%$ employing basis set 1 (see sections 4.2, 4.4 and 4.5. The value of the bulk modulus, B_{EL} is given in the last column for comparison.)

	$B_{EOS}(\text{GPa})$	$V_o(\text{\AA}^3)$	$E_0(a.u.)$	$B_{EL}(\text{GPa})$
HF	129.70	61.94	-1511.6746041	-
LDA	212.85	55.73	-1510.954822	215.28
PWGGA	142.16	60.04	-1515.007794	139.41
PBE	149.87	60.27	-1514.483511	136.65
B3LYP	146.31	60.35	-1514.6190517	142.65
LSDA ^a	189.06	-	-	-
<hr/> <i>a.</i> Ref. [20] <hr/>				

Table 4.4: The values of relaxed lattice constants (in \AA), ambient volume (in $(\text{\AA}^0)^3$), density (in gm/cm^3), and energy (in a.u.) for cubic $BaFeO_3$. The computations were done by using Hartree-Fock, DFT LDA, PWGGA, PBE and B3LYP potentials employing basis set 2. (see sections 4.2, 4.4 and 4.5.)

	$a(\text{\AA})$	$V_o(\text{\AA}^3)$	$Density(g/cm^3)$	$E(a.u.)$
HF	3.955	62.10	6.49	-1511.670839
LDA	3.831	56.24	7.14	-1510.948553
PWGGA	3.911	59.82	6.71	-1515.006266
PBE	3.916	60.09	6.68	-1514.481171
B3LYP	3.917	60.13	6.67	-1514.616494
Exp. ^a	3.994	-	-	-
Th. ^a	3.975	-	-	-
Th. ^a	4.116	-	-	-
<hr/> <i>a.</i> Refs. [16, 17, 21] <hr/>				

Table 4.5: The elastic constants and bulk modulus computational results using the Hartree Fock and LDA, PWGGA and PBE potentials with basis set 2. (see sections 4.2, 4.4 and 4.5.) All values are in GPa.

	C_{11}	C_{12}	C_{44}	B
LDA	212.26	242.37	138.84	232.33
PWGGA	129.20	106.93	106.93	157.93
PBE	129.87	167.60	108.43	155.02
LSDA ^a	238.54	164.33	105.35	205.18
<hr/>				
<i>a.</i> Ref. [20]				

Table 4.6: Equation of state results for cubic $BaFeO_3$ with the Birch Murnaghan 3rd order equation. The energy-volume curve was fitted with eleven points and the range of volume around equilibrium was chosen as $\pm 10\%$ employing basis set 2 (see sections 4.2, 4.4 and 4.5. The value of the bulk modulus, B_{EL} is given in the last column for comparison.)

	$B_{EOS}(\text{GPa})$	$V_o(\text{\AA}^3)$	$E_0(a.u.)$	$B_{EL}(\text{GPa})$
LDA	160.64	59.83	-1515.0062726	
PWGGA	155.87	60.07	-1514.4811825	-
PBE	155.87	60.07	-1514.4811825	-
B3LYP	157.94	60.18	-1514.6165046	-
LSDA ^a	189.06	-	-	-
<hr/>				
<i>a.</i> Ref. [20]				

Table 4.7: The values of relaxed lattice constants (in \AA), ambient volume (in \AA^3), density (in gm/cm^3), and energy (in a.u.) for tetragonal $BaFeO_3$. The computations were done by using Hartree-Fock, DFT LDA, PWGGA, PBE and B3LYP potentials employing basis set 1. (see sections 4.2, 4.4 and 4.5.)

	$a(\text{\AA})$	$c(\text{\AA})$	c/a	$V_o(\text{\AA}^3)$	$Density(g/cm^3)$	$E_o(a.u.)$
HF	3.797	4.099	1.079	59.13	6.79	-1511.872043
LDA	3.708	4.222	1.138	58.08	6.91	-1510.962842
PWGGA	3.860	3.860	1.000	60.24	6.67	-1515.012308
PBE	3.830	4.125	1.077	60.53	6.63	-1514.48623
B3LYP	3.881	4.043	1.041	60.90	6.59	-1514.62652
Exp. [18]	3.997	4.031	1.008	64.42	-	-

Table 4.8: Equation of state results for tetragonal $BaFeO_3$ with the Birch Murnaghan 3rd order equation. The energy-volume curve was fitted with eleven points and the range of volume around equilibrium was chosen as $\pm 10\%$ employing basis set 1 (see sections 4.2, 4.4 and 4.5).

	$B_{EOS}(\text{GPa})$	$V_o(\text{\AA}^3)$	$E_0(a.u.)$
HF	200.00	59.20	-1511.8782039
LDA	138.07	58.08	-1510.962836
PWGGA	130.95	59.79	-1515.0123155
PBE	127.62	60.53	-1514.4862532
B3LYP	221.70	62.37	-1514.6283632

Table 4.9: The values of relaxed lattice constants (in \AA), ambient volume (in \AA^3), density (in gm/cm^3), and energy (in a.u.) for tetragonal $BaFeO_3$. The computations were done by using Hartree-Fock, DFT LDA, PWGGA and PBE potentials employing basis set 2. (see sections 4.2, 4.4 and 4.5.)

	$a(\text{\AA})$	$c(\text{\AA})$	c/a	$V_o(\text{\AA}^3)$	$Density(g/cm^3)$	$E_0(a.u.)$
HF	3.799	4.099	1.078	59.19	6.784	-1511.8693632
LDA	3.773	3.954	1.0479	56.29	7.133	-1510.949963
PWGGA	3.841	4.047	1.0536	59.71	6.725	-1515.009354
PBE	3.867	4.050	1.0473	60.57	6.629	-1514.4709459
Exp. [18]	3.997	4.031	1.008	64.427	-	-

Table 4.10: Equation of state results for tetragonal $BaFeO_3$ with the Birch Murnaghan 3rd order equation. The energy-volume curve was fitted with eleven points and the range of volume around equilibrium was chosen as $\pm 10\%$ employing basis set 2 (see sections 4.2, 4.4 and 4.5).

	$B_{EOS}(\text{GPa})$	$V_o(\text{\AA}^3)$	$E_0(a.u.)$
HF	197.55	59.24	-1511.869363
LDA	217.17	56.32	-1510.949958
PWGGA	154.22	59.71	-1511.869363
PBE	135.13	60.58	-1514.470945

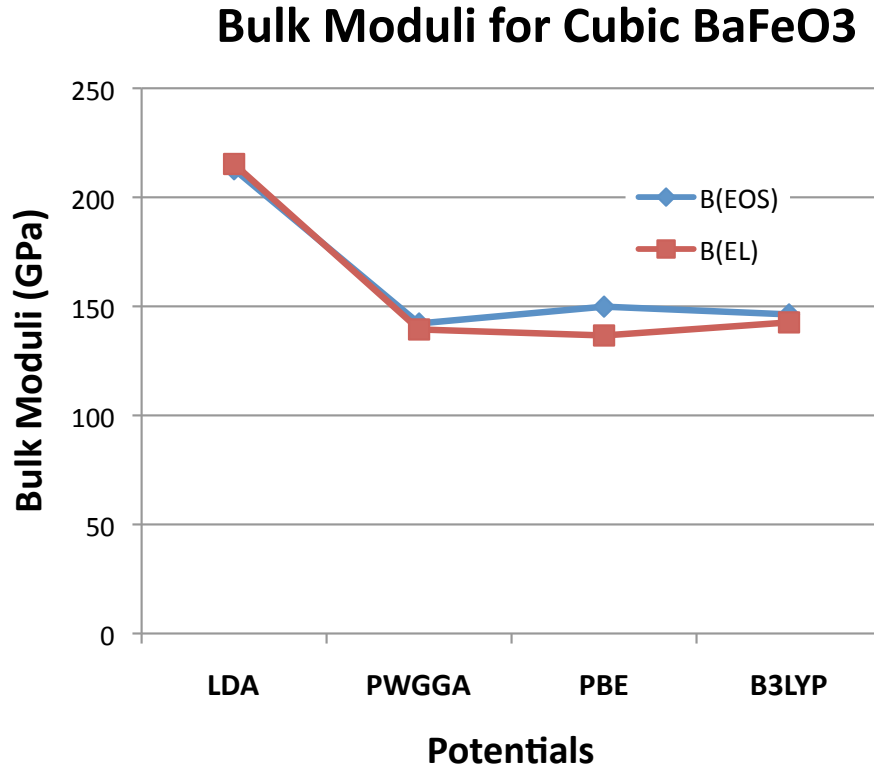


Figure 4.1: Computational values of bulk moduli for cubic $BaFeO_3$ are shown. B_{eos} and B_{el} represent the computational values obtained with EOS (equation of state) and ELASTCON (second-order elastic constants) algorithms.

References

- [1] Shruba Gangopadhyay, Talgat Inerbaev, Artm E. Masunov, Deanna Altilio, and Nina Orlovskaya. *ACS Appl. Mater. Interfaces*, 1:1512–1519, 2009.
- [2] Tinte S., Stachiotti M. G., Rodriguez C. O., Novikov D. L., and Christensen N. E. *Phys. Rev. B*, 58:11959–11963, 1998.
- [3] Mori and Saburo. *Journal of the American Ceramic Society*, 49:600–605, 1966.
- [4] W. D. Townes, J. H. Fang, and A. J. Perrotta. *Zeitschrift für Kristallographie*, 125:437–449, 1967.
- [5] J. Kreisel, G. Lucazeau, and H. Vincent. *Journal of Solid State Chemistry*, 137:127–137, 1998.
- [6] Shu yao Yan, Ying Xie, Tao Liu, and Hai tao Yu HuYao. *J. Phys. Condens. Matter*, 22:125501(7), 2010.
- [7] Rondinelli James M., Eidelson Aaron S., and Spaldin Nicola A. *Phys. Rev. B*, 79:205119, 2009.

- [8] K. Yamaurab C. Felsera and R. J. Cavab. *Journal of Solid State Chemistry*, 146:411–417, 1999.
- [9] Feng HongJian and Liu FaMin. *Chinese Phys. B*, 17:1874, 2008.
- [10] Ravindran P., Vidya R., Kjekshus A., Fjellvaag H., and Eriksson O. *Phys. Rev. B*, 74:224412, 2006.
- [11] Pardo V., Blaha P., Iglesias M., Schwarz K., Baldomir D., and Arias J. E. *Phys. Rev. B*, 70:144422–8, 2004.
- [12] V. Pardo, M. Iglesias, D. Baldomir, J. Castro, and J. E. Arias. *Solid State Communications*, 128:101–106, 2003.
- [13] Sadoc Aymeric, De Graaf, Coen, and Broer Ria. *Phys. Rev. B*, 75:165116, 2007.
- [14] King-Smith R. D. and Vanderbilt David. *Phys. Rev. B*, 49:5828–5844, 1994.
- [15] R. Dovesi, V. R. Saunders, C. Roetti, R. Orlando, C. M. Zicovich-Wilson, F. Pascale, B. Civalleri, K. Doll, N. M. Harrison, I. J. Bush, Ph. D’Arco, and M. Llunell. *CRYSTAL2006 User’s Manual*. University of Torino, University of Torino, Torino, Italy, 2006.
- [16] Verma A. S., Kumar A., and Bhardwaj S. R. *Phys. Stat. Sol. (B)*, 245:1520–26, 2008.
- [17] Li Feng-Ying, Jin Chang-Qing, You Shu-Jie, Xiao Chang-Jiang, Yu Ri Cheng,

- Wang Xiao-Hui, Liu Jing, Li Xiao-Dong, Li Yan-Chun, and Chen Liang-Chen. *Chin. Phy. Lett.*, pages 1249–52, 2006.
- [18] F. F. Hammad, A. K. Mohamed, and A. M. ElShabiny. *Egypt. J. Solids*, 31:55, 2008.
- [19] B. Xu, K. B. Yin, J. Lin, Y. D. Xia, X. G. Wan , J. Yin, X. J. Bai, J. Du, and Z. G. Liu. *Phys. Rev. B*, 79:134109, 2009.
- [20] H. Rached, D. Rached, M. Rabah, R. Khenata, and Ali H. Reshak. *Physica B Condensed Matter*, 405:3515–3519, 2010.
- [21] Roberto L. Moreira and Anderson Dias. *Journal of Physics and Chemistry of Solids*, pages 1617–1622, 2007.

Chapter 5

Spin-Strain Coupling in 3-*d*

Transition Metal Oxides

5.1 Introduction

The experimental verification of spin-dependent tunneling were started in early 70's by Tedrow and Julliere [1, 2]. In 1985, Johnson and Silsbee [3] discovered the coupling between the electron charge and spin in interfaces of transition metals. The GMR effect was discovered in a *Fe-Cr* superlattice by Albert Fert [4] and Peter Grünberg [5] in 1988. Due to success of GMR device, the spin field effect transistor was proposed

by [6]. These discoveries further influenced the research interest in the interfacial properties of thin film composites of transition metal oxides [7].

Researchers [8, 9, 10] employed the first-principle computational techniques and fabrication to explore the interfacial properties in ferroic composites. They observed that the elastic coupling depends upon a number of factors such as lattice strain, orbital overlaps and chemical bonding.

The crystal field theory and localized nature of d orbitals in oxide of transition metals is widely researched for transition metal oxides (TMOs)[11, 12, 13, 14]. However, the *ab-initio* computational techniques have not been employed to explore the coupling between the crystalline structure and electron spin angular momentum in TMOs.

We employed the *ab-initio* computations on a large variety of transition metal oxides of $Sc - Fe$. The CRYSTAL09 code is employed to compute the change in the FM/AFM energy and exchange energy by applying the hydrostatic compression and expansion of periodic unit cells of $BaScO_3$, $BaTiO_3$, $BaVO_3$, $BaCrO_3$, $BaMnO_3$ and $BaFeO_3$. The unrestricted Hartree Fock (UHF), Spin-DFT and Spin-hybrid potentials are employed for computing the UHF and FM/AFM exchange energy.

We chose the cubic crystalline materials of $BaScO_3$, $BaTiO_3$, $BaVO_3$, $BaCrO_3$, $BaMnO_3$ and $BaFeO_3$ to fully understand the factors responsible for the coupling. The supercells consisting of 02 unit cells were employed in these computations. Fig-

ures 5.1 and 5.2 show the clusters employed for cubic $BaTiO_3$ and $BaFeO_3$. The compressive and tensile strains were introduced in step-wise manner by reduction and expansion of the lattice constant for each transition metal oxide.

5.2 Computations

The Crystal09 code [15] is employed to compute the UHF and exchange energy for the ferromagnetic and antiferromagnetic spin polarization in each of the transition metal oxides. The unrestricted Hartree Fock (UHF), Spin-DFT and Spin-hybrid potentials are employed during these computations. Care is taken to keep the parameters of self consistent field (SCF) process consistent during these computations. The optimized lattice constants, computed with BILLY script, were employed during these computations. Same basis sets were employed for Ba and O atoms consistently whereas the basis set for the specific transition metal was replaced.

The computational results of open-shell and exchange energy computed with UHF, Spin-DFT and Spin-hybrid potentials for the cubic crystalline systems are shown in Tables 5.1 - 5.6 and Figures 5.3 - 5.8. The open-shell and exchange energies are computed at optimized crystalline structure of each material. Four additional computations are carried out for each oxide by employing increments of .005 in values of lattice constants.

5.2.1 Quantum mechanical model

Maekawa *et al* [12] has performed a detailed study on the quantum mechanical interpretation of crystal field theory (CFT) for manganite transition metal oxides (TMOs). In TMOs, a delicate balance exists between the crystal field and Hund's pairing energy. The energy degeneracy in these materials is partially lifted due to the crystal field formed by the cations and anions. The crystal field depends upon the nature of chemical bonding between the transition metal and O atoms.

It has been observed that changes in FM/AFM energy and exchange energy appear during compression and expansion of the crystalline lattice. Change in UHF and FM/AFM exchange energy may be caused by the coupling between the localized d -orbitals and crystalline structure. The chemical bonding between transition metal and O atom results in a large overlap causing the fluctuations in FM/AFM energy and exchange energy for $BaVO_3$, $BaCrO_3$ and $BaMnO_3$.

The quantum mechanical model can be equally applicable to Manganites ($AMnO_3$), Titanates ($ATiO_3$) and Vanadates (AVO_3) as the crystal field varies in all these TMOs [12]. The Hamiltonian for a transition metal oxide based upon the splitting of d orbitals due to the crystal field is given in Eq. 5.1

$$H_{eff} = H_{hund} + H_{t_{2g}} + H_{e_g} \quad (5.1)$$

The H_{e_g} term in Eq. 5.1 represents the energy component due to e_g sub-orbitals which are σ -bonded with the p_x and p_y sub-orbitals. The $H_{t_{2g}}$ term represents the energy component due to t_{2g} sub-orbitals which are π -bonded the p_z sub-orbitals [12].

The term H_{hund} expresses the energy term associated with Hund's rule

$$H_{hund} = J_H \sum_i S_i S_i^{t_{2g}} \quad (5.2)$$

The second term in Eq. 5.1 due to localized t_{2g} orbital results in an antiferromagnetic spin polarization.

$$H_{t_{2g}} = J_{ij} S_i^{t_{2g}} S_j^{t_{2g}} \quad (5.3)$$

Equation 5.4 expresses the H_{e_g} as

$$H_{e_g} = \Delta \sum_i L_{iz} + \sum_{\langle ij \rangle \sigma \gamma \gamma'} t_{\gamma \gamma'}^{ij} (a_{i\gamma\sigma}^\dagger a_{j\gamma'\sigma}) + \sum_{\beta} H_{U_{\beta}} \quad (5.4)$$

In Eq. 5.4, the subscripts i and j stand for the nearest neighbors, $a_{i\gamma\sigma}^\dagger$ and $a_{j\gamma'\sigma}$ are the creation and annihilation operators, respectively. Small changes in the electron energy are introduced due to the compression and expansion of the lattice constant as shown in Table 5.1-5.5 and Figures 5.3 to 5.8.

$$t = \sum_{\langle ij \rangle \sigma \gamma \gamma'} t_{\gamma}^{ij \gamma'} (a_{i \gamma \sigma}^{\dagger} a_{j \gamma' \sigma}) \quad (5.5)$$

$$t_{ij}^{\gamma \gamma'} = \alpha_{\gamma \gamma'} t_{oij} \quad (5.6)$$

The electrostatic energy term U expresses the on-site electron correlation in transition metal cations resulting in the electron localization on transition metal sites. The symbol t in Eq. 5.5 is the hopping integral expressing electrons hopping between i and j sites.

The term $\Delta\epsilon$ in Eq. 5.7 expresses the crystal field energy and the term $\sum_i T_i$ shows the orbital angular momentum [12] in TMOs.

$$\Delta \epsilon = \Delta \sum_i T_i \quad (5.7)$$

5.3 Results

The computations of FM/AFM and exchange energy were performed with Hartree Fock, DFT-LDA, DFT-PWGGA and DFT-B3LYP. An atomic cluster containing 02 unit cells was employed for each crystalline system. The atomic matrix used in these

computations is :

$$\begin{pmatrix} a/2 & a/2 & a \\ a/2 & a & a/2 \\ a & a/2 & a/2 \end{pmatrix}$$

The unrestricted Hartree Fock method was employed to compute changes in exchange energy for small strains on the unit cell of cubic crystalline ABX_3 systems. The lattice sites A and X contained Ba and O atoms while B site was replaced with Sc , Ti , V , Cr , Mn and Fe transition metals. An interdependence between the ferromagnetic, antiferromagnetic exchange and lattice strain is found. It is observed that the exchange energy is lowered or enhanced consistently for hydrostatic compression and expansion of cubic $BaScO_3$, $BaTiO_3$, $BaVO_3$, $BaCrO_3$, $BaMnO_3$ and $BaFeO_3$.

The computational results are shown in Table 5.1 - 5.6 and Figures 5.3-5.6. Figures 5.3-5.6 show a consistent trend of increase in energy with expansion of cubic crystalline structure. A linear increase in FM/AFM energy and exchange energy vs. applied hydrostatic strain is observed for $BaScO_3$, $BaTiO_3$ and $BaFeO_3$. Whereas, oscillations in FM/AFM energy and exchange energy vs. applied strain are seen for $BaVO_3$, $BaCrO_3$ and $BaMnO_3$. In Tables 5.1 - 5.6 the $E_{fm.}$, $E_{exch.}^{fm.}$, $E_{afm.}$ and $E_{exch.}^{afm.}$ terms represent the UHF energy for FM spin polarization, FM exchange energy, UHF energy for AFM spin polarization and AFM exchange energy respectively.

Table 5.1 show the computational results for cubic $BaScO_3$ achieved with Hartree

Fock, DFT-LDA, DFT-PWGGA and DFT-B3LYP. The FM energy is lower than AFM energy for HF and non-local DFT potentials whereas AFM energy is lower than FM energy for DFT-LDA potential.

Table 5.2 shows the computational results for cubic $BaTiO_3$. The Hartree Fock, DFT-PWGGA and DFT-B3LYP potentials were employed. The AFM energy is lower than FM energy for HF and DFT-PWGGA potentials.

Table 5.3 shows the computational results for cubic $BaVO_3$. The Hartree Fock, DFT-LDA, DFT-PWGGA and DFT-B3LYP potentials were employed. FM energy was lower than AFM energy for HF and B3LYP potentials.

Table 5.4 shows the computational results of cubic $BaCrO_3$. The AFM energy was lower in value than FM energy computed with HF and DFT potentials. Table 5.5 show the computational results of cubic $BaMnO_3$. HF, DFT-LDA, DFT-PWGGA potentials were employed. For optimized crystalline structure, the FM energy was lower than AFM energy for DFT-LDA and DFT-PWGGA potentials. For HF and DFT-B3LYP potentials, the AFM energy was lower than FM energy.

Table 5.6 shows the computational results of cubic $BaFeO_3$ done with HF, DFT-LDA and DFT-PWGGA and DFT-B3LYP potentials. For HF and DFT-B3LYP potentials, the FM energy was lower than AFM energy. The FM and AFM energy was equal in value for DFT-PWGGA and DFT-LDA potentials.

5.4 Analysis of results

Figures 5.6-5.8 show variations in Hartree Fock FM energy for hydrostatic compression and expansion of cubic $BaVO_3$, $BaCrO_3$ and $BaMnO_3$. It is observed that Figures 5.3, 5.5 and 5.8 show no fluctuations in the FM energy for $BaScO_3$, $BaTiO_3$ and $BaFeO_3$.

For cubic $BaVO_3$, $BaCrO_3$ and $BaMnO_3$, the atomic orbitals of transition metals (TMs) and O overlap with each other during hydrostatic compression. In case of $BaVO_3$, $BaCrO_3$ and $BaMnO_3$, the electron spins of TM and O atoms fluctuate for compression as well as expansion of crystals. Oscillatory trend in $BaVO_3$, $BaCrO_3$ and $BaMnO_3$ is accompanied by the overlap between the atomic orbitals resulting in spin fluctuations. The distorted crystalline structure of $BaVO_3$, $BaCrO_3$ and $BaMnO_3$ results in higher orbital overlaps and spin fluctuations.

It can be seen in Tables 5.1-5.6 and Figures 5.3-5.8 that there is a lowering of FM/AFM and exchange energies due to during hydrostatic compression of crystals. According to crystal field theory, the degeneracy is lifted with the compression. The effects of compression on the lowering of the FM and exchange energies has been observed for manganites and cuprates by ref. [12]. For $BaVO_3$, $BaCrO_3$, $BaMnO_3$ and $BaFeO_3$ with more electrons occupying the e_g levels, the FM and exchange energies are more sensitive to hydrostatic compressions and expansions. In case of

$BaScO_3$ and $BaTiO_3$ the electron spins belonging tot_{2g} orbitals do not fluctuate due to large lattice parameter a .

The oxides of transition metal have varied number of electrons in their highly correlated d - orbitals. The contracted wavefunctions of d electrons in $BaScO_3$, $BaTiO_3$, $BaVO_3$, $BaMnO_3$ and $BaFeO_3$ experience the varied degree of competitive forces [16] due to electrostatic repulsion. The electrostatic forces may localize the electrons around ionic cores while the hybridization may favor the overlaps between valence p and d orbitals of O and transition metals to delocalize the valence electrons. Moreover, the ionic and covalent components are varied by hydrostatic strains on crystals. For hydrostatic compression, the ionic bonding decreases at the expense of covalent bonding.

In case of $BaScO_3$, the lower value of FM total energy and FM exchange energy needs further exploration. The charge density maps for $BaScO_3$ may help in understanding the chemical bonding and its role in determining the FM energy.

The weak nature of π bonding between $Ti-O$ t_{2g} - p sub-orbitals respectively results in antiferromagnetic exchange in $BaTiO_3$ as shown in Table 5.2. While σ bonding between transition metal e_g and oxygen p electrons in V to Fe results in ferromagnetic exchange as can be seen in Tables 5.3-5.6. If e_g sub-orbital is occupied by electron, it changes the position of atoms and crystalline lattice structure undergoes Jahn Teller distortions. The change in the position of atoms, usually coupled strongly with e_g

electrons, may not happen in $BaTiO_3$ as there are no electrons to occupy e_g energy levels. The effect of compressive strains on cubic $BaTiO_3$ can be observed in Table 5.2 and Figure 5.5.

The transition metal e_g and oxygen p sub-orbitals form a stronger σ bond whereas the transition metal t_{2g} and oxygen p sub-orbitals form a weaker π bond. The σ and π has consequences to determine the ferromagnetic or antiferromagnetic energy.

5.5 Concluding Remarks

We have employed first principles computational techniques to compute the coupling between the electron spin and lattice strain. The spin exchange is computed for a wide variety of perovskite cubic crystalline transition metal oxides. It is observed that the compressive strain on the bulk lattice structure results in the lowering of the spin exchange energy. It is also observed that the compressive strain lowers the exchange energy in all transition metal oxides. The lowering of the exchange energy can be interpreted as spin-strain coupling between the transition metal e_g and p orbitals forming a σ bond.

Table 5.1: Computations of $E_{fm.}$, $E_{exch.}^{fm.}$, $E_{afm.}$ and $E_{exch.}^{afm.}$ are done with Hartree Fock, DFT-LDA, DFT-PWGGA and DFT-B3LYP potentials for cubic $BaScO_3$. Optimized values of lattice constant a are used. The units of energy are in Hartree.

	a	E_{fm}	$E_{exch.}^{fm}$	E_{afm}	$E_{exch.}^{afm}$
HF	4.222	-2019.15430	-132.65117	-2019.0250	-132.4049
LDA	4.095	-2017.13884	-	-2017.1412	-
PWGGA	4.175	-2024.1167	-	-2024.1142	-
B3LYP	4.218	-2023.7225	-	-2023.7043	-
HF	4.227	-2019.1544	-132.6425	-2019.02520	-132.3953
LDA	4.100	-2017.1388	-	-2017.1412	-
PWGGA	4.180	-2024.1170	-	-2024.1145	-
B3LYP	4.223	-2023.7225	-	-2023.7042	-
HF	4.232	-2019.1545	-132.6330	-2019.02598	-132.3766
LDA	4.105	-2017.1388	-	-2017.1412	-
PWGGA	4.185	-2024.1172	-	-2024.11479	-
B3LYP	4.228	-2023.7224	-	-2023.7042	-
<i>Exp.</i> ^a	4.13	-	-	-	-
HF	4.237	-2019.1545	-132.6240	-2019.0283	-132.3673
LDA	4.110	-2017.1387	-	-2017.1411	-
PWGGA	4.190	-2024.1173	-	-2024.1148	-
B3LYP	4.233	-2023.7224	-	-2023.7040	-
HF	4.242	-2019.1545	-132.6150	-2019.0282	-132.3578
LDA	4.115	-2017.1386	-	-2017.1409	-
PWGGA	4.195	-2024.1173	-	-2024.1148	-
B3LYP	4.238	-2023.7222	-	-2023.7038	-

a. See Refs. [17]

Table 5.2: Computations of $E_{fm.}$, $E_{exch.}^{fm.}$, $E_{afm.}$ and $E_{exch.}^{afm.}$ are done are done with Hartree Fock, DFT-LDA and DFT-B3LYP potentials for cubic $BaTiO_3$. Optimized values of lattice constant a are used. The units of energy are Hartree.

	a	$E_{fm.}$	$E_{exch.}^{fm.}$	$E_{afm.}$	$E_{exch.}^{afm.}$
HF	4.015	-2196.0888	-138.4584	-2196.7306	-138.7112
LDA	3.935	-2194.5160	-	-2194.6420	-
B3LYP	4.218	-2201.3644	-	-2201.3644	-
HF	4.020	-2196.0907	-138.4465	-2196.7306	-138.6977
LDA	3.940	-2194.5166	-	-2194.6421	-
B3LYP	4.223	-2201.3644	-	-2201.3644	-
HF	4.025	-2196.0907	-138.43402	-2196.7306	-138.6842
LDA	3.940	-2194.5171	-	-2194.6421	-
B3LYP	4.228	-2201.3644	-	-2201.3644	-
<i>Exp.</i> ^a	3.94,4.02,4.03	-	-	-	-
HF	4.030	-2196.0925	-138.4222	-2196.7305	-138.6708
LDA	3.945	-2194.5175	-	-2194.6421	-
B3LYP	4.233	-2201.2021	-	-2201.3642	-
HF	4.035	-2196.0943	-138.4107	-2196.7304	-138.6577
LDA	3.950	-2194.5178	-	-2194.6419	-
B3LYP	4.238	-2120.7983	-	-2201.3641	-

a. See Ref. [18]

Table 5.3: Computations of E_{fm} , E_{exch} , E_{afm} and E_{exch}^{afm} are done with Hartree Fock, DFT-LDA, DFT-PWGGA and DFT-B3LYP potentials for cubic $BaVO_3$. Optimized values of lattice constant a are used. The units of energy are Hartree.

	a	E_{fm}	E_{exch}^{fm}	E_{afm}	E_{exch}^{afm}
HF	3.907	-2385.1472	-144.855	-2385.0032	-144.3554
LDA	3.921	-2383.4052	-	-2383.4089	-
PWGGA	3.969	-2390.8149	-	-2390.8073	-
B3LYP	3.919	-2390.2370	-	-2390.2264	-
HF	3.912	-2385.1538	-144.8675	-2385.0036	-144.3406
LDA	3.926	-2383.4139	-	-2383.4169	-
PWGGA	3.974	-2390.8095	-	-2390.8073	-
B3LYP	3.924	-2390.2463	-	-2390.2272	-
HF	3.917	-2385.1545	-144.8415	-2385.0038	-144.3259
LDA	3.931	-2383.4162	-	-2383.4162	-
PWGGA	3.979	-2390.8096	-	-2390.8148	-
B3LYP	3.929	-2390.2473	-	-2390.2180	-
<i>Theory</i> ^a	3.843-3.900	-	-	-	-
HF	3.922	-2385.1545	-144.8774	-2385.0040	-144.3112
LDA	3.936	-2383.4155	-	-2383.4072	-
PWGGA	3.984	-2390.8099	-	-2390.8074	-
B3LYP	3.934	-2390.2482	-	-2390.2187	-
HF	3.927	-2385.1591	-144.8717	-2385.0041	-144.2966
LDA	3.946	-2383.4036	-	-2383.4067	-
PWGGA	3.989	-2390.8098	-	-2390.8072	-
B3LYP	3.939	-2390.2485	-	-2390.2286	-

a. See Ref. [19]

Table 5.4: Computations of E_{fm} , E_{exch}^{fm} , E_{afm} and E_{exch}^{afm} are done with Hartree Fock, DFT-PWGGA and DFT-B3LYP potentials for cubic $BaCrO_3$. Optimized values of lattice constant a are used. The units of energy are Hartree.

	a	E_{fm}	$E_{exch.}$	E_{afm}	$E_{exch.}$
HF	3.890	-2586.0427	-151.8044	-2585.2942	-150.2527
PWGGA	3.932	-2591.6821	-	-2591.6821	-
B3LYP	3.930	-2591.0157	-	-2590.9943	-
HF	3.895	-2586.0452	-151.7922	-2585.2942	-150.2385
PWGGA	3.937	-2591.6821	-	-2591.6821	-
B3LYP	3.935	-2591.0160	-	-2590.9801	-
HF	3.900	-2586.0477	-151.7802	-2585.2943	-150.2243
PWGGA	3.942	-2591.7052	-	-2591.6821	-
B3LYP	3.940	-2590.9938	-	-2590.9938	-
<i>Theory</i> ^a	3.8536	-	-	-	-
HF	3.905	-2586.0487	-151.7666	-2585.2916	-150.2102
PWGGA	3.947	-2591.7055	-	-2591.6820	-
B3LYP	3.945	-2591.0873	-	-2590.9938	-
HF	3.910	-2586.0509	-151.7546	-2585.2914	-150.1961
PWGGA	3.952	-2591.7058	-	-2591.6819	-
B3LYP	3.950	-2591.1006	-	-2590.9797	-

a. See Ref. [20]

Table 5.5: Computations of E_{fm} , E_{exch}^{fm} , E_{afm} and E_{exch}^{afm} are done with DFT-LDA, DFT-PWGGA and DFT-B3LYP potentials for cubic $BaMnO_3$. Optimized values of lattice constant a are used. The units of energy are Hartree.

	a	E_{fm}	$E_{exch.}$	E_{afm}	$E_{exch.}$
HF	3.874	-704.9155	-76.8556	-704.9916	-77.1601
LDA	3.822	-706.9945	-	-706.9888	-
PWGGA	3.896	-710.6341	-	-710.5635	-
B3LYP	3.925	-710.1267	-	-709.9275	-
HF	3.879	-705.9401	-78.2257	-704.9926	-77.1503
LDA	3.827	-706.9945	-	-706.9887	-
PWGGA	3.901	-710.6285	-	-710.5634	-
B3LYP	3.930	-710.1269	-	-709.9272	-
HF	3.884	-705.9412	-78.2206	-704.9935	-77.1405
LDA	3.832	-707.0306	-	-706.9892	-
PWGGA	3.906	-710.6316	-	-710.5634	-
B3LYP	3.935	-710.1295	-	-709.9268	-
$Exp.^a$	3.806	-	-	-	-
HF	3.889	-705.9423	-78.2192	-704.9943	-77.1310
LDA	3.837	-707.0296	-	-706.9890	-
PWGGA	3.911	-710.6293	-	-710.5632	-
B3LYP	3.940	-710.1291	-	-709.9255	-
HF	3.894	-704.9130	-76.8050	-704.9950	-77.1214
LDA	3.842	-707.0255	-	-706.9880	-
PWGGA	3.916	-710.6404	-	-710.5630	-
B3LYP	3.945	-	-	-709.9250	-

a. see Ref. [21]

Table 5.6: Computations of E_{fm} , E_{exch}^{fm} , E_{afm} and E_{exch}^{afm} are done with Hartree Fock, DFT-LDA, DFT-PWGGA and DFT-B3LYP potentials for cubic $BaFeO_3$. Optimized values of lattice constant a are used. The units of energy are Hartree.

	a	E_{fm}	$E_{exch.}$	E_{afm}	$E_{exch.}$
HF	4.155	-3023.9438	-165.2933	-3023.5233	-164.7191
LDA	3.852	-3021.9662	-	-3021.9065	-
PWGGA	3.917	-3030.0156	-	-3030.01562	-
B3LYP	3.927	-3029.4513	-	-3029.2331	-
HF	4.160	-3023.9442	-165.2866	-3023.5236	-164.7117
LDA	3.857	-3021.9126	-	-3021.9059	-
PWGGA	3.922	-3030.0935	-	-3030.0156	-
B3LYP	3.932	-3029.4524	-	-3029.2398	-
HF	4.165	-3023.9445	-165.2800	-3023.5238	-164.7043
LDA	3.862	-3021.9054	-	-3021.9054	-
PWGGA	3.927	-3030.01553	-	-3030.01553	-
B3LYP	3.937	-3029.4524	-	-3029.2387	-
<i>Exp.</i> ^a	3.994	-	-	-	-
HF	4.170	-3023.9448	-165.2733	-3023.5239	-164.6970
LDA	3.867	-3021.9665	-	-3021.9047	-
PWGGA	3.932	-3030.0947	-	-3030.01542	-
B3LYP	3.942	-3029.4534	-	-3029.2385	-
HF	4.175	-3023.9451	-165.2668	-3023.5241	-164.6897
LDA	3.872	-3021.9040	-	-3021.9040	-
PWGGA	3.937	-3030.0952	-	-3030.0152	-
B3LYP	3.947	-3029.4544	-	-3029.2383	-

a. see Ref. [21]

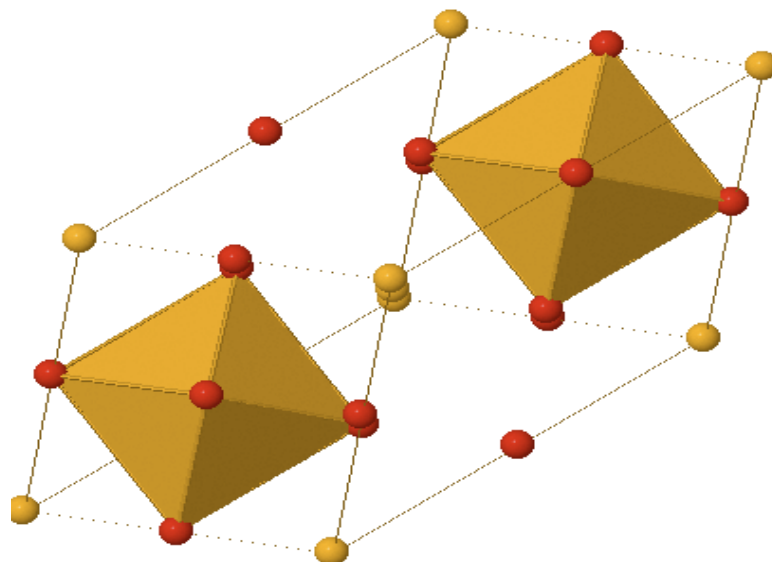


Figure 5.1: An octahedral is formed by O atoms having Fe atom in the middle. Yellow and red color spheres represent Ba , O and Fe atoms could not be seen as these are positioned in the middle of each cage in a perovskite $BaFeO_3$.

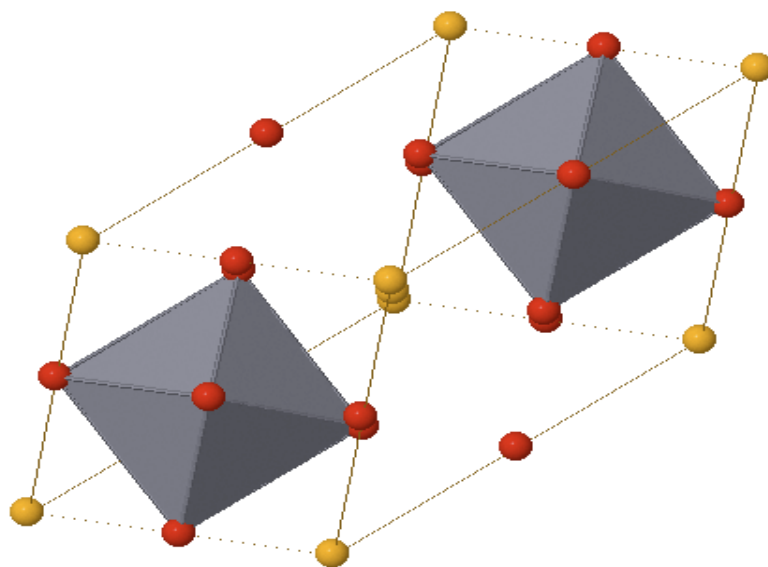


Figure 5.2: An octahedral is formed by O atoms having Fe atom in the middle. Yellow and red color spheres represent Ba and O while grey colored Ti atoms are positioned in the middle of each cage in a perovskite $BaTiO_3$.

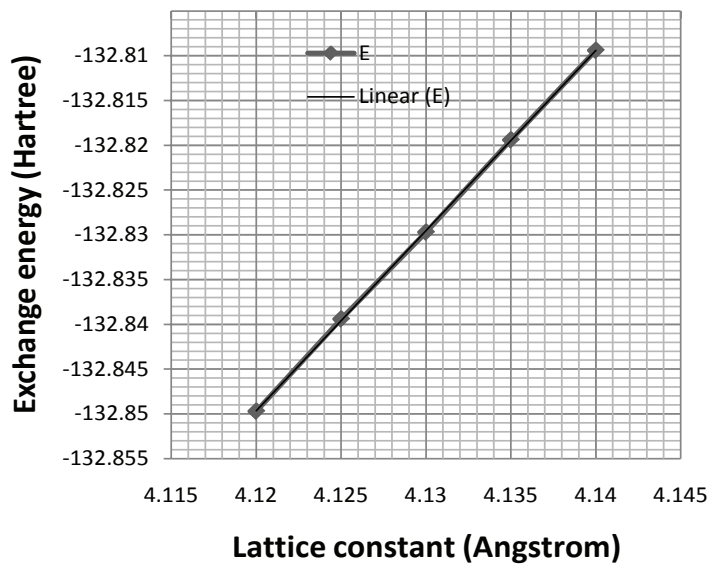


Figure 5.3: Exchange energy vs. lattice strain for cubic $BaScO_3$. A decrease in exchange energy can be seen for the compression of lattice. The straight line is drawn to signify the linearity of the trend.

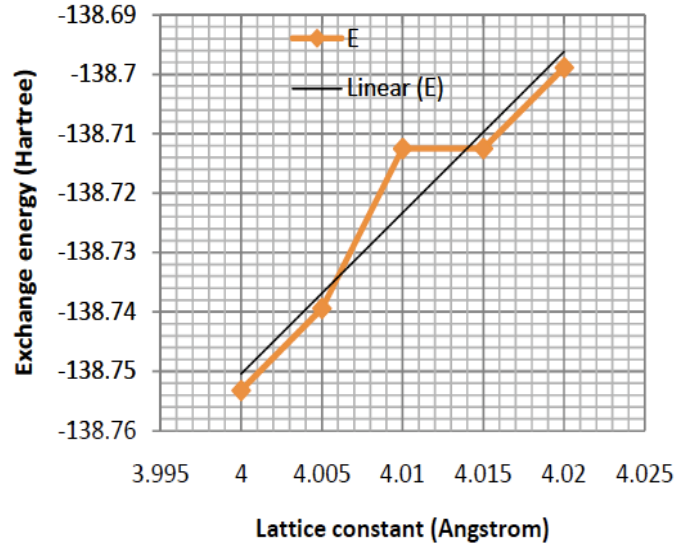


Figure 5.4: Exchange energy vs. lattice strain for cubic $BaTiO_3$. A decrease in exchange energy can be seen for the compression of lattice. The straight line is drawn to signify the linearity of the trend.

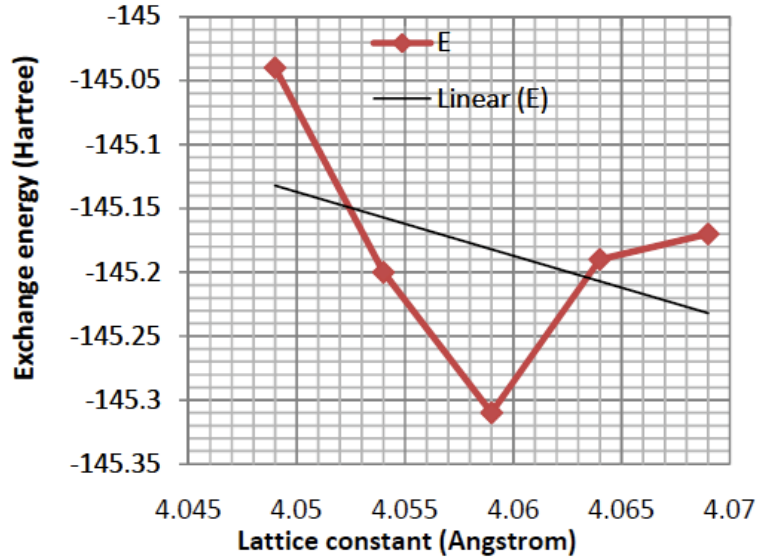


Figure 5.5: Exchange energy vs. lattice strain for cubic $BaVO_3$. A decrease in exchange energy can be seen for the compression of lattice. There is smaller deviation from the linear trend.

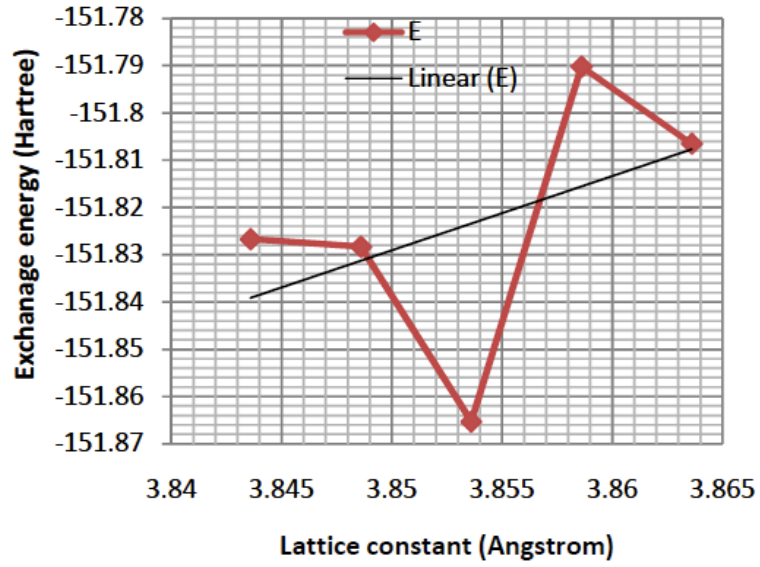


Figure 5.6: Exchange energy vs. lattice strain for cubic $BaCrO_3$. A slight increase in the exchange energy can be seen for the compression of lattice. The nonlinear dependence of the exchange energy on lattice strain is more pronounced.

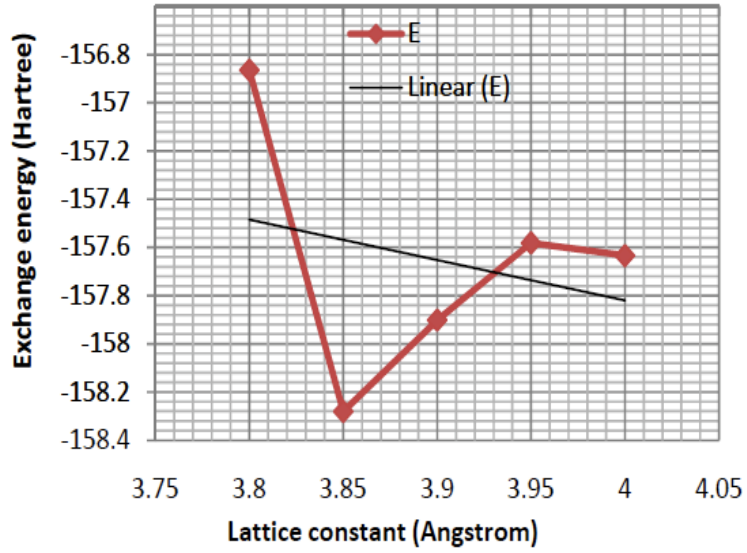


Figure 5.7: Exchange energy vs. lattice strain for cubic $BaMnO_3$. A decrease in exchange energy can be seen for the compression of lattice. The oscillatory character of exchange energy is also persistent.

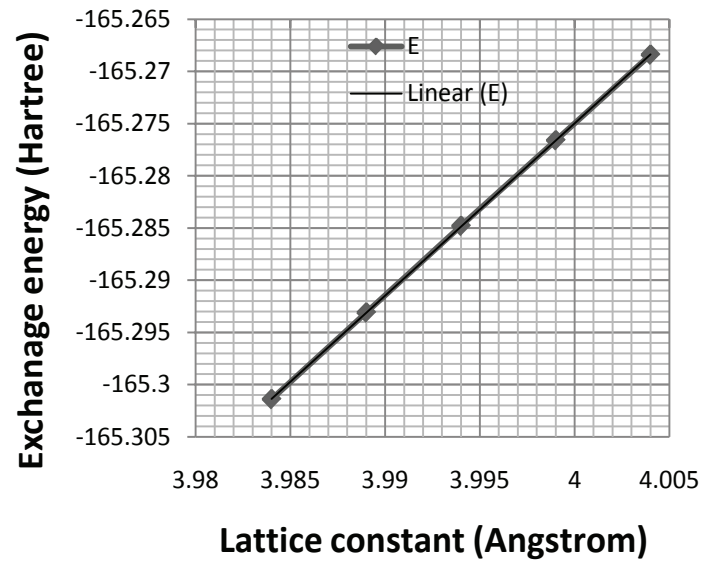


Figure 5.8: Exchange energy vs. lattice strain for cubic $BaFeO_3$. The non-linear dependence of the exchange energy on the compression of lattice can be observed. Exchange energy has slightly increased with the compression of the lattice in this case.

References

- [1] P. M. Tedrow and R. Meservey. *Phys. Rev. B*, 7:318–326, 1973.
- [2] M. Julliere. *Physics Letters A*, 54:225–226, 1975.
- [3] Mark Johnson and R. H. Silsbee. *Phys. Rev. Lett.*, 55:1790–1793, 1985.
- [4] Baibich M. N., Broto J. M., Fert A., and Chazelas J. *Phys. Rev. Lett.*, 61:2472–2475, 1988.
- [5] Binasch G., Grünberg P., and Zinn W. Saurenbach F. *Phys. Rev. B*, 39:4828–4830, 1989.
- [6] Supriyo Datta and Biswajit Das. *Appl. Phys. Lett.*, pages 665–667, 1990.
- [7] Mangalam R. V. K., Ray N., Waghmare U. V., Sundaresan A., and Rao C.N.R. *Sol Stat Com*, 149:367–70, 2009.
- [8] Evgeny Y. Tsymbal, Oleg N. Mryasov, and Patrick R. LeClair. *J. Phys. Condens. Matter*, 15:R109–R142, 2003.

- [9] Chun Gang Duan, Julian P. Velev, R. F. Sabirianov, W. N. Mei, S. S. Jaswal, and E. Y. Tsymbal. *Applied Physics Letters*, 92:1–3, 2008.
- [10] J. P. Velev, P. A. Dowben, E. Y. Tsymbal, S. J. Jenkin, and A.N. Caruso. *Surface Science Reports*, 63:400–425, 2008.
- [11] Goodenough J. Electron-Lattice Interactions in Manganese-Oxide. *Perovskites, Fundamental Materials Research*, pages 127–133, 2002.
- [12] Ishihara Sumio, Okamoto Satoshi, and Maekawa Sadamichi. *Physics of Transition Metal Oxides*. 1997.
- [13] C. N. Rao and B. Raveau. *Annual Review of Physical Chemistry*, pages 291–326, 1989.
- [14] Y. Tokura and N. Nagaosa. *Science*, 288:462–468, 2000.
- [15] R. Dovesi, V. R. Saunders, C. Roetti, R. Orlando, C. M. Zicovich-Wilson, F. Pascale, B. Civalleri, K. Doll, N. M. Harrison, I. J. Bush, Ph. D’Arco, and M. Llunell. *CRYSTAL2006 User’s Manual*. University of Torino, University of Torino, Torino, Italy, 2006.
- [16] Ahn K. H., Lookman T., and Bishop A. R. *Nature*, 2004.
- [17] Takahisa Omata, Tomonao Fukea, and Shinya OtsukaYao-Matsuo. *Solid State Ionics*, 177:2447–2451, 2006.

- [18] S. Piskunov, E. Heifets, R. I. Eglitis, and G. Borstel. Bulk properties and electronic structure of $SrTiO_3$, $BaTiO_3$, $PbTiO_3$ perovskites: An *ab initio* HF/DFT study. *Comput. Mater. Sci.*, pages 165–178, 2004.
- [19] Shu yao Yan, Ying Xie, Tao Liu, HaiTao, and Yu HuYao. *J. Phys. Condens. Matter*, page 125501, 2010.
- [20] Zhu Z. H. and Yan X. H. *Journal of Applied Physics*, 106:1–5, 2009.
- [21] A.S. Vermaa and V.K. Jindal. *Journal of Alloys and Compounds*, 485:514–518, 2009.

Chapter 6

Conclusions

We have performed the *ab-initio* computations on the electronic structure, elastic properties and spin-strain coupling in 3-*d* transition metal oxides with perovskite crystalline structure. The electronic structure, elastic constants and bulk moduli are computed for the tetragonal $BaTiO_3$, rutile TiO_2 , cubic and tetragonal $BaFeO_3$. The *ab-initio* computations are also carried out to explore the coupling between the FM/AFM properties and crystalline lattice structures of 3-*d* transition metal oxides of $BaScO_3$, $BaTiO_3$, $BaVO_3$, $BaMnO_3$, $BaCrO_3$ and $BaFeO_3$.

We computed the electronic structure, elastic constants and bulk moduli of tetragonal $BaTiO_3$. These computations were done to fill the research gap as the *ab-initio* computations of the elastic constants and bulk moduli were not carried out prior to

our work. We compared our computational results with the experimental values of the lattice parameters, elastic constants and bulk moduli from various sources. We have pioneered to explore the elastic properties of the tetragonal $BaTiO_3$. Tables 2.3 - 2.6 and Figures 2.1 - 2.4 show the lattice parameters, elastic constants and bulk moduli results for tetragonal $BaTiO_3$.

The computations of lattice parameters and elastic properties of rutile TiO_2 was performed to crosscheck the reliability of our computational values. The experimental and computational values of lattice parameters, elastic constants and bulk moduli for rutile TiO_2 are widely explored by researchers. Our *ab-initio* computational results show a significant agreement with the computational and experimental values of lattice parameters determined by other researchers. In chapter 3, the Tables 3.1 - 3.6 show the values of lattice parameters, elastic constants and bulk moduli for rutile TiO_2 .

After a detailed understanding of the factors that can enhance the effectiveness of our computational results for tetragonal $BaTiO_3$ and rutile TiO_2 , we explored the crystalline structure, elastic constants and bulk moduli of cubic and tetragonal $BaFeO_3$. Computational values of optimized lattice parameters, elastic constants and bulk moduli of cubic and tetragonal $BaFeO_3$ were determined with HF, DFT and hybrid potentials. We employed the HF, DFT and hybrid potentials, basis sets and other computational parameters which were already tested on tetragonal $BaTiO_3$ and ru-

tile TiO_2 crystalline systems. The computational values of lattice parameters of cubic and tetragonal $BaFeO_3$ were compared with the theoretical and experimental values performed.

A significant agreement has been observed between our computational values of lattice parameters and the values obtained by other researchers. The values of elastic constants and bulk moduli for cubic $BaFeO_3$ were compared with *ab-initio* computations done with Local Spin Density Approximation (LSDA) potential by Rached *et al.* An agreement in the values of elastic constants and bulk moduli was observed. In chapter 4, Tables 4.1 - 4.10 show the lattice parameters, elastic constants and bulk moduli of cubic and tetragonal $BaFeO_3$.

The 3-*d* transition metal oxides with a perovskite crystalline structure undergo a coupling between the electron spin, charge, atomic orbitals and crystalline structure due to electronic configuration of *d*-orbitals. The computations were carried out to explore the coupling between the FM/AFM properties resulting from parallel and antiparallel spin polarization and hydrostatic strains on the cubic crystalline structures of $BaScO_3$, $BaTiO_3$, $BaVO_3$, $BaMnO_3$, $BaCrO_3$ and $BaFeO_3$.

The Unrestricted Hartree Fock (UHF), Spin-DFT and Spin-hybrid DFT potentials were employed for computing the total energy for different spin polarization. Basis sets for *Ba* and *O* atoms employed in $BaScO_3$, $BaTiO_3$, $BaVO_3$, $BaMnO_3$, $BaCrO_3$ and $BaFeO_3$ crystalline systems were chosen from CRYSTAL09 code basis set library.

The computational values of total energy and FM/AFM spin exchange energy showed an increase in UHF energy and FM/AFM spin exchange energy for hydrostatic expansion of all crystalline systems. We also observed a decrease in UHF energy and FM/AFM exchange energy for all crystalline systems under hydrostatic compression. A linear relationship between the crystalline structure and FM/AFM spin exchange was observed for cubic $BaScO_3$, $BaTiO_3$ and $BaFeO_3$. Whereas an oscillatory relationship between the crystalline structure and FM/AFM spin exchange was observed for cubic $BaVO_3$, $BaMnO_3$ and $BaCrO_3$. The linear relationship between lattice strain and exchange energy for cubic $BaScO_3$, $BaTiO_3$ and $BaFeO_3$ was accompanied with no changes in spin. It was observed that the spin transitions are coupled with the electronic orbitals and crystalline lattice. Tables 5.1 - 5.6 and figures 5.1 - 5.8 presented in chapter 5 show computational results of change in FM/AFM energy due to hydrostatic compression and expansion for $BaScO_3$, $BaTiO_3$, $BaVO_3$, $BaMnO_3$, $BaCrO_3$ and $BaFeO_3$.

6.1 Research accomplishments

† We have pioneered to perform the *ab-initio* computations on electronic structure and elastic properties of tetragonal $BaTiO_3$ successfully.

† A considerable agreement was observed between the computational and the

experimental values of lattice parameters and bulk moduli for hybrid potentials employed in combination with basis set 1.

† A more significant agreement between the computational values of optimized lattice parameters and experimental values was also observed for rutile TiO_2 .

† The merit of these computational methods was confirmed by the agreement between our computational results and experimental values from other researchers.

† We have also pioneered to compute the electronic structure and elastic properties of novel cubic and tetragonal $BaFeO_3$.

† We have observed a significant agreement between the computational values of optimized lattice parameters, the theoretical and experimental results from other sources for cubic and tetragonal $BaFeO_3$.

† Computational values of bulk moduli computed with ELASTCON and EOS programs have shown a significant agreement for the tetragonal $BaTiO_3$, rutile TiO_2 , cubic and tetragonal $BaFeO_3$ crystal systems.

† We explored the novel coupling between the electronic charge, spin and lattice structure.

† A novel interaction is detected between the crystalline lattice structure and electronic spin.

6.2 Future directions

The tetragonal $BaTiO_3$ possesses a displacement-type ferroelectric behavior. The elastic properties of tetragonal $BaTiO_3$, a displacement-type ferroelectric, are not completely understood. A general lack of agreement between the computational and experimental values of elastic constants and bulk moduli is observed. A comprehensive future effort is needed to understand the influence of the complex physics, experimental conditions and computational parameters on this general disagreement.

The experimental and computational effort must be performed in an integrated manner through a collaborative effort to understand the challenge of disagreement between the former and the latter. The computational and experimental methods are fairly different but the former can always lead the latter as being more effective. For rutile TiO_2 , a significant agreement between the computational and experimental values of lattice parameters, elastic constants and bulk moduli is only an initial step in the right direction. The challenges of the pressure and temperature dependency of the crystalline structure and elastic properties need to be addressed.

Moreover, the merit of computational programs of ELASTCON and EOS has enhanced the authenticity of the computational values of rutile TiO_2 . However, these computations can be extended further to cover the electronic band gap and volume charge density to fully understand the physics of rutile TiO_2 .

A detailed set of computations must also be followed to understand the pressure and temperature dependence of the elastic properties in all simple and complex crystalline structures. This may help in contributing to an increased reliability of our computational results.

There is a lack of experimental values of the lattice parameters for the high pressure phases of $BaFeO_3$. The experimental research must be carried out to determine the cubic and tetragonal crystalline structure and elastic properties in a detailed manner.

We have started the pressure-induced phase transitions study of cubic and tetragonal phases. These computations of the pressure-induced phase transitions must also be continued to confirm the possibility of a phase transition from cubic to tetragonal $BaFeO_3$ phase.

The novelty associated with the physics of transition metal oxide and our *ab-initio* computational methods has equally contributed to an initial evidence of an interaction between the electronic charge, spin, orbitals and lattice structure. However, an independent experimental verification of our computational results may enhance the veracity of our research effort.

Experiments must be conducted on 3-*d* transition metal oxides to establish the reliability of our computational results. The experimental detection of the pressure-induced phases and their impact on spin transitions may provide a key to verify

the computational results and to crosscheck the authenticity of our results on 3-*d* transition metal oxide perovskites.

Appendix A

JOURNAL PUBLISHING

AGREEMENT Elsevier B.V.2

YOUR ARTICLE DETAILS

Article: First principles computation of second-order elastic constants and equations of state for tetragonal $BaTiO_3$

Corresponding author: Mr. Ghous Narejo

E-mail address: gbnarejo@mtu.edu

Journal: Chemical Physics Letters

Our reference CPLETT28276

PII: S0009-2614(10)00707-4

DOI: 10.1016/j.cplett.2010.05.043

YOUR STATUS

I am one author signing on behalf of all co-authors of the manuscript

I am not a US Government employee but some of my co-authors are

DATA PROTECTION

I do wish to receive news, promotions and special offers about products and services from Elsevier B.V. and its affiliated companies worldwide.

A.0.1 ASSIGNMENT OF PUBLISHING RIGHTS

I hereby assign to Elsevier B.V. the copyright in the manuscript identified above (government authors not electing to transfer agree to assign a non-exclusive licence) and any supple-

mental tables, illustrations or other information submitted therewith that are intended for publication as part of or as a supplement to the manuscript (the "Article") in all forms and media (whether now known or hereafter developed), throughout the world, in all languages, for the full term of copyright, effective when and if the article is accepted for publication. This transfer includes the right to provide the Article in electronic and online forms and systems. No revisions, additional terms or addenda to this Agreement can be accepted without our express written consent. Authors at institutions that place restrictions on copyright assignments, including those that do so due to policies about local institutional repositories, are encouraged to obtain a waiver from those institutions so that the author can accept our publishing agreement.

A.0.2 RETENTION OF RIGHTS FOR SCHOLARLY PURPOSES

I understand that I retain or am hereby granted (without the need to obtain further permission) rights to use certain versions of the Article for certain scholarly purposes, as described and defined below ("Retained Rights"), and that no rights in patents, trademarks or other intellectual property rights are transferred to the journal. The Retained Rights include the right to use the Pre-print or Accepted Author Manuscript for Personal Use, Internal Institutional Use and for Scholarly Posting; and the Published Journal Article for Personal Use and Internal Institutional Use.

AUTHOR REPRESENTATIONS / ETHICS AND DISCLOSURE Author representations The article I have submitted to the journal for review is original, has been written by the stated authors and has not been published elsewhere. The article is not currently being considered for publication by any other journal and will not be submitted for such review while under review by this journal. The article contains no libellous or other unlawful statements and does not contain any materials that violate any personal or proprietary rights of any other person or entity. I have obtained written permission from copyright owners for any excerpts from copyrighted works that are included and have credited the sources in my article. If the article was prepared jointly with other authors, I have informed the co-author(s) of the terms of this publishing agreement and that I am signing on their behalf as their agent, and I am authorized to do so. **FUNDING AGENCY REQUIREMENTS AND OTHER POLICIES** For more information about the definitions relating to this agreement click [here](#). I have read and agree to the terms of the Journal Publishing Agreement. . 17th May 2010 T-copyright-v15/2009 Copyright (c) 2010 Elsevier B.V. All rights reserved.